Distribution Agreement

In presenting this thesis or dissertation as a partial fulfillment of the requirements for an advanced degree from Emory University, I hereby grant to Emory University and its agents the non-exclusive license to archive, make accessible, and display my thesis or dissertation in whole or in part in all forms of media, now or hereafter known, including display on the world wide web. I understand that I may select some access restrictions as part of the online submission of this thesis or dissertation. I retain all ownership rights to the copyright of the thesis or dissertation. I also retain the right to use in future works (such as articles or books) all or part of this thesis or dissertation.

Signature:

Chao Chen Date

Dynamics Calculations of Several Atmospheric Reactions on Global Potential Energy Surfaces

By

Chao Chen
Doctor of Philosophy

Chemistry

Joel M. Bowman, Ph.D.
Advisor

Michael C. Heaven, Ph.D.
Committee Member

James T. Kindt, Ph.D.
Committee Member

Accepted:

Lisa A. Tedesco, Ph.D.
Dean of the James T. Laney School of Graduate Studies

Date

Dynamics Calculations of Several Atmospheric Reactions on Global Potential Energy Surfaces

By

Chao Chen
B.S., University of Science and Technology of China, 2004

Adivsor: Joel M. Bowman, Ph.D.

An Abstract of
A dissertation submitted to the Faculty of the
James T. Laney School of Graduate School of Emory University
in partial fulfillment of the requirements for the degree of
Doctor of Philosophy
in Chemistry
2010

Abstract

Dynamics Calculations of Several Atmospheric Reactions on Global Potential Energy Surfaces

By Chao Chen

The potential energy surface (PES) plays a crucial rule in the computational simulation of chemical reactions. Sometimes, owing to the complexity of systems, only stationary points (minima and transition states) are characterized to represent the PES to explore reactions using statistical tools. However, the comprehensive and detailed dynamic studies call for global, full dimensional PES with accuracy. Recent progress by Braams and Bomwan enable us to construct the global potential energy surface of polyatomic system up to 10 atoms. The PES is mainly weighted least-square fit with respect to tens of thousands of high level *ab initio* electronic calculation energies. A critical ingredient of the PES is that it is made explicitly invariant under all permutations of like nuclei, and this property is built into the polynomial basis used for the fitting. Therefore, PES construction will be made routinely and more effort could be made on system itself.

In atmospheric chemistry, there are lots of fundamental chemical reactions with very important implication of many crucial processes like catalytic cycles to produce ozone. Based on the constructed PES with key feature of invariance under all permutations of like nuclei, we can perform very detailed dynamics studies of many such fundamental reactions, like C+C_2H_2, OH+NO_2, HO_2+NO, and photodissociation of CH_2CHCH_2, CH_2CDCH_2, to explore microscopic mechanisms. With the good agreement between calculation results and experimental data, and more importantly, with detailed theoretical exploration to explain experimental mysterious results like in photodissociation of CH_2CHCH_2 case, the quasi-classical dynamics based on accurate high-level global PES are shown to be a powerful tool to investigate fundamental atmospheric chemical reactions.

Dynamics Calculations of Several Atmospheric Reactions on Global Potential Energy Surfaces

By

Chao Chen
B.S., University of Science and Technology of China, 2004

Adivsor: Joel M. Bowman, Ph.D.

A dissertation submitted to the Faculty of the
James T. Laney School of Graduate School of Emory University
in partial fulfillment of the requirements for the degree of
Doctor of Philosophy
in Chemistry
2010

Acknowledgements

First of all, I would like to give the most sincere thank to my advisor, Professor Joel M. Bowman, for his inspirational instructions and patient guidance during these six years. Without his effort and support, this dissertation would not have been possible.

Here I also thank Dr. Michael C. Heaven and Dr. James T. Kindt for serving as my committee members, giving very nice suggestions.

I also want to express my appreciation to Dr. Tianquan Lian, Dr. Keiji Morokuma, Dr. Michael C. Heaven, Dr. James T. Kindt and Dr. Joel M. Bowman for the wonderful chemistry courses.

I acknowledge the previous and current members of Dr. Bowmans group, especially Dr. Xinchuan Huang, Dr. Tiao Xie, Dr. Zhong Jin, Dr. Alex Kaledin, Dr. Xiubin Zhang, Dr. Zhen Xie, Dr. Benjamin C. Shepler, Dr. Yimin Wang, Dr. Gabor Czako, Dr. Amit Sharma and Dr. Bina Fu for their enduring friendship and valuable discussions.

I also acknowledge members of Emerson Center, especillay Fuchang Yin, Dr. Guishan Zheng, Dr. Zhi Wang and Dr. Djamaladdin (Jamal) G. Musaev for their help on my graduate studies

I am especially grateful to Ann Dasher for the graduate study advice, Susan Browne and Jianli Zhao for their coordination work.

Last but not least, I would like to thank my parents Genfa Chen and Suping Wang, my wife Jin Liu, for their unlimited love understanding and support all these years.

Contents

List of Tables

List of Figures

Dedicate to my parents, Genfa and Suping,
and my beloved wife, Jin

Chapter 1

Introduction

With the development of both theoretical and experimental techiniques, understanding the essential details of chemical change of various chemical reactions becomes a very important aspect in the field of chemistry. For theoretical study, the potential energy surface, the function describing the molecular interactions, is the key for the simulation. Accurate potential energy surface is the prerequisite for subsequent simulation setup. Without a correct PES, regardless of the accuracy of the model, the calculating results are certain to be questionable or incorrect. While employing an accuate PES, the simulation can provide some details or useful aspects of system, even through the model may have some limitations. Therefore, PES construction is the most significant part for each project. In most cases, quasiclassical trajectory simulation based on high quality abinitio potential energy surface is such a combination that can describe a lot of chemical reactions reasonably as shown in this thesis.

This thesis is organized as following: chapter 2 gives the overall description of potential energy surface construction, while each following chapter will describe specific PES construction in details. Chapter 2 will also cover the model, quasi-classical trajectory, covering initial and final conditions. Chapter 3 and 4 focus on $C+C_2H_2$

reaction, with chapter 4 describing coupling of two PESs for surface hopping. Chapter 5 and 7 mainly tell the effort to construct HOONO PES for simlulation on HO_2+NO and OH+NO_2 association reaction. Update on CH_3HCO PES for improvement in $CH_3 \cdots HCO$ area is given in Chapter 8. Finally, with the help of newly constructed allyl PES, chapter 9 shows how to explain the discrepancy of internal energy distribution in photodissociation of allyl radical.

Chapter 2

Classical Trajectory Simulation on Potential Energy Surface

2.1 Ab Initio Potential Energy Construction

A global potential energy surface(PES) can be defined as an analytical function of internal coordinates of a system that gives the potential energy as a function of geometry. The potential energy surface can be constructed based on the basis of electronic structure calculations, semiempirical adjustment to experimental data or the combination of both methods. Now more and more research focus on the PES based on the *ab initio calculations*. A essential criteria for an potential energy surface representation includes that the PES should accurately characterize the asymptotic reactant and product molecules, have the correct symmetry properties of the system, represent the true potential accurately in interaction regions, and smoothly connect the asymptotic and interaction regions. In my projects, the potential energy surfaces are constructed based on the electornic structture calculations.

2.1.1 Potential Energy Function Representation

In order to describe the PES function, we take HOONO as the example. For the five-nucleus system HOONO, taking into account translational and rotational invariance, at least 9 (3N-6) coordinates are required to specify the conguration for evaluating the potential. However, we represent the PES as a function of all 10 internuclear distances, as this facilitates a representation that is invariant with respect to permutations of like nuclei. Note that for systems of more than four atoms the set of all internuclear distances forms a redundant set of coordinates, but this does not pose any problems because molecular dynamics and other calculations are done in Cartesian coordinates. One needs to convert from Cartesians to internuclear distances, which is well defined. We can define a conceptually straightforward function to be used as PES function and the tting function would be given by

$$V(x_1, x_2, \cdots, x_d) = \sum_{i_1 \cdots i_d} C_{i_1 \cdots i_d} S(x_1^{i_1} x_2^{i_2} \cdots x_d^{i_d}) \tag{2.1}$$

where d=N(N-1)/2 (in HOONO d=10), x_i are the internuclear distances or, more generally, functions of the internuclear distances. The symbol S indicates a symmetrization operator so that the symmetrized monomial $S(x_1^{i_1} x_2^{i_2} \cdots x_d^{i_d})$ is invariant with respect to interchange of any two identical nuclei. The summation over exponents $i_1 \cdots i_d$ is constrained by some maximum degree bound on $i_1 + i_2 + \cdots + i_d$. Moreover, for each symmetrized monomial only one representative tuple of indices must occur in the summation.

A critical ingredient of our work is that the PES is made explicitly invariant under all permutations of like nuclei, and this property is built into the polynomial basis used for the fitting. The problem of specifying a basis of the space of polynomials invariant under some permutation symmetry belongs to computational invariant the-

ory [1], and specically the theory of invariants of finite groups. From computational invariant theory the algebra of invariant polynomials is generated by a small number of primary invariants and a larger number of secondary invariants. The primary and secondary invariant polynomials together thus form a system of generators, also called an integrity basis for the space of invariant polynomials. A Magma computation gives very quickly, by way of the Hilbert Series, the dimension of the relevant space of invariant polynomials at each degree.

In reality, Suppose i and j will generally be used as nuclear indices, Let r(i) be the position of the ith nucleus and let $r_{i,j}$=‖ r(i)-r(j)‖ be the distance between nuclei i and j. The independent variables of the PES fit are the 10 internuclear distances $r_{i,j}$ (i ≠ j and that $r_{i,j}$ and $r_{j,i}$ denote the same variable). The basis functions used in the fit are functions of auxiliary variables y_{ij} given by , $y_{ij} = exp(-r_{ij}/\lambda)$. The range parameter, λ, is fixed at the value 2.0 bohr. The Morse variables tend to a constant in the limit $r_{ij} \to \infty$ and so can describe reactive potential energy surfaces. Finally we define our PES function as

$$V(\mathbf{y}) = \sum_{\alpha} h_{\alpha}(p_1(\mathbf{y}) \cdots p_d(\mathbf{y}))q_{\alpha}(\mathbf{y}) \tag{2.2}$$

where we denote the set of variables y_{ij} as a vector y, of dimension d, which in the present case equals 10. p_k denotes the k-th primary invariant polynomial and q_{α} denotes the the α-th secondary invariant polynomial. These are both homogeneous polynomials in the variables y_{ij} and also each is invariant under the molecular permutation symmetry group. There are d primary invariant polynomials and here h_{α} is a polynomial of them. In the implementation the total degree of the polynomial V(y) is bounded by some value, D. Thus, the weighted degree of the polynomial h_{α} is bounded by D-deg(q_{α}),where the weighted degree of a monomial term $p_1^{m_1} \cdots p_d^{m_d}$ in h_{α} is $m_1 deg(p_1) + \cdots + m_d deg(p_d)$.

In the present HOONO case, the symmetry group is S3 and it acts on the 10 variables y_{ij}. S3 is reducible since the permutation acts separately on the spaces of O-O distances (3 variables), O-H distances (3 variables), O-N distances (3 variables) and the H-N distance (1 variable). Each of these three 3-dimensional subrepresentations of S3 is itself reducible as the sum of a 1-dimensional and a 2-dimensional representation. This leads to a system of 10 primary invariants, of which 3 are functions of the transformed O-O distances, likewise 3 for the O-H and 3 for the O-N subsystems, and one invariant function of the transformed H-N distance. For the 3-dimensional subspaces the associated three primary invariant polynomials are of degrees 1, 2, and 3. The exact form of the polynomials is not unique; the simplest choice for purpose of exposition is elementary symmetric monomials in the transformed internuclear distances. For the purpose of illustration and to simplify the notation let y1, y2 and y3 denote the 3 transformed variables for any of these three subspaces. In term of these variables the primary invariants are $y_1^k + y_2^k + y_3^k$; k=1,2,3. For the 1-dimensional subspace the associated primary invariant is just the transformed H-N distance itself.

The simplest secondary invariant is the constant function 1 (polynomial of degree 0); beyond that there turn out to be 3 secondary invariants of degree 2, 7 of degree 3, 6 of degree 4, 6 of degree 5, 10 of degree 6, and 3 of degree 7. Unlike the primary invariants, the secondary invariants cannot each be confined to an irreducible component of the representation; in general they mix several irreducible components. For the present small molecular group they could be determined by hand, but for our general work on invariant expansions for molecular symmetry groups we rely on the procedures in the representation theory chapter of the Magma computer algebra system.

Assuming that the basis is available and that there are m basis functions and n congurations in the database (with m$\leq$ n) then the polynomial coefcients are deter-

mined by a weighted least-squares system of dimension n×m. The solution of the system involves an efficient factorization of the associated matrix, for which we use the routine DSYEV from LAPACK. The computational cost scales as m^2n. If the kth entry in the database has ab initio energy f(k) then the corresponding entry in the least-squares system is given weight $\delta/(\delta + f(k) - f_{min})$,where f_{min} denotes the global minimum potential energy over all entries in the database and where the parameter δ was set to 0.1 hartree.

2.2 Classical Trajectory Method

Classical trajecotry method is employed in our group to explore dynamics of some atmospheric reactions. Hamilton's classical equations of motion are integrated to simulate motions of indiviual atoms.

$$\begin{aligned} \frac{\partial H}{\partial q_i} &= \frac{-dp_i}{dt} \\ \frac{\partial H}{\partial p_i} &= \frac{dq_i}{dt} \end{aligned} \tag{2.3}$$

where q, p are coordinates and conjugate momenta of atoms, respectively. H is the system's Hamiltonian, expressed as

$$H = T(p, q) + V(q) \tag{2.4}$$

where T is the kinetic energy and V is the potential energy.

The next section we will focus on how to choose the initial condition for the classical trajecotory, sampling the appropriate distribution to select initial values of coordinates p and conjugate momenta q, so that results from an ensemble of trajecotries can be used to predict dynamics of reactions. Section 2.5 will describe how

to calculate properties of prodcuts based on coordinates p and conjugate momenta q at the termination of classical trjactories.

2.3 Initial Conditions

2.3.1 Microcanonical normal mode sampling

Microcanonical normal mode sampling [2] is employed for each fragment or moluecule. Initailly given the starting geometry, we can perform normal mode analysis by diagonalizing the mass-weighted Cartesian force constant matrix. The corresponding harmonic frequency is $\omega_{\mathbf{i}}$, and the normal mode eigenvector is $\mathbf{L}$. Suppose there are n normal modes in the molecule. then the harmonic zero-point energy is

$$E = \sum_{i=1}^{n} E_i = \sum_{i=1}^{n} \frac{1}{2}\omega_i \tag{2.5}$$

While the Hamiltonian for this system of n normal mode can aslo be expressed as

$$H(\mathbf{P}, \mathbf{Q}) = E = \sum_{i=1}^{n} E_i = \sum_{i=1}^{n} \frac{P_i^2 + \omega_i^2 Q_i^2}{2} \tag{2.6}$$

Random values for P_i and Q_i are chosen by giving a random phase by

$$\begin{aligned} Q_i &= [(2E_i)^{1/2}/\omega_i] cos(2\pi R_i) \\ P_i &= -(2E_i)^{1/2} sin(2\pi R_i) \end{aligned} \tag{2.7}$$

where R_i is a random number.

Then **Q** and **P** are used to transfrom back to Cartesian coordinate **q** and momenta **p** using normal mode eigenvector **L**

$$\begin{aligned} \mathbf{q} &= \mathbf{q}_0 + \mathbf{M}^{-1/2}\mathbf{L}\mathbf{Q} \\ \mathbf{p} &= \mathbf{M}^{1/2}\mathbf{L}\mathbf{P} \end{aligned} \tag{2.8}$$

where $\mathbf{q_0}$ the equlibrium (starting) geometry in Cartesian coordinates and **M** is a diagonal mass matrix.

2.3.2 Angular Momentum Setup

Next we treat angular momentum part. The angular momentum **J** can be calulated using either of the forms

$$\begin{aligned} \mathbf{J} &= \sum_{i=1}^{n} \mathbf{r}_i \times \mathbf{m}_i \dot{\mathbf{r}}_i \\ \mathbf{J} &= \mathbf{I}\omega \end{aligned} \tag{2.9}$$

We construct the moment of inertia matrix **I** via

$$\begin{aligned} I_{xx} = \sum_{i=1}^{n}(y_i^2 + z_i^2), I_{yy} = \sum_{i=1}^{n}(z_i^2 + x_i^2), I_{zz} = \sum_{i=1}^{n}(x_i^2 + y_i^2) \\ I_{xy} = I_{yx} = -\sum_{i=1}^{n} x_i y_i, I_{xz} = I_{zx} = -\sum_{i=1}^{n} x_i z_i, I_{yz} = I_{zy} = -\sum_{i=1}^{n} y_i z_i \end{aligned} \tag{2.10}$$

The moment of inertia matrix **I** is diagonalized, and the molecule is transformed into the principle frame. In principle frame, the second form for calculating angular

momentum in equation 2.9 can simply be reduced to

$$\begin{aligned} J_x &= I_{xx}\omega_x \\ J_y &= I_{yy}\omega_y \\ J_z &= I_{zz}\omega_z \end{aligned} \tag{2.11}$$

With **J** calculated using the first one in equation 2.9 and digonalized **I**, the angular velocities ω_0 can be obtained as

$$\begin{aligned} \omega_x &= J_x/I_{xx} \\ \omega_y &= J_y/I_{yy} \\ \omega_z &= J_z/I_{zz} \end{aligned} \tag{2.12}$$

velocities can be adjusted by removing angular parts of the velocities.

$$\mathbf{v} = \mathbf{v}_0 - \omega_0 \times \mathbf{r} \tag{2.13}$$

Once rotation quantum number J_{rot}'s components are obtained, adding rotational energy can be done by

$$\mathbf{v} = \mathbf{v} + \omega \times \mathbf{r} \tag{2.14}$$

2.3.3 Rotational Sampling for symmetric top polyatomic reactant

Suppose it it oblate, and the rotational quantum number is J and K, the components of the angular momentum can be found from

$$\begin{aligned} j &= \sqrt{(J(J+1)\hbar} \\ j_z &= K\hbar \\ j_x &= (j^2 - j_z^2)^{1/2} sin 2\pi R \\ j_y &= (j^2 - j_z^2)^{1/2} cos 2\pi R \end{aligned} \tag{2.15}$$

where R is a random number.

When calculating the thermally averaged cross-section $\sigma(\nu, T)$, it is sufficiently accurate to sample j and j_z from their classical Boltzmann distribution

$$\begin{aligned} P(j_z) &= exp(-j_z^2/2I_z kT) \qquad 0 \leq j_z \leq \infty \\ P(j) &= jexp(-j^2/2I_x kT) \qquad j_z \leq j \leq \infty \end{aligned} \tag{2.16}$$

The Von Neumann rejection method is used to sample j_z from $P(j_z)$, while j is sampled by the cumulative distribution function formula

$$j = [j_z^2 - 2I_x kT ln(1-R)]^{1/2} \tag{2.17}$$

the component of j_x, j_y are found from equation 2.15. Once J components are obtained, adding rotational energy can be done by equation 2.14.

For NO_2, I rewrite the code similar to code in VENUS and implement it to my md code, do 100000 times initial rotational sampling, calculate the J_x (NO_2 is prolate)

and J values each time to get corresponding distributions, compared with analytical forms

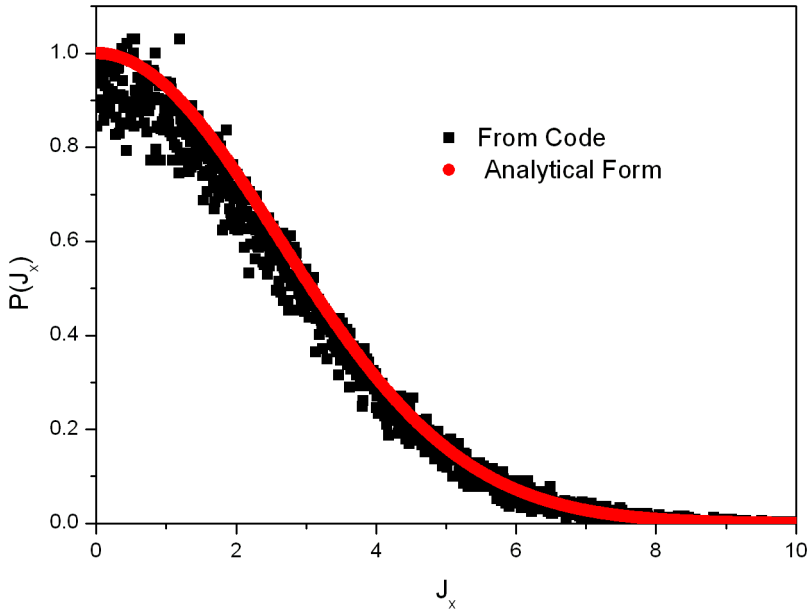

2.3.4 Relative Position and Energy in Bimolecular Reaction

After sampling the vibrational and rotational energy for both reactants, denoted as A and B, the relative position and energy will be setup to simulate the bimolecular collision. First each reactant is randomly rotated through Euler's angles to present a random orientation

$$\begin{aligned} \mathbf{q} &= \mathbf{R}(\theta, \phi, \chi)\mathbf{q}^0 \\ \dot{\mathbf{q}} &= \mathbf{R}(\theta, \phi, \chi)\dot{\mathbf{q}}^0 \end{aligned} \tag{2.18}$$

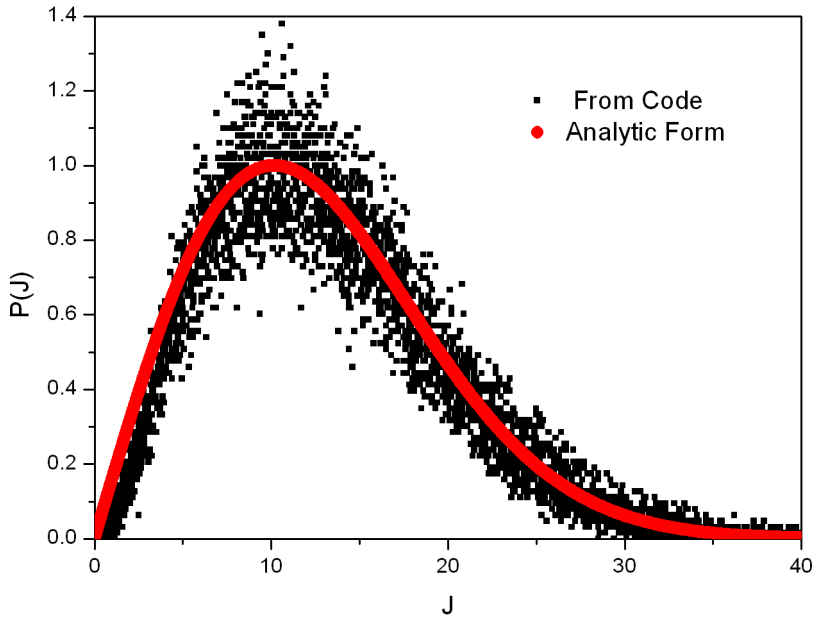

where $\mathbf{R}(\theta, \phi, \chi)$ is the Euler rotation matrix. The angles θ, ϕ, χ are obtained by

$$cos\theta = 2R_1 - 1 \quad \phi = 2\pi R_2 \quad \chi = 2\pi R_3 \tag{2.19}$$

Here we need to generate R_1, R_2, R_3 , three different random numbers. Suppose we define b is the impact parameter, and s is the initial distance between center of mass A and that of B. After random orientation for both A and B discussed above, reactant A is set at the origin, and reactant B is moved to the point

$$x = 0 \quad y = b \quad z = (s^2 - b^2)^{1/2} \tag{2.20}$$

Relative energy will be added to the current system so that reactant A and B can collide with each other. Momentum and energy conservation are applied to the

relative energy E_{rel}

$$m_A v_A = m_B v_B$$
$$\frac{1}{2} m_A v_A^2 + \frac{1}{2} m_B v_B^2 = E_{rel} \tag{2.21}$$

the center of mass velocities v_A ,v_B for reactant A, B, respectively, can be added by

$$v_A = m_A \sqrt{2\mu E_{rel}} \quad v_B = m_B \sqrt{2\mu E_{rel}} \tag{2.22}$$

where μ is the reduced mass between A and B.

2.4 Cross-Section and Rate Constant Calculation

Trajecotry calculation results can be used to calculate cross-section and rate constant for each product channel. Indepenedent of the reaction specification, the classical mechanical expression for the reaction cross-section is

$$\sigma_r = \int_0^{b_{max}} P_r(b) 2\pi b db \tag{2.23}$$

where b is the impact parameter, b_{max} is the largest impact parameter leading to reaction, and $P_r(b)$ is the probability of reaction.

The average reaction probability $< P_r(b) >$ can be evaluated from

$$\begin{aligned} < P_r(b) > &= \int_0^{b_{max}} P_r(b) 2\pi b db / \int_0^{b_{max}} 2\pi b db \\ &= \int_0^{b_{max}} P_r(b) 2\pi b db / \pi b_{max}^2 \end{aligned} \tag{2.24}$$

Combining previous two equations we can get another expression for cross-section as

$$\sigma =< P_r(b) > \pi b_{max}^2 \tag{2.25}$$

with impact parameter randomly generated between 0 and b_{max} using the equation

$$b = (R_i)^{1/2} b_{max} \tag{2.26}$$

where R_i is the random number between 0 and 1

The average reaction probability is

$$< P_r(b) >= N_r/N \tag{2.27}$$

where N is the total number of trajectories and N_r the number which are reactive

Thus the reaction cross-section

$$\sigma_r = \frac{N_r}{N} \pi b_{max}^2 \tag{2.28}$$

Batches of trajectories are set up at different collision energies to get collision energy dependence of the cross-section based on method above to sample impact parameter b. Multiple cross-section $\sigma_r(v_{rel} : T)$ by v_{rel} gives the rate constant for a fixed relative velocity of v_{rel} as

$$k(v_{rel}; T) = v_{rel} \sigma_r(v_{rel} : T) \tag{2.29}$$

Integrating the rate constant in equation above over Boltzmann relaive velocity distribution $P(v_{rel} : T)$ for the temperature T presents the thermal bimolecular rate

constant:

$$k(T) = \int_0^\infty v_{rel}\sigma_r(v_{rel} : T)P(v_{rel} : T)dv_{rel} \tag{2.30}$$

2.5 Final Conditions

Once the trajectories finish or terminate, forming products, the final Cartesian coordinates and conjugate momenta are commonly used to calculate properties of products. Suppose the chemical reaction is

$$A + B \rightarrow C + D \tag{2.31}$$

2.5.1 Relative Velocity and Translation Energy

The difference between velocities of center of mass of C and D is product relative velocity $\dot{\mathbf{R}}$. In terms of product C, the center of mass position and velocity are obtained by

$$\begin{aligned} X_C &= (\sum_{i=1}^{n_C} m_i x_i)/M_D \quad Y_C = (\sum_{i=1}^{n_C} m_i y_i)/M_D \quad Z_C = (\sum_{i=1}^{n_C} m_i z_i)/M_D \\ \dot{X}_C &= (\sum_{i=1}^{n_C} m_i \dot{x}_i)/M_D \quad \dot{Y}_C = (\sum_{i=1}^{n_C} m_i \dot{y}_i)/M_D \quad \dot{Z}_C = (\sum_{i=1}^{n_C} m_i \dot{z}_i)/M_D \end{aligned} \tag{2.32}$$

Where upper case X,Y,Z are used to identify center-of-mass positions and velocities of the products. M_C is the mass of C. Note the sum is over n_C number of atoms in C. So the separation between the center-of-mas of C and D:

$$\begin{aligned} \mathbf{R} &= (X_D - X_C)\hat{\mathbf{i}} + (Y_D - Y_C)\hat{\mathbf{j}} + (Z_D - Z_C)\hat{\mathbf{k}} \\ &= R_x\hat{\mathbf{i}} + R_y\hat{\mathbf{j}} + R_z\hat{\mathbf{k}} \end{aligned} \tag{2.33}$$

and the product relavite velocity is

$$\dot{\mathbf{R}} = \dot{R}_x\hat{\mathbf{i}} + \dot{R}_y\hat{\mathbf{j}} + \dot{R}_z\hat{\mathbf{k}} \tag{2.34}$$

The product relative translational energy is

$$E_{rel} = \frac{\mu_{CD}\dot{\mathbf{R}}\cdot\dot{\mathbf{R}}}{2} \tag{2.35}$$

where μ_{CD} is the reduced mass between C and D.

2.5.2 Velocity Scattering Angle

The velocity scattering angle θ is the angle between the relative velocity vector for the reactant $\dot{\mathbf{R}}_\mathbf{0}$ and the prodcut's relative velocity vector $\dot{\mathbf{R}}$ given in equation 2.34 :

$$\theta = cos^{-1}(\frac{\dot{\mathbf{R}}\cdot\dot{\mathbf{R}}_\mathbf{0}}{\dot{R}\dot{R}_0}) \tag{2.36}$$

2.5.3 Internal Energy

Since center-of-mass positions and velocities are already available in equation 2.32, the coordinates and velocities of the atoms in C in the center-of-mass frame can be calculated as

$$\begin{aligned} x_i' &= x_i - X_C \\ \dot{x}_i' &= \dot{x}_i - \dot{X}_C \end{aligned} \tag{2.37}$$

So the kinetic energy of C, T_C, is

$$T_C = \sum_{i=1}^{n_C} \frac{m_i(\dot{x}_i'^2 + \dot{y}_i'^2 + \dot{z}_i'^2)}{2} \tag{2.38}$$

and the interal energy of C is

$$E_C = T_C + V_C \tag{2.39}$$

where the potential energy V_C is the energy difference bewteen energy of current configuration and energy of equilibrium geometry.

2.5.4 Rotational Energy and Vibrational Energy

The product C can be transformed into principle axis frame mainly using procedure from section 2.3.2. With the digonalized $\mathbf{I}$, the angular velocities ω_0 from equation 2.12, we can determined the rotational energy as

$$E_{rot} = \frac{1}{2}(I_x\omega_x^2 + I_y\omega_y^2 + I_z\omega_z^2) \tag{2.40}$$

Internal Energy consists of rotational energy and vibrational energy. Since internal energy and rotational energy is available, vibrational energy can be easily determined.

Chapter 3

Dynamics Calculations of C + C_2H_2 Reaction

3.1 Introduction

The reaction of ground state carbon C(^{3}P) with acetylene, $C_2H_2(^1\Sigma_g^+)$, has attracted theoretical and experimental attention in recent years due to its importance in interstellar chemistry [6], [7], combustion processes [8] and hydrocarbon syntheses [9], [10], The main products of the reaction are *linear(l)*-C_3H, *cyclic(c)*-C_3H and C_3. The ratio of *c*-C_3H/*l*-C_3H has been measured and apparently varies in different interstellar clouds [10]- [12].

The rate constant for the reaction was measured by Husain and co-workers [9], [13], at room temperature and by Sims and co-workers [14], [15] at temperatures down to 15K. These experiments measured the disappearance of reactants and so cannot distinguish isomers, *l*-C_3H and *c*-C_3H. Crossed Molecular Beam (CMB) experiments [12], [16]- [19] have also been reported on reactions of C(^{3}P) + C_2H_2 and C(^{1}D)

+ C_2H_2 and hydrogen isotopic variants. Kaiser *et al.* [12], [16], [17] have performed an extensive series of CMB experiments on the reaction at collision energies between 8.8 and 45.0 kJ mol^{-1}. Although mass spectrometric detection cannot distinguish *l*-C_3H and *c*-C_3H, these authors tried to explain the possibility of the existence of two isomers based on changes in the angular scattering with collision energy. They inferred that both isomers were formed under the conditions of their experiments. Casavecchia and co-workers and Costes and co-workers [18], [19] have reported differential and integral cross-sections for the $C(^3P)$ + C_2H_2 and $C(^1D)$ + C_2H_2 reactions. These groups have also detected the C_3 + H_2 product and invoked a spin-orbit coupling between the singlet and triplet surfaces to account for the appearance of this product, which was not reported by Kaiser and co-workers.

Calculations of the $C(^3P)$ + C_2H_2 reaction at various levels of *ab initio* and Density Functional Theory have been performed by several groups [20]- [25]. Energetics, structures and vibrational frequencies for the reactant, products and several stationary points in the reaction have been reported. Most of the calculations agree that *c*-C_3H isomer is more stable than *l*-C_3H isomer, but the energy difference between two isomers is only 4-8 kJ mol^{-1} according to high level MRCI calculations [21]. However, the (harmonic) zero-point energy of *c*-C_3H isomer is 3 to 6 kJmol-1 higher than*l*-C_3H depending on the level of calculations, and so at low reaction energy the zero-point energy effect on the dynamics can be very significant. The energy difference between these two isomers is still not accurately (i.e., to within less than a few kJ mol^{-1}) known.

Variational RRKM theory with an *ab initio* (CASSCF) calculation of relevant stationary points and reaction paths was used to obtain the thermal rate constant at 300 K; however, the branching to the *l*-C_3H and *c*-C_3H products was not calculated [22]. Dynamics calculations of the triplet reaction have been done in reduced dimension-

ality. Buonomo and Clary [24] reported a quantum wavepacket calculation for the C(^{3}P) + C_2H_2 reaction in two degrees of freedom, the distance between C(^{3}P) and the center of mass of C_2H_2 , and the angle between the C-C_2H_2 displacement and the C_2H_2 bond axis. They constructed a two-dimensional potential energy surface based on *ab initio* energies [CCSD(T)/cc-pVDZ] with the other seven degrees of freedom being optimized. Reaction cross-sections were calculated at collision energies from 5 to 70 kJ mol^{-1} and they concluded that l-C_3H isomer is highly favored but the fraction of c-C_3H increases with increasing collision energy. Subsequently, Takayanagi reported three [25] and two-degree-of-freedom [26] quantum calculations of the reaction cross-section using a potential energy surface based on B3LYP/6-31G(d,p) density functional calculations, very similar to ones used by us. The three-degree-of freedom total reactive cross-section is larger than the one reported by Buonomo and Clary in two-degree-of-freedom [24] calculations. The more recent two-degree-of-freedom calculations of Takayanagi [26] find that c-C_3H was highly favored over l-C_3H, in sharp disagreement with results of Buonomo and Clary, which find the opposite. Also, while Buonomo and Clary report a cross-section for l-C_3H that varies from roughly 35 to 12 $\dot{A}^2$ in the range of collision energies 5 to 40 kJ mol^{-1}, Takayanagi reports a cross-section for l-C_3H that is roughly 0.01 $\dot{A}^2$ and the one for c-C_3H that is below 2 $\dot{A}^2$ in this energy range.

Given these very different conclusions about the dominant product of this reaction from reduced dimensionality calculations and some unresolved issues raised by molecular beam experiments we were motivated to study this reaction in full dimensionality using new potential energy surfaces (PESs) for both triplet and singlet systems and quasiclassical trajectory calculations using them .

3.2 Tirplet and Singlet C_3H_2 Potential Energy Surface

The construction of PESs for the C(^{3}P) + C_2H_2 reaction and for a limited portion for singlet reaction (described below) mainly used procedures described in section 2.1. The PESs are based on a many-body expansion using basis functions of all internuclear distances that are invariant under permutations of like nuclei. The coefficients in this representation are obtained by weighted least-squares fitting to the results of tens of thousands of electronic structure calculations, done at the DFT B3LYP/6-311g(d,p) level of theory. This level of theory and basis set was employed by other groups and shown to produce quite realistic energies in comparison to more accurate methods for both the triplet and singlet potentials [23], [25].

Energies for the triplet were obtained by a combination of direct dynamics calculations done with a variety of initial conditions and total energies. These data were supplemented by calculations done at stationary pointes and intrinsic reaction coordinates connecting them. Preliminary fits were done using these data and subsequent dynamics calculations were done on these fits, which typically revealed regions where additional data was needed. The end result of this iteration between electronic structure calculations and function fitting is a database of 86,551 configurations for triplet surface which covers the entire region reactants C(^{3}P) + C_2H_2 to products and the complex regions. The root mean square fitting error is 3.6 kJ/mol for the entire data set which included energies as high as 26 355 kJ/mol relative to the global minimum.

Our interest in the singlet PES is not focused on the C(^{1}D) + C_2H_2 reaction, which is energetically closed at the energies of interest. We are interested in the possible role the singlet PES plays via interaction with the triplet PES to form the products. This possible role has been pointed out previously [18], [19], [21], [23] since it is known that *l*-C_3H, *c*-C_3H products also correlate with the singlet PES. In addition the singlet products C_3 + H_2 correlate with this PES. In order to investigate this we generated

a singlet PES but limited to the complex region and the products l-C_3H, c-C_3H and C_3 + H_2 using a combination of direct-dynamics and stationary point data and the iterative procedure described briefly for the triplet PES. Roughly 100 000 energies were used in the final fit, which had an RMS fitting error of 3.5 kJ/mol for the entire data set.

All DFT stationary points were located on the PESs and in Figure 3.1 and 3.2 we show comparisons between the DFT and PES energies at these as well as structures for the triplet and singlet cases, respectively. As seen the PES, energies are generally in very good agreement with the DFT ones, i.e., within a few kJ mol^{-1}. For the reactant, the difference is only 0.6 kJ mol-1. Product states in exothermic channels, of especially the c-C_3H +H, l-C_3H +H, channels are fit essentially exactly on the triplet PES and less accurately on the singlet one.

Comparisons of harmonic normal-mode frequencies at these stationary points and also for C_2H_2 and products are given in Tables 3.1 and 3.2 for the triplet and singlet reactions, respectively. As seen the frequencies are also generally in very good agreement with the ones for reactant, products and stationary points. Exceptions are for some very low frequencies which signify a "flat" region of the potential along the corresponding normal mode.

3.3 Dynamics Caculation Results

Quasiclassical trajectory calculations (QCT) for the triplet reaction were performed for five initial collision energies in the range 5 to 40 kJ mol^{-1} on the triplet PES. These energies correspond to experimental ones in the CMB experiments. Limited QCT calculations were also done for the singlet reaction leading to l-C_3H, c-C_3H and

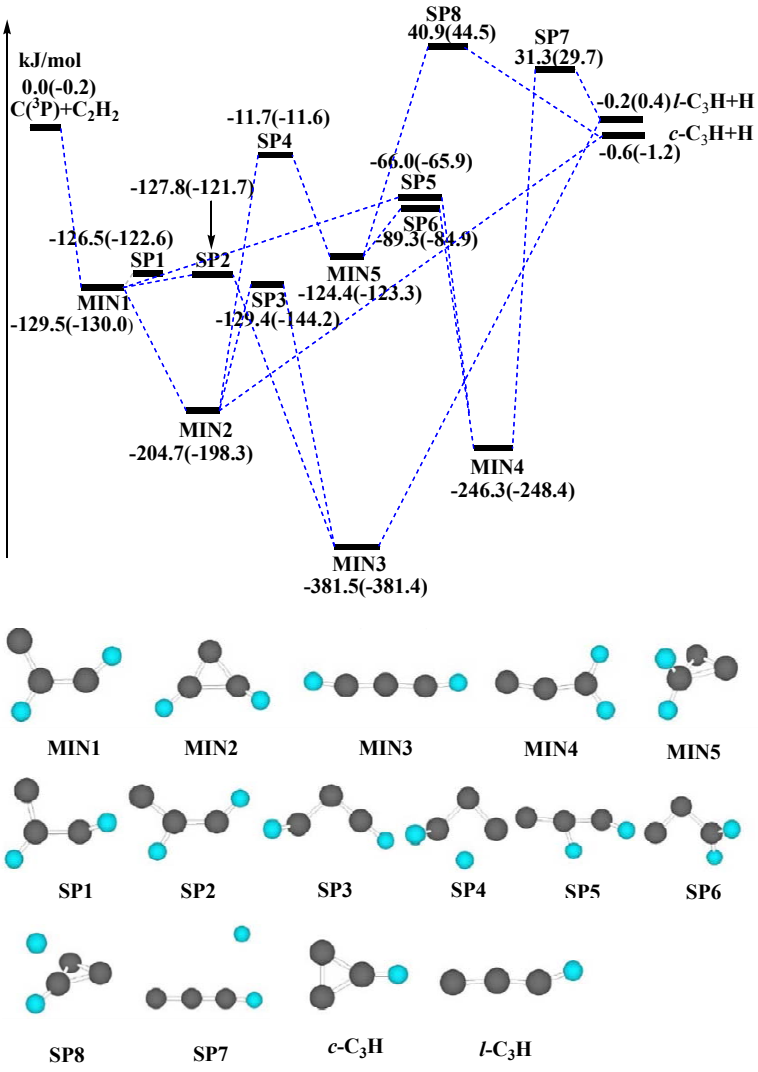

Figure 3.1 Schematic energy diagram for the reaction of $C(^3P) + C_2H_2$. The energies indicated in the upper panel are from the DFT calculations and those in parentheses are from the PES fit. The corresponding molecular structures are indicated in the lower panel.

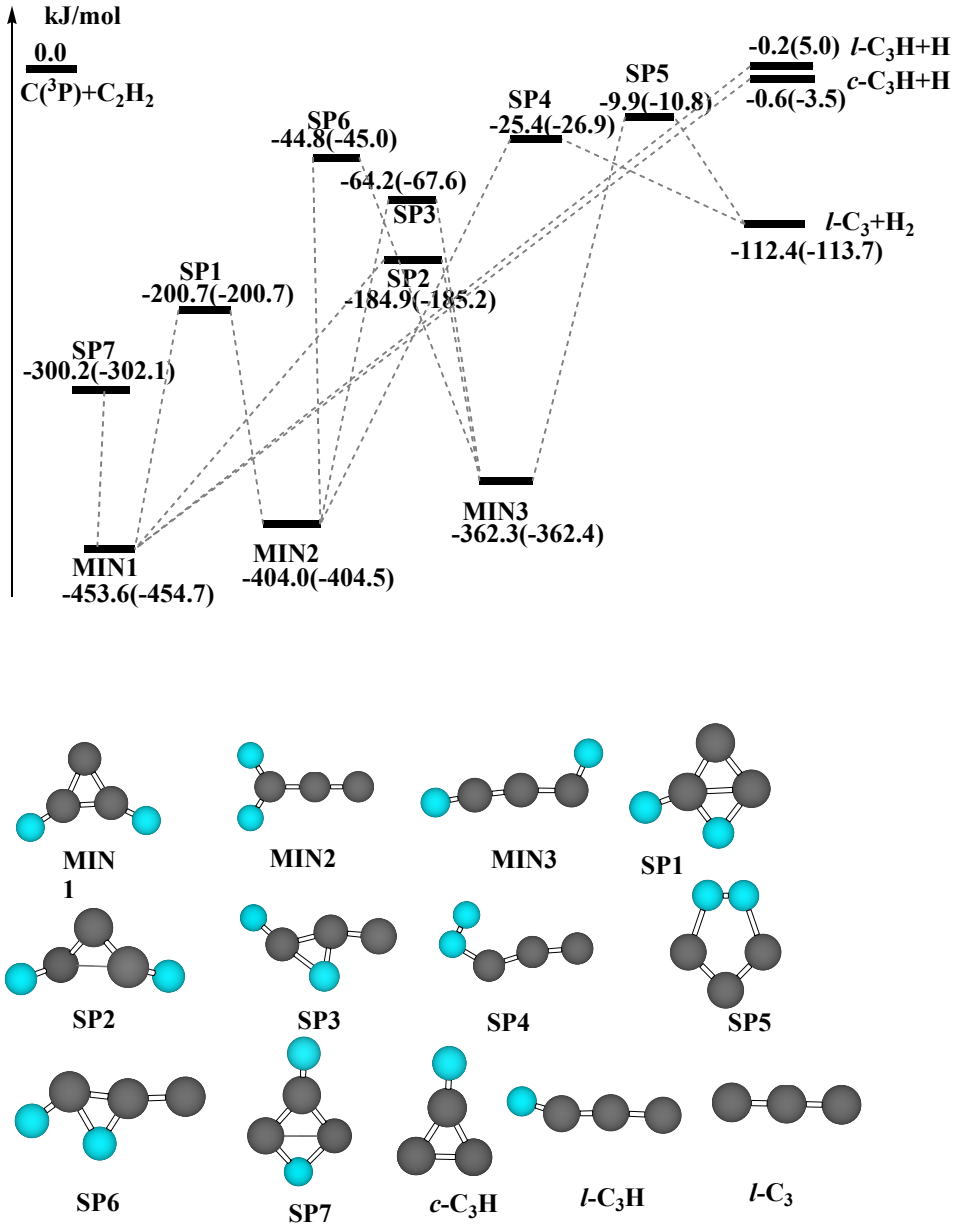

Figure 3.2 Schematic energy diagram for the reaction of $C(^1D) + C_2H_2$. The energies indicated in the upper panel are from the DFT calculations and those in parentheses are from the PES fit. The corresponding molecular structures are indicated in the lower panel. The zero of energy is the $C(^3P) + C_2H_2$ asymptote.

Table 3.1 Harmonic frequencies (cm^{-1}) of reactant, products and stationary points for triplet C_3H_2. The first column and second column are DFT and the PES, respectively.

C_2H_2	C_2H_2	*c*-C_3	*c*-C_3	*c*-C_3H	*c*-C_3H	*l*-C_3H	*l*-C_3H	INT1	INT1
DFT	PES	DFT	PES	DFT	PES	DFT	PES	DFT	PES
642	639	1155	1173	540	737	242	111	236	286
642	639	1156	1173	872	905	300	243	361	353
773	745	1618	1630	916	908	374	244	692	755
773	745			1223	1099	1190	1146	748	792
2070	2146			1615	1607	1888	1897	1051	1029
3421	3400			3221	3232	3393	3480	1219	1161
3523	3470							1318	1294
								3070	3062
								3262	3280
INT2	INT2	INT3	INT3	INT4	INT4	INT5	INT5	SP12	SP12
DFT	PES	DFT	PES	DFT	PES	DFT	PES	DFT	PES
566	340	44	145	365	144	604	515	216i	307i
639	547	106	176	445	394	650	568	380	422
851	736	226	196	648	578	913	849	675	761
898	851	422	389	940	867	978	897	733	814
922	928	423	389	974	1034	1029	906	1035	1009
1083	975	1286	1266	1348	1406	1500	1396	1108	1074
1668	1585	1716	1706	1439	1523	1745	1623	1404	1388
3086	3189	3442	3464	3128	3134	3061	2917	3087	3101
3321	3429	3452	3470	3217	3214	3140	3076	3255	3260
SP13	SP13	SP23	SP23	SP25	SP25	SP34	SP34	SP45	SP45
DFT	PES	DFT	PES	DFT	PES	DFT	PES	DFT	PES
170i	251i	921i	661i	1293i	1208i	1160i	1137i	454i	507i
492	288	284	302	504	470	337	350	581	372
623	472	404	445	819	719	372	366	644	667
785	719	809	456	831	873	562	583	811	824
965	910	870	637	998	1036	658	649	1001	928
1163	1111	1164	1229	1248	1166	1109	1119	1363	1349
1458	1520	1588	1466	1490	1504	1607	1593	1446	1470
2866	2808	3182	3257	2002	2221	2551	2444	3093	3064
3249	3336	3395	3265	3104	2888	3271	3218	3224	3199
SP5cpr	SPSP5cpr	SP4lpr	SP4lpr						
DFT	PES	DFT	PES						
756i	912i	125i	189i						
273	346	125	233						
453	575	259	254						
502	804	312	275						
903	889	373	356						
930	982	501	474						
1200	1044	1191	1155						
1577	1633	1883	1855						
3212	3352	3390	3385						

C_3 products, by starting them at the each of the three minima on the singlet PES with the restriction of zero total angular momentum.

Now we present results of QCT calculations of the C(^{3}P) + C_2H_2 reactions with C_2H_2 the ground rotational state and with zero-point energy. As expected the calculations find that the reaction proceeds via long-lived collisions complexes. However, as shown in Figure 3.3 the time evolution of the reaction products is not the same. As seen, *c*-C_3H is formed in a relatively short time (and with small probability), whereas

Table 3.2 Harmonic vibrational frequencies (cm^{-1}) of reactant, products and stationary points for the singlet C_3H_2. The first column and second column are DFT and the PES, respectively.

c-C_3H_2	*c*-C_3H_2	H_2CCC	H_2CCC	HCCCH	HCCCH	SP1	SP1	SP2	SP2
DFT	PES	DFT	PES	DFT	PES	DFT	PES	DFT	PES
798	846	233	232	301	302	929i	923i	977i	856i
891	852	293	291	302	407	715	678	419	324
894	877	1042	1044	425	448	909	951	828	403
1003	1075	1052	1048	835	726	1009	1035	884	661
1070	1098	1147	1175	974	756	1101	1178	962	1013
1312	1326	1485	1488	1088	1133	1227	1203	1447	1344
1646	1702	2043	2039	1937	1918	1490	1593	1569	1532
3221	3170	3091	3058	3022	3110	2232	2266	3148	3103
3256	3187	3168	3161	3438	3487	3182	3157	3150	3115
SP3	SP3	SP4	SP4	SP5	SP5	SP6	SP6	SP7	SP7
DFT	PES	DFT	PES	DFT	PES	DFT	PES	DFT	PES
1708i	1585i	1125i	1093i	1289i	1283i	1064i	1057i	529i	598i
226	310	222	285	606	533	259	435i	747	766
377	333	288	399	642	741	427	406	789	842
418	420	582	561	773	847	520	466	1040	1078
897	958	830	918	1043	1120	903	829	1132	1216
1139	1177	1179	1191	1167	1162	1124	1142	1339	1414
1763	1631	1718	1908	1477	1486	1747	1600	1556	1638
2366	2300	2045	2004	1497	1525	2388	2190	2397	2377
3070	3039	2560	2702	2315	2629	3133	3138	3292	3333
c-C_3H	*c*-C_3H	*l*-C_3H	*l*-C_3H	*l*-C_3+H_2	*l*-C_3+H_2				
DFT	PES	DFT	PES	DFT	PES				
542	849	218i	345	108	71				
875	901	242	345	108	71				
918	964	377	528	1237	1287				
1223	1205	830	528	2148	2114				
1615	1611	1171	1177	4419	4396				
3215	3312	1902	1967						
		3446	3526						

the time evolution for the major *l*-C_3H product follows the longer decay dynamics of the collision complex. The time-dependence of *l*-C_3H formation and decay of the collision complex were fit using a simple first-order kinetics model and has allowed us to extrapolate the dynamics to infinite time. In this way we have obtained the reaction probability to obtain *l*-C_3H at each impact parameter. The resulting cross-sections for this product and *c*-C_3H are shown in Figure 3.4 as a function of the collision energy. As seen, the cross-section for the *l*-C_3H product is much larger than for the *c*-C_3H one. Both cross-sections decrease with increasing collision energy; however, the one *l*-C_3H more than for *c*-C_3H. These results for the cross-sections disagree with the reduced dimensionality calculations of Takayanagi which were reviewed above. Also it is clear that for the energies considered here the QCT calculations find that *l*-C_3H is the major product, in agreement with the two-degree-of-freedom quantum

calculations of Buonomo and Clary; there is also agreement on the magnitude of the cross-section for the l-C_3H product.

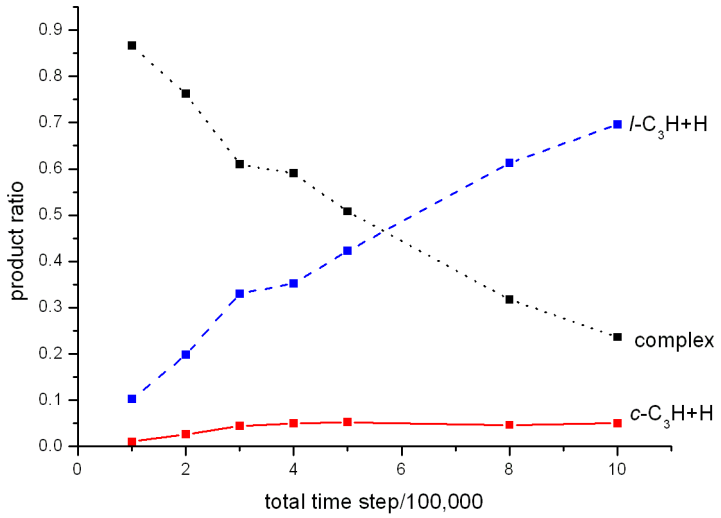

Figure 3.3 Time dependence of trajectories for triplet reaction at an impact parameter of 2.0 Bohr and initial relative collision energy of 40 kJ mol^{-1}.

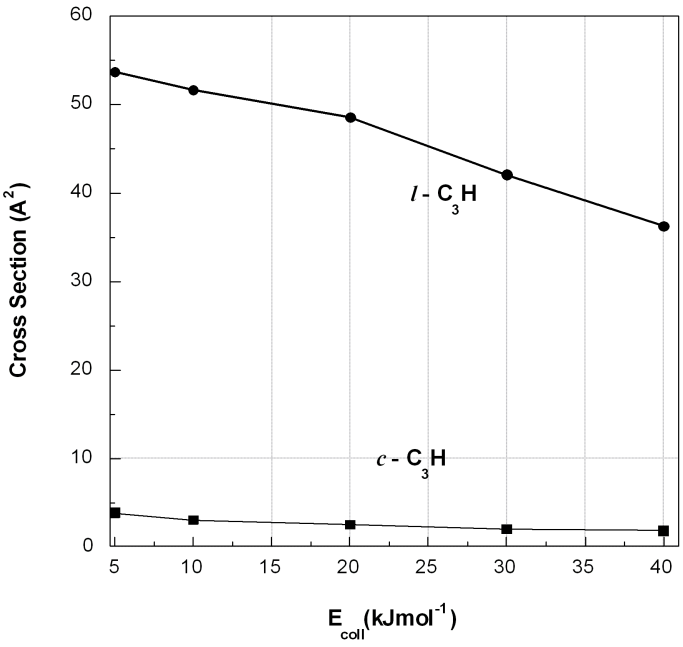

Figure 3.4 Reaction cross-sections for the products l-C_3H and c-C_3H as a function of initial relative kinetic energy.

Now consider results of limited QCT calculations for zero total angular momentum, starting at several minima of the singlet PES and with sufficient energy to form the C_3(singlet) and *l*-C_3H and *c*-C_3H products. The time evolution of the branching ratio of products is shown in Figure 3.5 for sets of 500 trajectories initiated at the two minima indicated. As seen all products, *l*-C_3H, *c*-C_3H and C_3 are formed in about equal amounts and with roughly the same time dependence. Also note that the energy of these trajectories is much higher than energies considered for the triplet reaction. The reason is that the minima on the singlet PES are considerably "deeper" than those on the triplet PES and thus the lifetime of the collision complex is very long. Indeed even at the high energy of these trajectories only roughly 20% of the complex has decomposed to products.

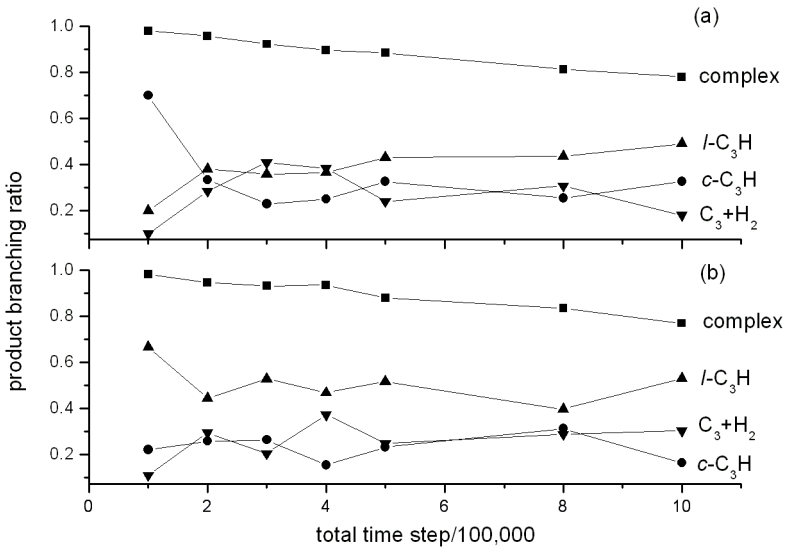

Figure 3.5 Time dependence of the product branching ratios averaged over 500 trajectories on the singlet PES started at different minima (a) H_2CCC, (b) HCCCH, with zero total angular momentum at a total energy of 84 kJ mol^{-1} relative to C(^{3}P) + C_2H_2. The curve labeled complex refers to the ratio of number of trajectories in complex region to the number of total trajectories.

Clearly, the present results indicate that the branching ratio for the *l*-C_3H, *c*-C_3H products contrasts markedly on the singlet and triplet surfaces and that the C_3

product is formed with significant probability on the singlet surface. For the singlet dynamics to have significance for the C(^{3}P) + C_2H_2 reaction there would need to be significant singlet-triplet interaction. Given the long collision lifetimes of the triplet and singlet systems, and the known fact that the two surfaces do have minimum seams of crossing that are accessible in the complex region [23], this seems highly probable. Future studies coupling these surfaces would certainly be needed to quantify this expectation.

3.4 Summay and Conclusion

We presented results of quasiclassical trajectory calculations of the C(^{3}P) + C_2H_2 → l-C_3H, c-C_3H + H reaction and also limited calculations of the unimolecular decay of C_3H_2(singlet) using new full-dimensional potential energy surfaces. These were obtained by fitting ca 10^5 electronic energies obtained with Density Functional Theory using a fitting basis that is invariant with respect to any permutation of H atoms and C atoms. Calculations on the triplet PES calculations found l-C_3H to be the dominant product over the collision energy range 5 to 40 kJ/mol. By contrast calculations on the singlet PES found l-C_3H, c-C_3H and C_3 products to be formed in roughly equal amounts. Dynamics on both surfaces found that the reactions proceed via long-lived complexes, which likely lead to significant triplet/singlet interactions. The implications for experiments on C(^{3}P) + C_2H_2 are that analysis of such experiments may be complicated by the significant singlet/triplet interactions and the quite different product branching for the two potentials.

Chapter 4

Surface-Hopping Trajectory Calculations of the $C(^3P)+C_2H_2$

4.1 Surface-Hopping Dynamics Approach

4.1.1 Minima on the seam of crossing

In the previous chapter, we described the nice quality of singlet and triplet PES with comparison with corresponding high level ab initio calculations in terms of stationary point configuration, potential energy, harmonic frequency and dissociation behavior. However, no comparison is made in the seam of crossing region, where singlet and triplet surfaces should be evaluated simultaneously. Mebel *et al.* [23] has successfully locate two minima (MSX) on the singlet-triplet seaming of crossing at the level of B3LYP/6-311G(d,p), and later these authors [27] found the third one significantly lower in energy at the level of CASSCF(14,11)/6-311G**. We also successfully locate those three stationary points on the seam of the triplet and singlet PES via the constrained optimization method using energy gradients [28]. Figure 4.1 shows the

geometrical parameter comparisons between PES optimized configurations and the *ab initio* ones, which confirms that the two PESs have good description in the vicinity of seam of crossing area.

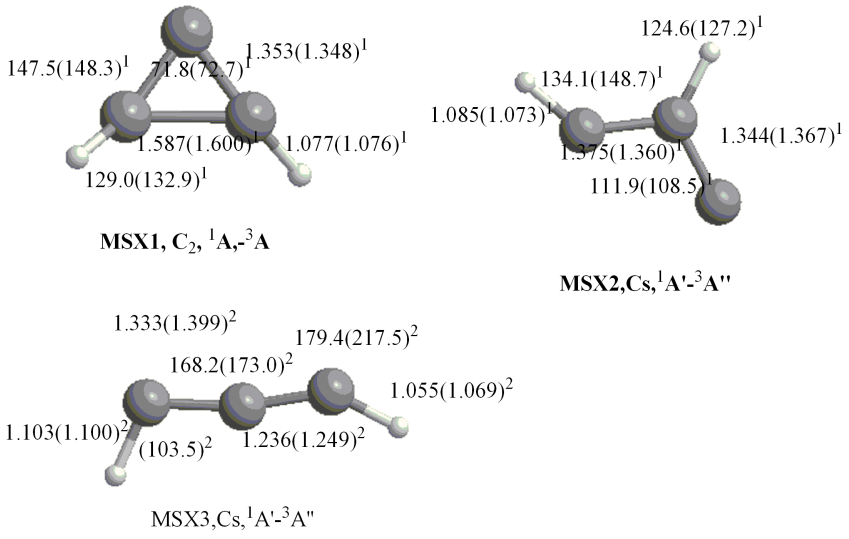

[1]A. M. Mebel, W. M. Jackson, A. H. H. Chang, and S. H. Lin, J. Am. Chem. Soc. 120, 5751(1998)
[2]A. M. Bebel, V. V. Kislov, M. Hayashi. J Chem. Phys. 126, 204310(2007)

Figure 4.1 Structures of indicated three minima on the singlet-triplet seam of crossing(MSX). The values outside squares are from the PES, and the values in squares are from various high-level ab initio calculations. Units are Angstroms and degrees

4.1.2 Transition probability

Simulation of the $C(^3P)+C_2H_2$ reaction in full dimensionality has been carried out using the quasiclassical variant of surface hopping approach [3] with two (singlet and triplet) basis functions. The first assumption taken here for non-adiabatic transition is that the probability of switching from one surface to the other one is calculated in a pseudo-one-dimensional way using Laudau-Zener theory [3]- [5]. The Laudau-Zener approximation gives the probability of not changing surface at a given crossing

encounter point q at time t as

$$p = exp[-\frac{\frac{2\pi}{\hbar}V_{st}^2(q(t))}{\frac{d}{dt}\Delta V(q(t))}]$$
$$\Delta V(q) = V_t(q) - V_s(q) \tag{4.1}$$

and evaluated at t=t_0, time at the surface intersection , being the root of the equation

$$\Delta V(q(t)) = 0 \tag{4.2}$$

$V_{st}(q)$ is the spin-orbital coupling term, which couples the singlet and the triplet PES. V_s(q), V_t(q) are the potential energy at configuration q in singlet and triplet state, respectively. (1-p) is the probability of hopping on the first passage, and p(1-p) is the probability for not hopping on first crossing the seam then hopping upon crossing it again in the reverse direction. Finally the net hopping probability is given by

$$P_{sh}^{Landau-Zener} = (1+p)(1-p) \tag{4.3}$$

Normally, spin-orbital coupling term depends on the configuration on the PES. Mebel *et al.* [27] obtained spin-orbital coupling term for various stationary points on the singlet and triplet surfaces at the level of CASSCF(14,11)/6-311+G(3df,2p) level. The values are relatively small in the range of 5.5 and 15.0 cm^{-1}, averaged as 8.22 cm^{-1}. Here we take another assumption that the spin-orbital coupling term is independent of the geometry and taken as a constant value of 8.22 cm^{-1} for Laudau-Zener transition probability calculation in Equation 4.1.

4.1.3 Dynamics setup and Transition scheme

The calculation started from triplet surface of C(^{3}P)+C_2H_2, with initial condition prepared as the standard QCT calculation. In brief, a normal mode analysis was done for the C_2H_2 reactant, and it was given harmonic zero-point energy. Then random sampling was done from each normal mode in the usual fashion. Adjustments were then made to the momenta to ensure total angular momentum equal to zero. The trajectories were propagated with the Verlet methods, initially in triplet state with a small time-step of 3 atomic units (roughly 0.07 fs) into triplet C_3H_2 complex region.

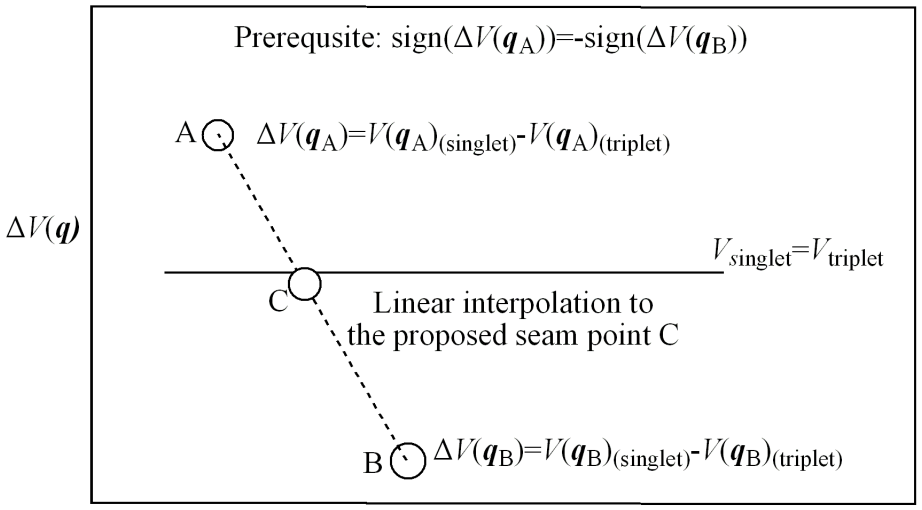

$$q_C = \frac{|\Delta V(q_B)|}{|\Delta V(q_A)|+|\Delta V(q_B)|} q_A + \frac{|\Delta V(q_A)|}{|\Delta V(q_A)|+|\Delta V(q_B)|} q_B$$

Figure 4.2 Proposed crossing point C location scheme. Point A and B represent the consecutive molecular dynamics propagation point with propagation time as stepsize 3 in atomic units. $\Delta V(q_A)$ stands for singlet and triplet energy difference for configuration q at point A. Linear interpolation between A and B to generate proposed crossing point C in terms of geometry and velocity. Equation below formulates the geometry interpolation.

Here we propose our scheme for potential crossing location and treatment shown in Figure 4.2. For each point or configuration q during propagation, potential energy difference between singlet and triplet PES, denoted as $\Delta V(q)$, is monitored. Provided

that previous study showed that the Intersystem crossing (ISC) is facile in this system [29], here comes the third assumption about the location of crossing point on the seam. If the energy difference $\Delta V(q)$ changes sign between consecutive propagation step A and B, it is likely that during this process, the molecule reaches the seam at a certain time, with the corresponding configuration of the same energy in singlet and triplet state, and that is the potential switching point on the seam of crossing, denoted as $\widehat{C}$. If transition is identified to be successful after switching probability evaluation, it will occur at point $\widehat{C}$ and the molecular dynamics propagation will resume from here in the new electronic state surface. Since propagation time between A and B is so small, 3 atomic units (roughly 0.07 fs), the calculated seam point, denoted as C, can be obtained by linear interpolation based on A and B in terms of $|\Delta V(q)|$. The configuration, velocity vectors at this seam point C are calculated based on point A and B linearly, shown in Equation 4.4. If the approximation is good enough, the interpolated point C should be very close to the actual point on the seam $\widehat{C}$, and the time at point C should be close to t_0, the solution of Equation 4.2. Therefore, the time derivative of the energy difference $|d\Delta V(q)/dt|$ at actual seam point $\widehat{C}$, used in Equation 4.1 can be calculated at point C based on point A and B linearly, shown in Equation 4.4

$$\begin{aligned} q_C &= \frac{|\Delta V(q_B)|}{\Delta V(q_B)+\Delta V(q_A)} q_A + \frac{|\Delta V(q_A)|}{\Delta V(q_B)+\Delta V(q_A)} q_B \\ |\frac{d}{dt}\Delta(q_C)| &= |\frac{d}{dt}(V_s(q_C)-V_t(q_C))| \\ \simeq \frac{|[V_s(q_B)-V_t(q_B)]-[V_s(q_A)-V_t(q_A)]|}{\Delta t} &= \frac{|\Delta V(q_B)-\Delta V_(q_A)|}{\Delta t} \end{aligned} \tag{4.4}$$

Where Δt is the propagation time stepsize, taken as 3 atomic units (roughly 0.07fs). $P_{sh}^{Landau-Zener}$ is calculated on the linearly interpolated crossing point C, and compared with a random number to decide validity of transition. If the transition is valid, the molecule switches to the new electronic state at crossing point C and stays

in the new state looking for possible configuration to flip back to the old surface until it dissociates. If C is very close to $\widehat{C}$, no velocity correction needed for conserving energy and angular momentum [3], [5]. The code is implemented to monitor $\Delta V(q)$ at point C. If C is away from $\widehat{C}$ and transition is accomplished, velocity correction will be triggered to conservation, even though the transition can be very rare because of extremely low transition probability in location away from seam shown later. Note here the gradient and energy in C and the gradient in B will be recalculated based on the new PES to allow for velocity verlet propagation. Finally, the algorithm chart for this setup is shown in Figure 4.3.

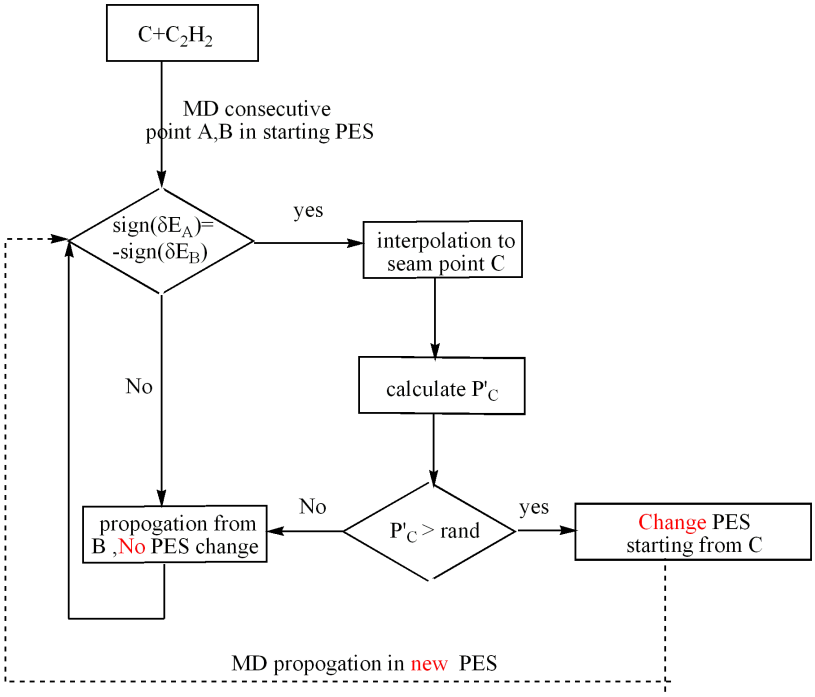

Figure 4.3 Algorithm chart for the surface-hopping dynamics.

4.1.4 Estimate of Transition Probability

Provide information above we can get an estimate of equation 4.3 as

$$P_{sh}^{Landau-Zener} = 1 - exp(-\frac{0.01934}{|\Delta V(q_B) - \Delta V(q_A)|}) \tag{4.5}$$

where the energy difference between $\Delta V(q_A)$ and $\Delta V(q_B)$ is expressed in cm^{-1}. Figure 4.4(b) shows the transition probability curve. Recall that $\Delta V(q_A)$ and $\Delta V(q_B)$ have different sign. You can see that if point B and A are away from crossing point, the proposed transition probability decrease extremely quickly to zero, (eg. $\Delta V(q_A)$ - $\Delta V(q_B)$= 5 cm^{-1}, $P_{sh}^{Landau-Zener}$=0.0039), while B and A are in the close vicinity of cross point , the transition probability is a little bit higher, but still low(eg. $\Delta V(q_A)$ - $\Delta V(q_B)$= 0.1 cm^{-1}, $P_{sh}^{Landau-Zener}$=0.17). Low transition probability can be offset by high frequency to reach seam region. To check how often the molecule enters the intersystem crossing region, one typical molecular dynamics trajectory propagated only on the triplet PES is shown in Figure 4.4(a), with $\Delta V(q)$ as the variable. The plot confirms that the singlet and triplet surface get entangled together in C_3H_2 complex region where the consecutive configurations A and B frequently have $\Delta V(q_A)$ and $\Delta V(q_B)$ sign changed, consistent with the ISC facility statement [29]. In the subsequent surface hopping calculation, the ratio of number of actual transition made to those of potential transition location is shown in Figure 4.4(c) to be around $2*10^{-4}$, relative small transition probability. The net outcome is that if triplet C_3H_2 finally switches to the singlet state, it rarely transits back to the triplet state, and there are still considerable trajectories in the singlet state before dissociation.

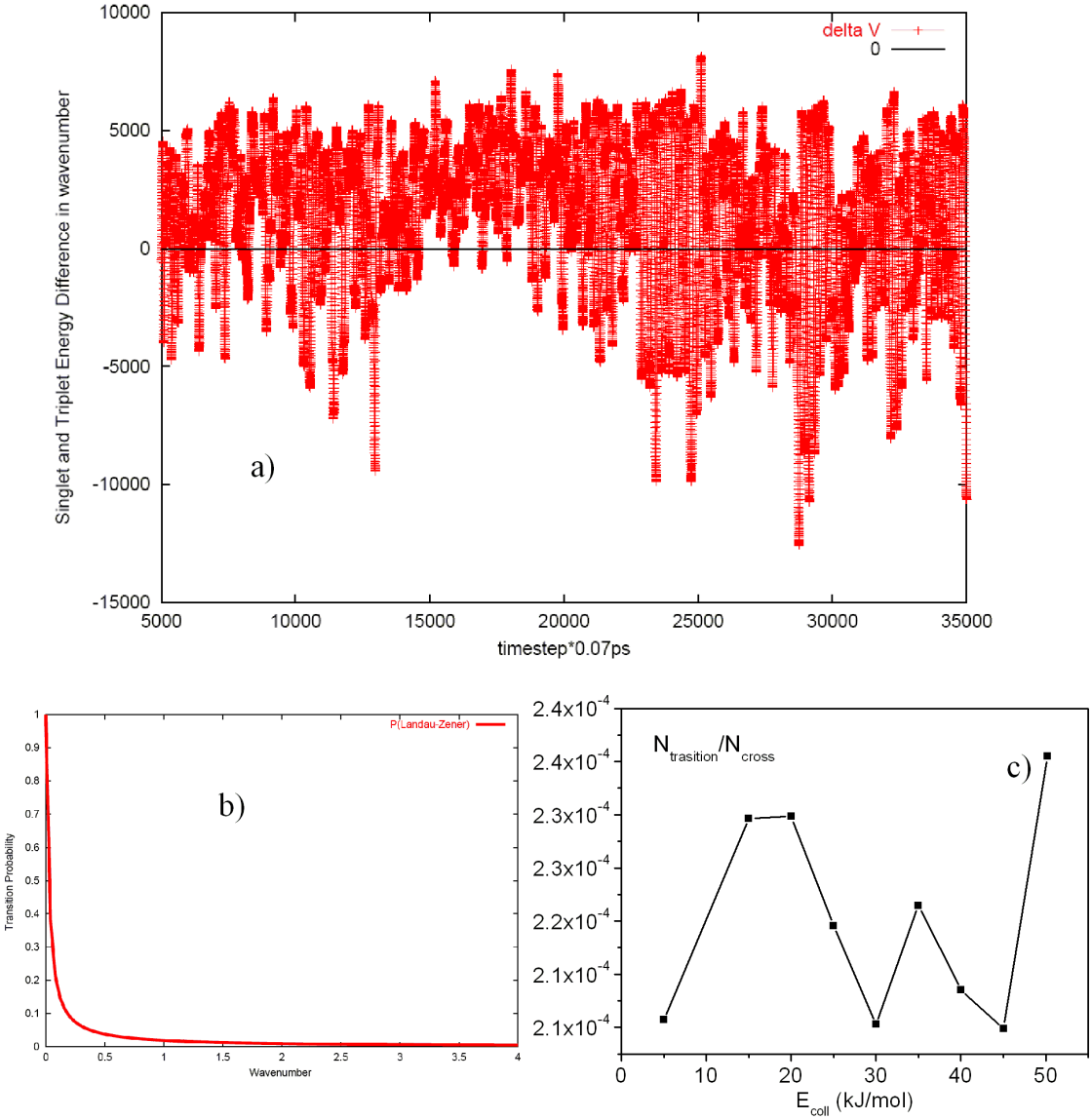

Figure 4.4 a) Time evolution of the energy difference between the singlet state and the triplet state for a trajectory run in the triplet state that illustrates high frequency of configuration crossing seam. b) Plot of equation 4.5 for the estimate Laudau-Zener transition probability as the function of $\Delta V(q_A)$ -$\Delta V(q_B)$. c) Collision energy dependence of ratio of number of actual transition to that of possible transition or crossing location.

4.2 Surface-hopping Dynamics Results and Discussion

500 trajectories were done at each relative collision energy from 5 to 50 kJ/mol at low impact parameter b= 2 Bohr, propagating with a small time-step of 3 atomic units (roughly 0.07 fs) up to 145 ps (2,000,000 time steps). The state of each configuration is monitored along propagation to keep track of actual transition location and final dissociation channel state. The final product can be l-C_3H or c-C_3H either from singlet or triplet C_3H_2 state, or C_3+H_2 exclusively from singlet C_3H_2 state.

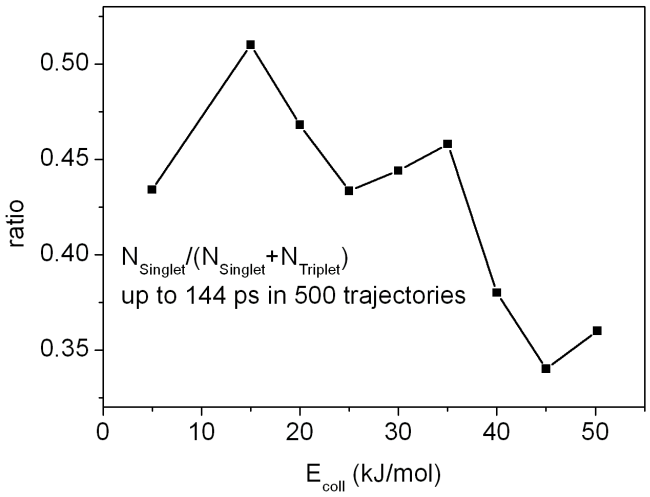

Figure 4.5 Collision energy dependence of ratio of fragment product dissociated from singlet PES to that from triplet PES that illustrates the net ratio of finished trajectories changing from original triplet state to singlet state.

Obviously, the entire product forming trajectories can be from either triplet C_3H_2 complex or switched singlet complex. Therefore, all the trajectories can be grouped into two categories, triplet state forming products and singlet state forming products. First, each trajectory is labeled as from triplet or singlet state, and the grouped trajectories are analyzed to identify the property of singlet and triplet PES separately. Figure 4.5 shows the C_3H_2 complex state of reactive trajectories, or the ratio of singlet state forming products. You can see that approximately 45% trajectories starting

from triplet state finally stay in the singlet state until dissociation. The lower the collision energy, the high ratio of the singlet state products. The singlet PES plays as a comparable role as triplet PES in this reaction.

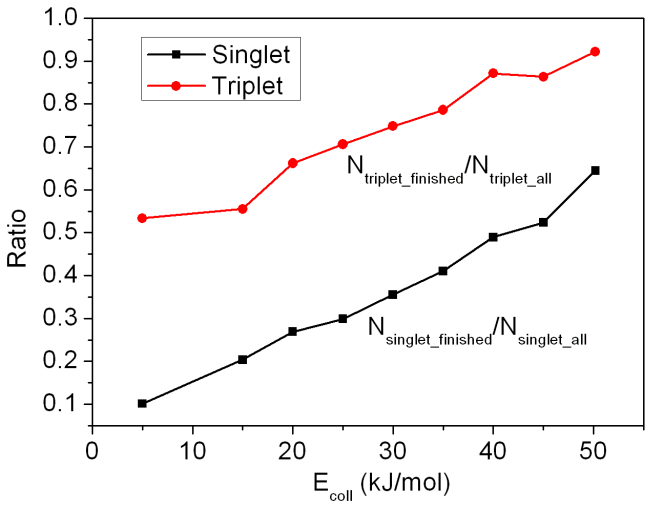

Figure 4.6 Collision energy dependence of fraction of singlet or triplet complex undergoing dissociation.

Dissociation behavior from different PES may be different in terms of stability, product preference. Figure 4.6 shows the tendency of C_3H_2 complex to dissociate from singlet and triplet state, respectively. Molecule getting trapped in the triplet PES is relatively easier to dissociate rather than that in the singlet PES, which is reasonable since the singlet PES well is about 100 kJ/mol deeper than triplet one [27]. Both dissociation ratio increases as the collision energy increased, and in triplet case at 50 kJ/mol, nearly 90% of the complexes become fragment products.

In terms of the product preference, the fraction of dissociated trajectories from singlet and triplet state C_3H_2 complex are shown in Figure 4.7(a), (b), respectively. In case of triplet state forming complex, l-C_3H appears to be the absolutely dominant product independent of collision energy, with the l-C_3H/c-C_3H ratio close to 10; while in singlet state complex dissociation case, l-C_3H and c-C_3H yields in comparable amount

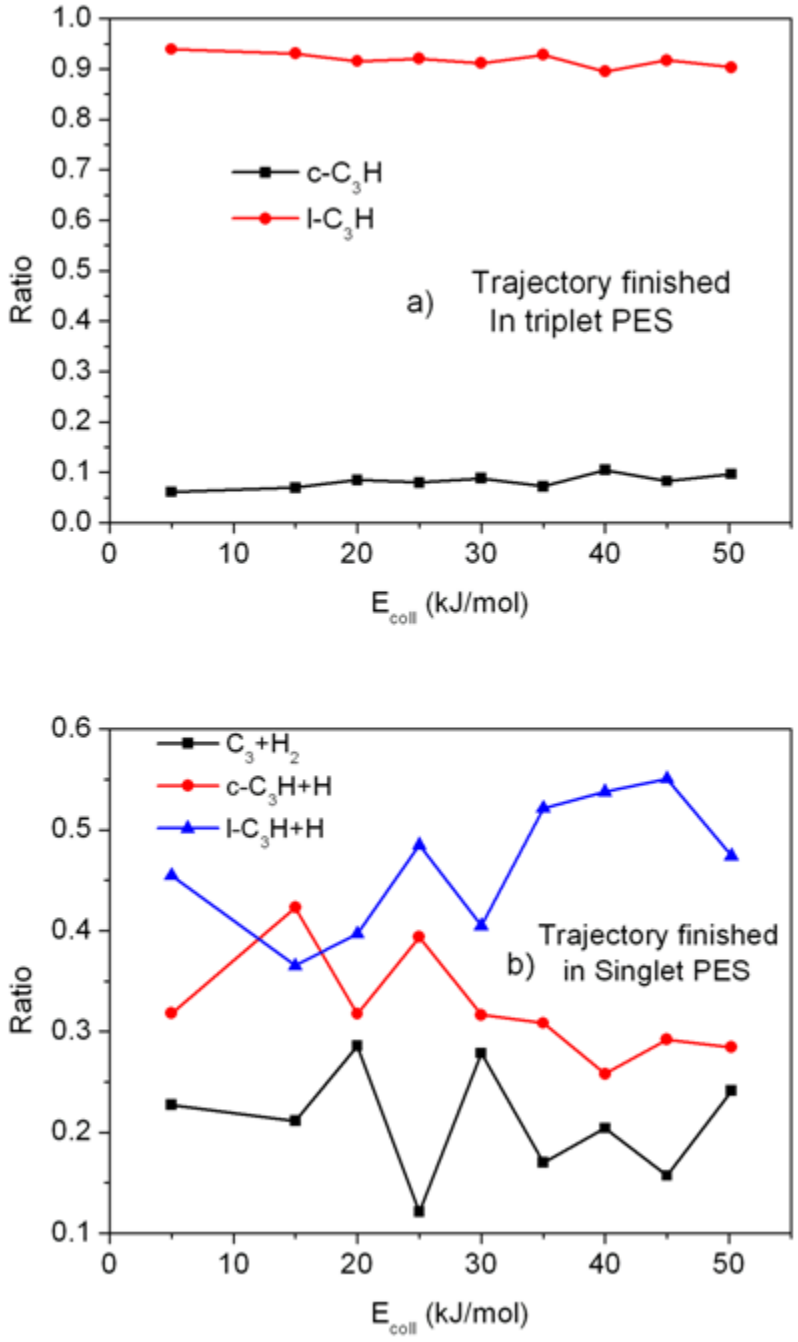

Figure 4.7 a) Energy dependence of the fraction of l-C3H and c-C3H from dissociated trajectories in triplet state. b) Energy dependence of the fraction of *l*-C_3H, *c*-C_3H, and C_3+H_2 from dissociated trajectories in singlet state.

with l-C_3H a little bit more favorable at high collision energy, which means that at least a considerable amount of products of l-C_3H and c-C_3H can be formed from the singlet PES. Note that about 20% singlet state trajectories lead to C_3+H_2 . Those are the trajectories to form spin-forbidden C_3+H_2 from triplet state via ISC. All those results are consistent with our conclusion in previous chapter.

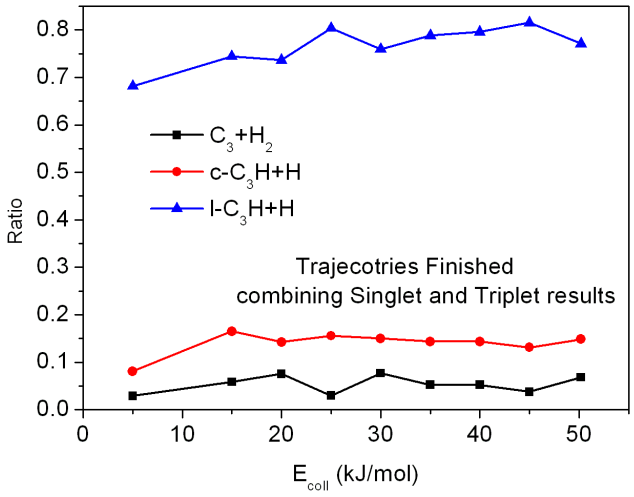

Figure 4.8 Energy dependence of the fraction of l-C_3H, c-C_3H and C_3+H_2 trajectories regardless of the originating state.

Now we ignore the origin of those products, all product forming trajectories are treated equally without distinction. The final product ratio is shown in Figure 4.8. Here we can see that l-C_3H, c-C_3H and C_3+H_2 are all produced in this C(^{3}P)+C_2H_2 reaction. Approximately about 80% are l-C_3H, 15% are c-C_3H, and 5% are C_3+H_2, where the ratio is independent of collision energy. The l-C_3H still dominates with a ratio of 6 to c-C_3H, in disagreement with Mebel's RRKM results where c-C_3H is dominant at low collision energy, while l-C_3H dominates at collision energy larger than 25 kJ/mol. The high abundance of l-C_3H in our calculation is due to high l-C_3H yield in triplet PES and easy dissociation in triplet surface.

4.3 Summary and Conclusions

We presented results of surface hopping trajectory calculations of the $C(^3P)+C_2H_2 \rightarrow$ l-C_3H, c-C_3H, + H and C_3+H_2 reaction using both DFT triplet and singlet PES in full dimensionality constructed in our group before. Laudau-Zener transition probability was used for non-adiabatic purpose to calculate intersystem crossing. Calculations still found l-C_3H to be the dominant product over the collision energy range 5 to 50 kJ/mol, and C_3+H_2 channel was observed in dynamics as a result of ISC. About 40% of trajectories eventually switch from original triplet state to the singlet state, showing the important participation of singlet PES in the dynamics. High l-C_3H yield mainly from trajectories in the triplet state may drive us to revisit the triplet PES.

Chapter 5

Dynamics Calculation of the $OH+NO_2$ Association Reaction

5.1 Introduction

As the major sink of both HO_X and NO_X radicals, the reaction of OH with NO_2 and a third body to produce stable nitric acid, $HONO_2$,

$$OH + NO_2 + M \rightarrow HONO_2 + M \tag{5.1}$$

is a key radical chain termination step and of critical importance in atmospheric chemistry [30]. However, recent laboratory kinetics and spectroscopic experiments have reported evidence of a second channel to form a more weakly bound isomer of nitric acid, peroxynitrous acid, HOONO [31]-[32],

$$OH + NO_2 + M \rightarrow HOONO + M \tag{5.2}$$

Donahue *et al.* [31] used isotopically labeled reactants to present evidence for HOONO formation based on the scrambling of isotope composition of the OH and NO_2 decay products. Direct spectroscopic observation of gas-phase HOONO was reported by Nizkorodov *et al.* [32] using vibrational overtone photodissociation spectroscopy. Hippler *et al.* [33] also reported direct experimental evidence for the formation of HOONO and this group recently re-visited this reaction experimentally and also performed a modeling analysis of the fall-off behavior and high-pressure limit of reaction 5.1 and 5.2 [34].

A number of spectroscopic measurements have been reported to answer a key question about the branching between $HONO_2$ and HOONO. Lester and co-workers identified the *trans-perp* conformer of HOONO by action spectroscopy in the O-H overtone region, and preformed extensive detailed analysis of this isomer [35]- [37]. Bean *et al.* [38] identified *cis-cis* HOONO via intracavity ringdown spectroscopy, and reported a HOONO/$HONO_2$ rate constant ratio of 0.075 ± 0.02 at 295 K and 20 torr. Their results suggested that essentially all isomers had converted to the most stable *cis-cis* HOONO. However, Fry *et al.* [39] observed both stable conformers of HOONO, *cis-cis* and *trans-perp* and explored their isomerization dynamics using vibrational predissociation that follows the excitation of the first overtone of OH. Matthews *et al.* [40] concluded that the concentration of *trans-perp* HOONO is comparable to that of *cis-cis* HOONO at room temperature by analyzing the room temperature vibrational overtone action spectra of HOONO in the region of $2\upsilon_{OH}$ and $3\upsilon_{OH}$. Later they focused on the stated resolved unimolecular dissociation of *cis-cis HOONO*, and reported the bond dissociation energy [41]. Zhang *et al.* [42] measured the infrared absorption spectrum of matrix-isolated *cis-cis* HOONO, and six of nine fundamental vibrational modes have been assigned definitively.

The energetics and structures of HOONO isomers have been calculated using high-level ab initio methods [35]- [52]. Limited ab initio-based potential energy surfaces also have been constructed for theoretical investigation. McCoy *et al.* [51] reported a two-dimensional ab initio potential energy surface and dipole moment surface for *cis-cis* HOONO to study the coupling of the O-H stretch of HOONO to torsional modes. Schofield *et al.* [52] simulated the HOONO vibrational overtone spectrum using a three-dimensional local mode Hamiltonian. These reduced dimensionality potentials do not describe dissociation and thus they cannot be used to study the reactions 5.1 and 5.2.

Several groups have done sophisticated modeling analysis of these reactions, including the pressure dependence. Golden *et al.* [45] performed a multi-well master equation analysis of the various isomerization/dissociation and energy transfer processes utilizing new electronic structure calculations of relevant stationary points. They obtained the association rate constant by combining the equilibrium constant with the decomposition rate constant, obtained using RRKM theory. The pressure dependence of the HOONO and $HONO_2$ rate constants was modeled by adjusting several parameters to obtain good agreement with experiment. The resulting extrapolated high pressure-limit rate constant for HOONO was found to be about twice as large as the rate constant for $HONO_2$. Zhu and Lin [46] modeled the HO_2 + NO $\leftrightarrow$ OH+ NO_2 reactions. They characterized many minima and saddle points relevant to these reactions, including those associated with HOONO and $HONO_2$. Variational TST and RRKM calculations were performed and stabilization by energy transfer to a third body was determined by fitting the pressure-dependent experiments. The results obtained in this study are similar to those of Golden *et al.* The ratio of HOONO to $HONO_2$ rate constants was predicted to be as high as 15% under atmospheric conditions and the extrapolated high-pressure limit of the ratio of these rate constants is about 1.3 at 300 K. This ratio is smaller than the factor of 2 obtained

by Golden *et al.*, although in qualitative agreement that the ratio is larger than one. Most recently Hippler *et al.* [34] modeled reactions 5.1 and 5.2 using their newer data and a somewhat simpler approach than either Golden *et al* or Zhu and Lin. They obtained a ratio of 0.68 at 300 K for the high-pressure limits of these rate constants, in qualitative disagreement with the earlier modeling.

There have been very few dynamical studies of the OH+NO_2 reaction. This is a very challenging system to study and so these calculations were limited in scope or done with a large reduction in dimensionality. One of these was a quasiclassical trajectory (QCT) study using a model potential energy surface (PES) that was limited to a description of the $HONO_2$ complex and does not contain the HOONO complex [53]. Thus, this interesting study did not address the HOONO/$HONO_2$ branching. Williams *et al.* [54] developed a PES in two degrees of freedom for use in a quantum wavepacket study of the branching ratio between *cis-cis* HOONO and $HONO_2$. This 2D PES was used in a quantum wave packet adiabatic capture approximation calculation of the cross-sections to form the HOONO and $HONO_2$ complexes. This approximation does not provide information on the lifetime of these complexes; however, it does provide the rate constant for formation of the stable molecules in the high-pressure limit.

In this chapter we present a dynamical study of reactions 5.1 and 5.2, including all the HOONO isomers in full dimensionality. This is done by developing a global PES and performing dynamics calculations using it. In the next section we present the details of the electronic structure calculations that were used to obtain the PES. Following that we present relevant characteristics of the PES and compare them to previous high-level, single-point calculations and additional benchmark ab initio calculations that we performed in section 5.2. In section 5.3 we present the details and results of QCT calculations using this PES. These include association cross-

sections to form HOONO and $HONO_2$, analysis of the dynamics, in particular the role of a hydrogen bond (H-bond) complex in the association dynamics. A brief lifetime analysis of the various complexes is done. Comparisons to previous modeling calculations and the recyent reduced dimensionality dynamical calculations are also given in that section. A summary are given in section 5.4.

5.2 Potential Energy Surface Construction

5.2.1 Fitting details

The construction of the PES mainly employs procedures described in section 2.1. The PES, which is manifestly invariant under all permutations of like nuclei, is expressed in terms of polynomials of Morse-type variables y_{ij} given by $y_{ij} = exp(-r_{ij}/\lambda)$, where r_{ij} is the internuclear distance between nuclei i and j. For the present system there are 10 internuclear distances. The range parameter, λ, is fixed at the value 2.0 bohr. The Morse variables tend to a constant in the limit $r_{ij} \rightarrow \infty$ and so can describe reactive potential energy surfaces.

The database of electronic energies was constructed in stages. Initially we generated a widely dispersed set of geometries for which energies were computed at a low level of theory: the MP2 method using Dunning's valence double zeta (cc-pVDZ) basis. Some geometries were obtained by applying random nuclear displacements to the known $HONO_2$ and HOONO minima and other geometries; others were obtained by placing HO and NO_2 fragments in random relative position; yet others by re-labeling the nuclei of some other five-atom systems for which we had previously obtained potential energy surfaces. These low-level ab initio calculations were then used to fit an initial potential energy surface. On this initial low-level potential energy surface

we carried out classical molecular dynamics (MD) and diffusion Monte Carlo (DMC) runs, sampling geometries from these calculations. The newly generated geometries were added into the database for coverage of the full dimensional configuration space for the energies and geometries.

Due to the need to generate tens of thousands of electronic energies for a global PES we chose the efficient DFT B3LYP/6-311G(d,p) approach for this system. As is well known, the DFT calculations are unreliable in regions of configuration space where the electronic wave function has multi-reference character. In general this is where bonds are being made/broken. This method cannot reliably describe open-shell singlet systems, like OH+NO_2. We dealt with this by simply discarding suspect energies from the data set used in the fit. Operationally we identified these regions by noting poor agreement between fits that were done using all the energies and outliers to the fit. Upon inspection it was determined that the outliers were indeed unreliable DFT energies and they were subsequently eliminated from the set of energies to be fit. We compare one-dimensional bond-breaking cuts starting from various points with corresponding CASPT2/aug-cc-pVTZ calculations to make sure that interpolation between complex and asymptotic region without the unreliable DFT will produce correct and smooth cuts.

For the final fit 55471 energies were used. The configurations include the separated OH + NO_2 fragments, the complex regions, and the fragments HO_2 + NO. The potential is of total order six and contains 1603 terms; the associated coefficients were obtained by standard linear-least squares fitting to all the data. The data were weighted by a simple function 0.1/(0.1+E), where E is in hartree, measured relative to the $HONO_2$ global minimum. The RMS fitting error is 0.51 kcal/mol for energies up to 63 kcal/mol.

5.2.2 Properties of the PES

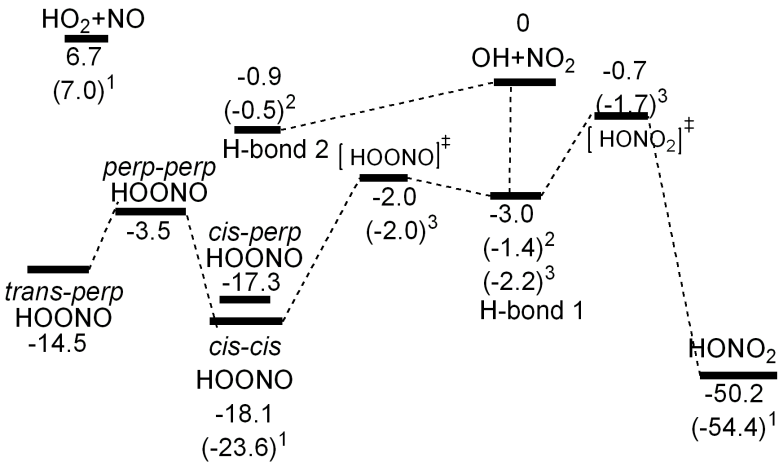

Figure 5.1 Energies (kcal/mol) of indicated stationary points, including the two H-bond complexes for the OH+NO_2 reaction from the present potential energy surface and various single point calculations, [1]ref. [43], [2]present CASPT2/aug-cc-pVTZ calculations, [3]present DFT-B3LYP/6-311G(d,p)-calculations.

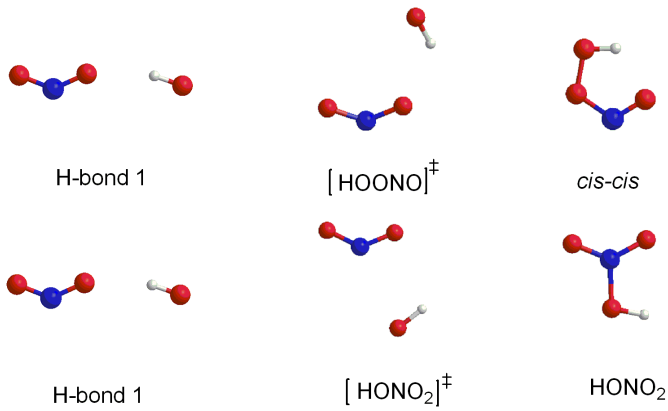

Figure 5.2 Structures of H-bond complex 1, saddle point for HOONO, denoted [HOONO], and *cis-cis* HOONO; structures of H-bond complex 1, saddle point for $HONO_2$, denoted [$HONO_2$], and $HONO_2$.

The geometries, energies, and harmonic frequencies of various stationary points on the PES were determined and are compared with previous high-level ab initio calculations in Figure 5.1-5.3 and Table 5.1 and 5.2. Two H-bond complexes were located on the PES and subsequently confirmed using new DFT calculations. We also performed multi-reference CASPT2/aug-cc-pVTZ calculations to verify the accuracy of

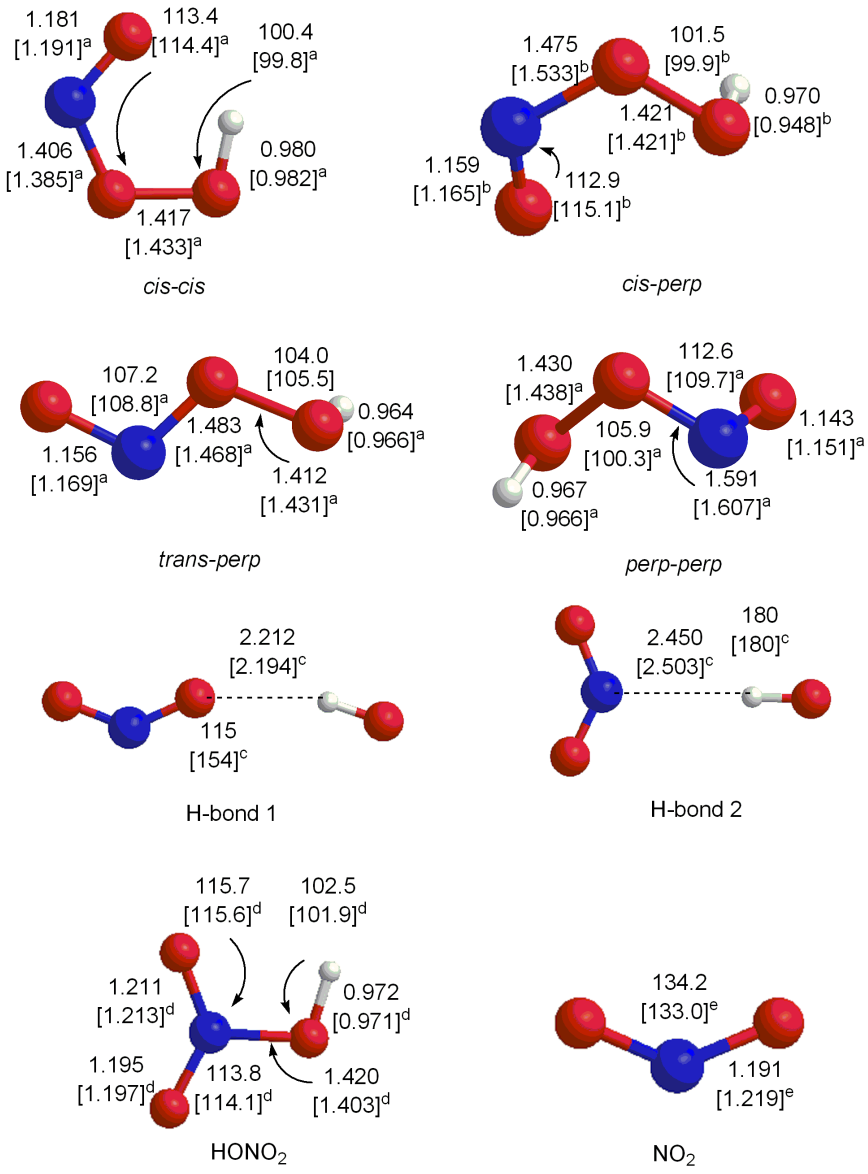

Figure 5.3 Structures of indicated stationary points. The top values are from the PES and the values in squares are from various high-level ab initio calculations. [a]ref. [39], [b]ref. [47], [c] present CASPT2/aug-cc-pVTZ calculations, [d]ref. [49], [d]ref. [50]. Units are Angstroms and degrees .

the PES characterization of these complexes. These multi-reference calculations were also done along several one-dimensional cuts to test the smoothness of the PES. The orbitals used in the CASPT2 calculations were taken from MCSCF calculations. In the case of the HOONO isomers, $HONO_2$ and one-dimensional dissociation curves the MCSCF and CASPT2 calculations employed active spaces that consisted of 19 occupied orbitals of which 8 were constrained to be doubly occupied, and the 4 1s orbitals were kept frozen in the CASPT2 calculations. For the hydrogen-bonded complexes a minimal active space consisting of 17 orbitals in which 14 were doubly occupied was used. The CASPT2 binding energies of the hydrogen-bonded complexes were calculated with a super-molecule approach to minimize size consistency errors and the standard counterpoise correction was added to account for basis set superposition error.

As seen from these figures and tables the PES describes all stationary points with good accuracy. Also note that the PES energies of the *trans-perp* and *perp-perp* isomers relative to *cis-cis* HOONO are 3.6 and 14.6 kcal/mol, respectively, which agree well with the CCSD(T)/cc-pVQZ//CCSD(T)/cc-pVTZ values of 3.7 and 14.6 kcal/mol, respectively [39].

The H-bond complexes are, as expected, much less deep than the HOONO and $HONO_2$ complexes. H-bond complex 1 was reported previously by Houk *et al.* [44], who performed DFT B3LYP/6-31G* calculations. These complexes may also correspond to Wells 2 and 3 in the recent reduced dimensionality PES of Williams *et al* [54]. The present CASPT2 calculations confirm the existence of these complexes and indicate the semi-quantitative accuracy of the PES and underlying DFT calculations, shown in Figure 5.1 and 5.3. A normal-mode analysis of complex 1 from the PES and direct DFT calculations is given in Table 5.2, along with analysis of two associated

Table 5.1 Harmonic vibrational frequencies (cm^{-1}) of stationary points for the OH+NO_2 reaction from the PES and ab initio calculations.

cis-cis	*cis-cis*	*trans-perp*	*trans-perp*	*perp-perp*	*perp-perp*	*cis-perp*	*cis-perp*
PES	CCSD(T)[a]	PES	CCSD(T)[a]	PES	CCSD(T)[a]	PES	DFT
286	383	193	211	239i	233i	191	178
431	523	327	302	322	288	381	324
504	419	449	366	379	384	430	389
676	723	530	497	418	468	538	460
919	838	790	816	667	702	854	832
982	969	1135	992	982	906	961	962
1415	1458	1513	1412	1501	1374	1446	1382
1676	1630	1805	1736	1931	1794	1812	1806
3607	3521	3915	3780	3838	3774	3845	3736
$HONO_2$	$HONO_2$	HO_2+NO	HO_2+NO	OH+NO_2	OH+NO_2		
PES	QCISD(T)[b]	PES	DFT	PES	DFT		
472	477	1180	1163	839	766		
629	576	1539	1427	1407	1399		
674	644	3739	3610	1695	1706		
865	762	1990	1988	3780	3704		
983	892						
1325	1337						
1374	1360						
1768	1786						
3609	3738						

[a]ref. [39], [b]ref. [45]

saddle points. As seen there are several low-frequency modes which signal that this complex and associated saddle points to enter the HOONO and $HONO_2$ wells are quite floppy. Thus, it is not surprising that the agreement between the PES and our CASPT2 characterization of the structure of this H-bond complex is only semi-quantitative. Our focus on complex 1 is due to its importance in the quasiclassical dynamics of the association reaction, as described in detail in the next section. For that reason we also located and characterized saddle points of H-bond 1 complex

Table 5.2 Harmonic frequencies of the H-bond complex 1, two associated saddle points and energies (kcal/mol) relative to the complex minimum.

H-bond 1 PES	H-bond 1 DFT	$[HOONO]^{\ddagger}$ PES	$[HOONO]^{\ddagger}$ DFT	$[HONO_2]^{\ddagger}$ PES	$[HONO_2]^{\ddagger}$ DFT
15	37	52i	14i	104i	64i
28	62	72	77	82	72
125	113	130	112	105	111
309	276	181	217	217	221
342	284	298	250	368	248
796	769	810	769	825	768
1388	1398	1364	1398	1381	1396
1703	1706	1684	1716	1660	1709
3820	3688	3754	3684	3676	3700
Energy					
0.0	0.0	1.0	0.2	2.3	0.5

and that information is given in Table 5.2. These saddle points are also quite floppy, as expected. However, the barrier to the HOONO well is smaller than the one to $HONO_2$ well, suggesting a preference for decay into HOONO than $HONO_2$ and this is consistent with the QCT calculations presented below.

To determine the reality of the PES in regions where the DFT method is problematic we compare one-dimensional cuts starting from the PES optimized HOONO and $HONO_2$ stationary points and separating to OH+NO_2 along the O-O coordinate, with all other degrees of freedom fixed, with corresponding CASPT2/aug-cc-pVTZ calculations. The comparisons shown in Figure 5.4 for four cuts indicate that the PES describes this dissociation smoothly and realistically.

To conclude this section on the PES we note that the endoergic products HO_2 + NO are also described by the PES and the energy of these products relative to reactants OH+NO_2, shown in Figure 5.1 is, somewhat in quite good agreement with high level ab initio calculations. Also the PES reproduces the direct DFT normal mode

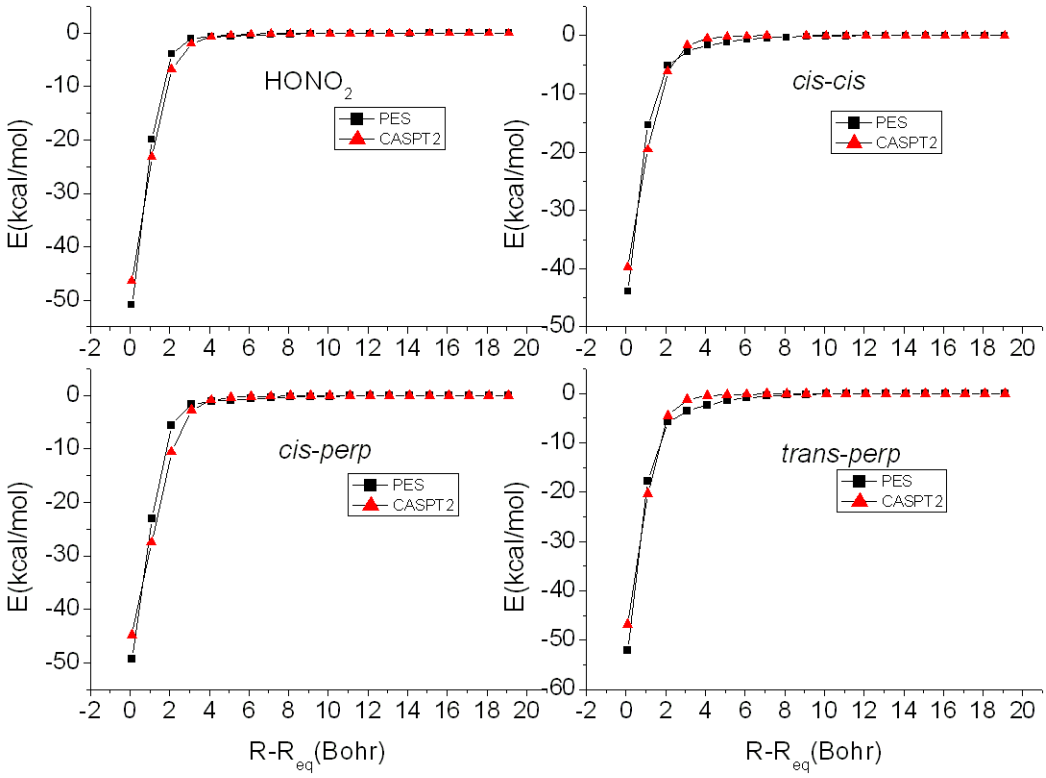

Figure 5.4 Comparison of one-dimensional cuts from the PES and CASPT2/aug-cc-pVTZ calculations starting from the minima indicated to OH+NO_2 a function of the OO distance, denoted R relative to the value at the PES minimum, denoted R_{eq}.

frequencies of these products to within 0.1 to 8%. Note that these products are not accessible for the collision energies considered in the QCT calculations described next, except at the highest energy, where they are formed with very small probability.

5.3 Quasiclassical Trajectory Calculations

5.3.1 Details of the calculation

The calculation setup mainly employs standard procedures described on chapter 2. The QCT calculations using this PES were done from 0.12 to 2.4 kcal/mol initial relative collision energy to determine the cross-sections and details of the dynamics to form $HONO_2$ and HOONO complexes from OH+NO2 reactants in the ground ro-vibrational states. In brief, a normal mode analysis was done for the OH and NO_2 reactants and they were each given harmonic zero-point energy. Then random sampling was done from each normal mode in the usual fashion. Adjustments were then made to the momenta to enforce zero angular momentum for each reactant. The trajectories were propagated with a small time-step of 3 atomic units (roughly 0.07 fs) and with the Verlet methods, which conserves energy for very long-time propagation. One thousand trajectories were performed for each impact parameter, b, and collision energy, E_{coll}, to determine whether complexes were formed. The criterion for formation of a specific complex is the usual one, i.e., long-lived trajectories followed by an identification of the configuration of atoms. We used the time dependence of the distance between the centers of mass of OH and NO_2, denoted R(t), to monitor complex formation. For a simple, direct interaction this distance would decrease monotonically with time as the OH and NO_2 approach from an initial large separation, reach a minimum, and then increase monotonically as the OH and NO_2 separate. For complex-forming trajectories R(t) exhibits multiple turning points and for the

purpose of detecting complex formation we adopted the usual condition of a least one oscillation in R(t). When complex-formation is found geometric conditions are applied to identify the complex and the time dependence of that complex is followed. Formation of several complexes during the course of single trajectory can thus be determined as well as the associated lifetime. The maximum impact parameter, b_{max}, for complex formation was determined at each collision energy and impact parameters between 0 and b_{max} were sampled with a step size of 0.5 bohr. A total of roughly 165 000 trajectories were run for a maximum time of approximately 14 ps.

5.3.2 Results and Discussion

Examination of trajectories in the important low-energy regime indicated very common transient H-bond complex 1 formation. We did not observe significant transient formation of H-bond complex 2 and so we do not consider this complex further. A significant fraction of these pre-reactive H-bond complexes decay into either the HOONO or $HONO_2$ wells. When this occurs we observe very little isomerization between $HONO_2$ and HOONO; however, we do find facile isomerization among the HOONO isomers, in agreement with previous expectations [39]. We did observe some interesting, rare HOONO/$HONO_2$ isomerization events that will be described briefly at the end of this section.

An example of a typical complex-forming trajectory is shown in Figure 5.5, where R(t) is plotted versus time. As seen a complex forms first at long range (in fact the H-bond complex 1) for roughly 4 ps, followed by formation of a second complex (in fact HOONO) which dissociates back to OH+NO_2 after roughly 6 ps. Figure 5.6 shows the impact parameter dependence of the probability to form complexes for E_{coll} = 0.12 kcal/mol. As seen the probability to form H-bond 1 is much larger than to form HOONO or $HONO_2$ and the probability to form HOONO is roughly twice the

probability to form $HONO_2$. Clearly more than half the H-bond 1 complexes decay directly to OH+NO_2 without subsequently forming HOONO or $HONO_2$.

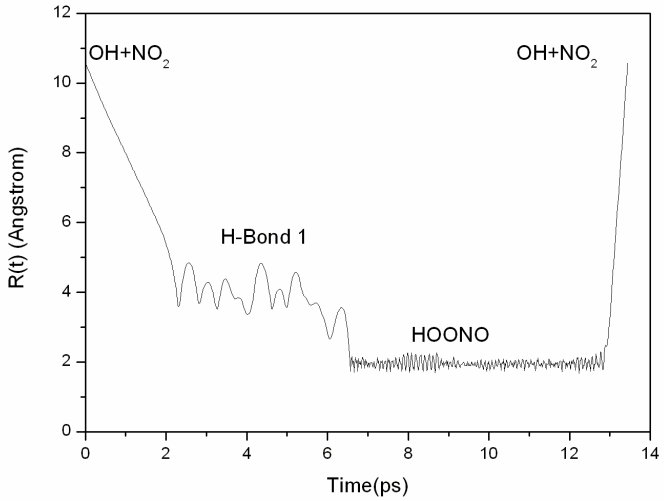

Figure 5.5 Time evolution of the distance between the OH and NO_2 centers of mass for a trajectory that illustrates H-bond complex 1 formation and subsequent HOONO complex formation and finally dissociation back to OH + NO_2.

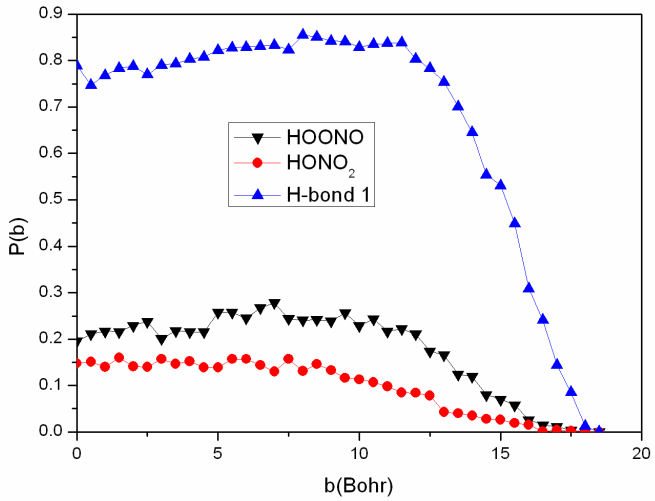

Figure 5.6 Impact parameter dependence of the probability to form H-bond complex 1, HOONO (all isomers) and $HONO_2$ for an initial relative collision energy of 0.12 kcal/mol.

A plot of the total cross-section to form the H-bond 1 complex versus E_{coll} is shown in Figure 5.7. This cross-section is split into non-reactive and reactive components, where reactive denotes the cross-section for the H-bond complex to decay into either HOONO or $HONO_2$ complexes and non-reactive denotes decay back to reactants without HOONO or $HONO_2$ complex formation. As seen all cross-sections decrease with E_{coll}, as expected for these barrier-less association processes. The non-reactive component of the total cross-section is roughly twice the reactive one at the lowest collision energies and at the higher energies it becomes much larger than the reactive one. We examined the corresponding HOONO and $HONO_2$ components of the reactive part of the total H-bond cross-section and find (as expected based on the results in Figure 5.6 that the HOONO component is larger than the $HONO_2$ one. This result is qualitatively consistent with properties of the two saddle points of the H-bond 1 complex shown in Table 5.2. However, not all HOONO or $HONO_2$ complexes are formed via the pre-reactive H-bond 1 complex. To investigate the significance of the reactive component of H-bond complex to HOONO and $HONO_2$ complex formation we plot in Figure 5.8 the energy dependence of the fraction of the number of trajectories that form HOONO and $HONO_2$ complexes via the H-bond 1 complex. As seen the fraction for HOONO is larger than for $HONO_2$ at low collision energies. The fractions for both HOONO and HONO2 decrease rapidly with increasing E_{coll}. This decrease mirrors the decrease in the cross-section of the H-bond complex with increasing E_{coll}.

The energy dependence of the cross-section to form HOONO and $HONO_2$ complexes is plotted in Figure 5.9. In this figure, the error bars shown were determined by running batches of trajectories with different random initial conditions. The full set of trajectories was used subsequently for analysis and results based on these analyses are shown without error bars. As seen the cross-section to form HOONO is greater than the one to form $HONO_2$ at low collision energies; however, the two

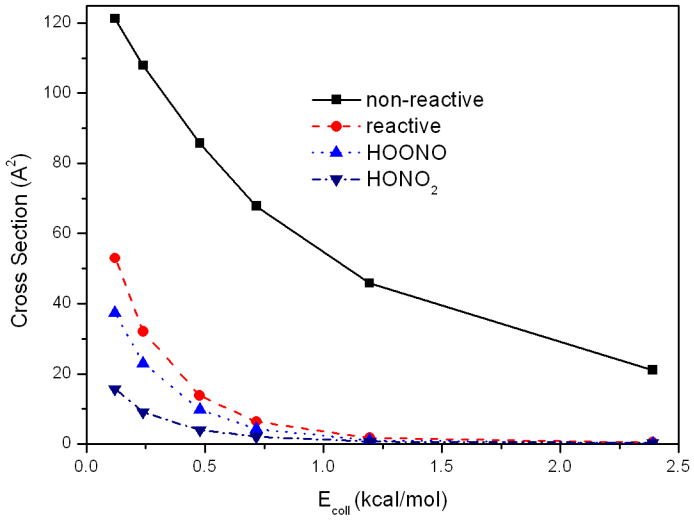

Figure 5.7 Collision energy dependence of the total cross-section to form H-bond complex 1 and its reactive and non-reactive component cross-sections as defined in the text.

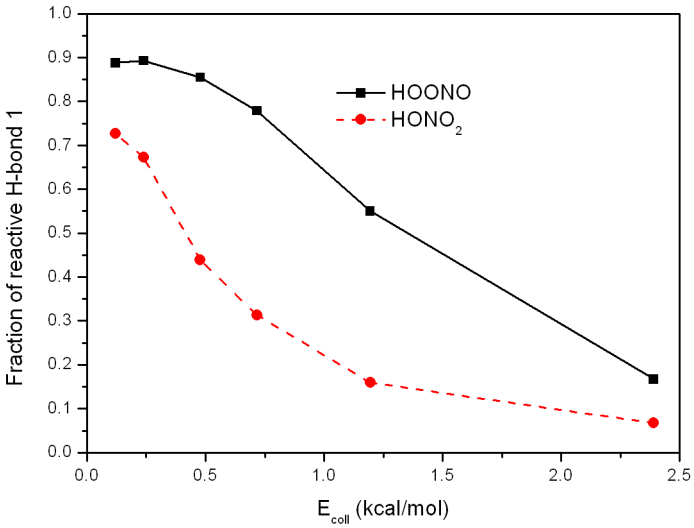

Figure 5.8 Energy dependence of the fraction of trajectories forming $HONO_2$ or HOONO with H-bond complex 1 as a precursor.

cross-sections cross at roughly E_{coll} = 0.75 kcal/mol. Both cross-sections exhibit an E_{coll}^{-q}(q > 0) energy dependence, as expected. Comparing Figure 5.9 with Figure 5.8, it is clear that the contribution of the H-bond complex to the HOONO and $HONO_2$ complexes is dominant at low collision energies, but decreases significantly at energies, where in fact the $HONO_2$ cross-section is larger than the HOONO one. Clearly the detailed collision mechanism for HOONO and $HONO_2$ formation is energy dependent and is dominated by the pre-reactive H-bond complex at low collision energies but largely independent of this complex at higher energies. We will investigate this a bit further below where we consider the energy dependence of the lifetimes of these complexes. The cross-sections for HOONO and HONO2 shown in Figure 5.9 were also obtained in two versions of the approximate reduced dimensionality quantum calculations of Williams *et al.* for non-rotating reactants. The preferred, WCA cross-sections are roughly a factor of two larger than the present QCT ones. There may be several sources of this disagreement. One significant one is the role of the H-bond

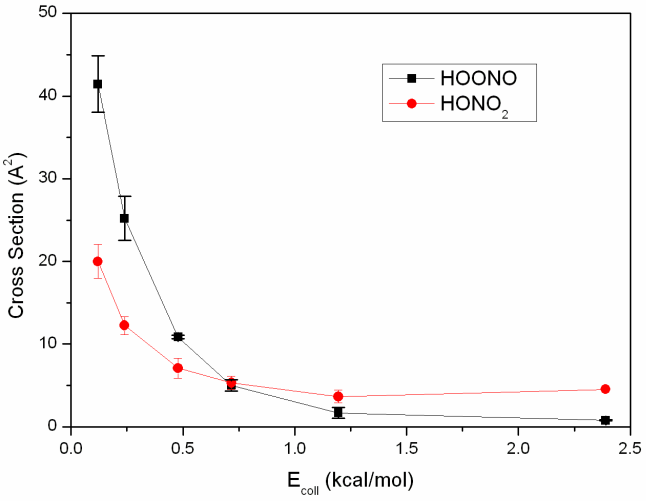

Figure 5.9 Association cross-section for HOONO (all isomers) and $HONO_2$ as a function of the initial relative collision energy for ground ro-vibrational states of the reactants OH and NO_2.

complex. In the present calculations we find that this complex dominates the reaction dynamics at low collision energies, and from Figure 5.6 it is clear that formation of this complex largely leads subsequently to non-reactive decay. The effect of this is to reduce the reactive cross-sections significantly and this may be the major source of the disagreement with the reduced dimensionality quantum capture calculations which probably do not accurately describe the effect of this H-bond complex. Interestingly though these approximate quantum cross-sections do agree qualitatively with the present QCT ones in finding that the cross-section to form HOONO is larger than the one to form HONO2 at very low collision energies with a reversal at higher collision energies. The energy where the two cross-sections are equal is lower in the approximate quantum calculations, however.

The cross-sections shown in Figure 5.9 were fit to the form A E_{coll}^{-q} and then used to obtain estimates of the high-pressure limit rate constants for HOONO and $HONO_2$. We stress these are just estimates because the cross-sections in Figure 5.9 are for ground ro-vibrational states of the reactants. With this caveat in mind the rate constants were obtained as usual from the expressions

$$k(T) = (\frac{8}{\pi\mu})^{1/2} \frac{1}{(k_B T)^{3/2}} \int_0^\infty Q_R(E_{coll}) E_{coll} e^{-E_{coll}/k_B T} dE_{coll} \tag{5.3}$$

which for the power-law fit to the cross-sections gives the analytical result

$$k(T) = (\frac{8}{\pi\mu})^{1/2} (k_B T)^{1/2-q} A\Gamma(2-q) \tag{5.4}$$

We give the results in table 5.3 and to indicate the sensitivity to the extrapolations to $E_{coll} = 0$ and ∞ we also give results obtained numerically over the range where the cross-sections were obtained. Note the results in that table include the factor $1/Q_{elec}(T)$, where the electronic partition function, $Q_{elec}(T)$, is given by 2+2exp(-

205/T) [54]. We adopt this expression for Q_{elec} here to be consistent with Williams *et al.*; however, we note that Liu *et al.* include an electronic contribution from NO_2 which at the temperatures of interest here would increase Qelec by a factor of 2. Table 5.4 includes rate constants from the modeling calculations and the approximate quantum calculations. They all agree semi-quantitatively with each other and with the present results in finding the rate constants for HOONO and $HONO_2$ being roughly equal. The present results are below all of the previous ones, and in particular below the one approximate dynamical calculation by roughly a factor of 2.3. This factor is larger than the factor of 2 or so noted above in the comparison of cross-sections and so perhaps some of this difference is due to the present result not being properly thermally averaged over initial states of the reactants. (We have not included the result from Liu *et al.* in this table because their QCT calculations were for the $HONO_2$ complex only. Nevertheless it is interesting to note their result of 0.7±.3 (-11) cm^3s^{-1} at 300 K, which without the additional electronic factor of two (noted above) would be 1.4±.6 (-11) and quite close to the present result for the total rate constant. We think is mainly fortuitous because the PES used in that work did also not contain the H-bond complex that as we have seen causes substantial non-reactivity of the association dynamics.)

Table 5.3 Fitting parameters to the function of A E_{coll}^{-q} for HOONO and $HONO_2$ cross-section.

	A	q	R^2
HOONO	3.2609 10^{-40}	1.00175	0.97743
$HONO_2$	7.2903 10^{-34}	0.68468	0.97596

To conclude this section we briefly consider the lifetime distributions of the complexes. The lifetime distribution of H-bond complex 1 is shown in Figure 5.10 for two collision energies that span the range of the energies considered here. In this figure

Table 5.4 rate constants($10^{-11}cm^3s^{-1}$) and comparison with previous results at 300 K.

Rate constant	430 K	430K	300k	300 K	250 K	250k
	HOONO	$HONO_2$	HOONO	$HONO_2$	HOONO	$HONO_2$
Analytical[a]	5.1	3.9	6.1	4.2	6.7	4.3
Numerical[b]	4.1	3.3	4.9	3.7	5.2	3.8
Averagec[c]	1.4	1.1	1.7	1.2	1.8	1.3
Ref. [34]			1.9	2.8		
Ref. [45]			5.3	2.7		
Ref. [46]			6.0	4.7		
Ref. [54]			2.8	4.0		

[a] From the power law fit and analytical integration from 0 to ∞
[b] From numerical integration from 0.119 to 2.39 kcal/mol.
[c] Includes factor of $1/Q_{elec}(T)$

the fraction plotted is of the fraction of the total number of H-bond 1 complexes at the indicated energy. Note from Figure 5.7 the cross-section for H-bond 1 formation decreases markedly over this energy range and so the number of H-bond complexes at E_{coll} = 2.4 kcal/mol is much less than at 0.12 kcal/mol. And, as seen in Figure 5.10 the lifetime shortens considerably at the higher energy. This behavior is expected based on the usual statistical arguments. The lifetime distributions of the HOONO and $HONO_2$ complexes are more challenging to obtain because they are much deeper wells than the H-bond 1 one and therefore the lifetimes are much longer. As noted above the trajectories reported here were followed for a maximum of 14 ps, which was sufficient to obtain the association cross-sections; however, this maximum propagation time is not sufficiently long to determine quantitative lifetime distributions of HOONO and $HONO_2$ complexes. We did determine the fraction of HOONO and $HONO_2$ complexes undissociated after 14 ps and these fractions are plotted in Figure 5.11 as a function of E_{coll}. As seen a much larger fraction of $HONO_2$ complexes remain undissociated than HOONO complexes over this energy range. Also note that less than half of the $HONO_2$ complexes dissociate after 14 ps. This is in accord with sta-

tistical expectations since $HONO_2$ is significantly more deeply bound than HOONO. As noted in the Introduction Liu *et al.* [53] determined the lifetime distribution of $HONO_2$ in their QCT study of the OH+NO_2 interaction on a PES which does not contain the HOONO isomers. They reported lifetimes for $HONO_2$ as a function of the total energy and also for vibrational state-selected reactants. From Figure 7 of that paper the 1/e lifetime, τ, for ground vibrational state reactants is roughly 40 ps. That lifetime is consistent with the present, limited results for $HONO_2$, which show that 50% or more of $HONO_2$ is un-dissociated after 14 ps.

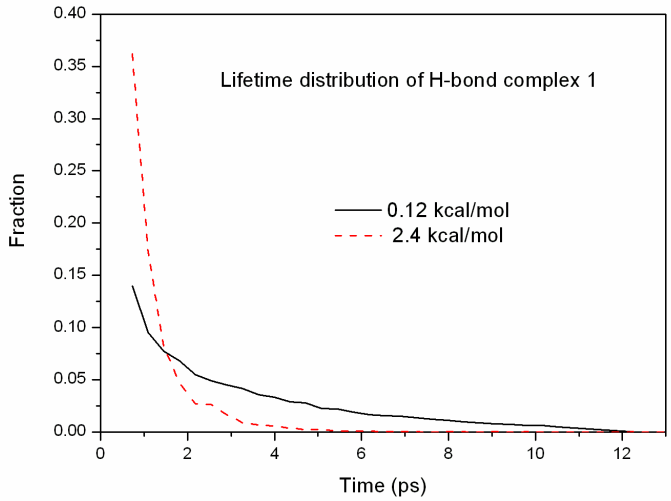

Figure 5.10 Lifetime distribution of the H-bond complex 1.

Finally, we note that a small number of trajectories exhibit HOONO/$HONO_2$ isomerization by a mechanism where HOONO begins to dissociate to OH+NO_2 but undergoes a change in relative velocity while the incipient OH rotates bringing the incipient fragments to the more stable $HONO_2$ complex. Figure 5.12 illustrates this by plotting R(t) versus time for one such trajectory. This mechanism appears to be somewhat different from the H-atom hopping reported in a recent semi-empirical direct-dynamics study of the reverse isomerization, $HONO_2$ to HOONO, induced by

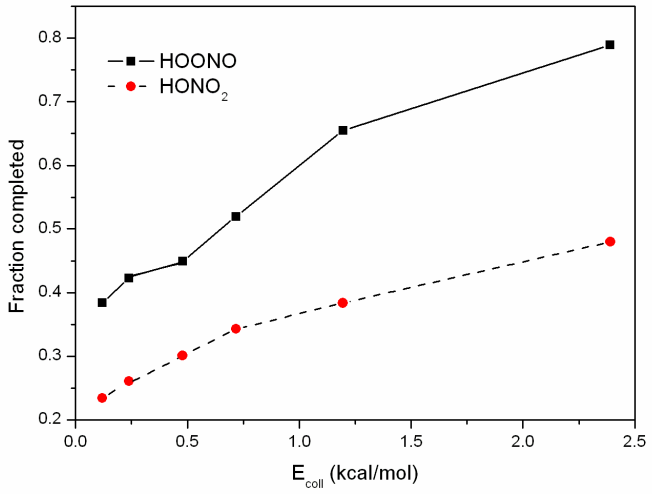

Figure 5.11 fraction of HOONO and $HONO_2$ complexes that dissociate within 14 ps or less as a function of the collision energy.

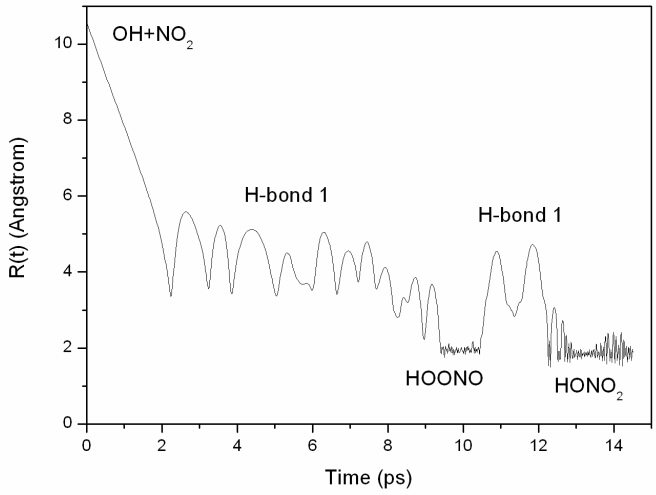

Figure 5.12 R(t) versus t for a rare trajectory showing HOONO → $HONO_2$ isomerization.

high overtone excitation of the O-H stretch of HONO2 [55]. Also, we observed scrambling among the O atoms in $HONO_2$ but virtually none in HOONO. The former result is consistent with experiments done with O-atom isotopes [31], which were among the first to present experimental evidence, albeit indirectly, for the existence of the HOONO isomer.

5.4 Summary and Conclusions

We presented a global DFT B3LYP/6-311G(d,p)-based potential energy surface in full dimensionality for OH+NO_2, which describes $HONO_2$, HOONO, HO_2+NO, and two H-bond complexes in the OH+NO_2 entrance channel. Standard analysis of stationary points, i.e., energies, structures, and normal mode frequencies, was done and compared with previous high-level ab initio calculations. Two hydrogen-bond complexes were found on the PES and verified by multi-reference CASPT2/aug-cc-pVTZ calculations.

The PES is invariant with respect to permutation of like nuclei, which is essential for a realistic description of the dynamics of this system. Quasiclassical trajectory calculations were done to describe the association reaction for OH and NO_2 in their ground ro-vibrational states. The importance of one H-bond, pre-reactive complex for the association was found, especially for low energy collisions. This complex decays preferentially directly to the reactants, but also decays to HOONO and HNO_2, with approximately a two to one preference for HOONO. This pre-reactive complex is similar to ones reported previously involving an OH reactant [56], [57].

Association cross-sections for $HONO_2$ and HOONO were calculated as a function of the initial relative kinetic energy. At energies below 0.75 kcal/mol the HOONO cross-section is larger than the $HONO_2$ one, however, the reverse is found above this

energy. This result agrees qualitatively with a very recent approximate quantum calculation of the association cross-section done in two degrees of freedom and also based on adiabatic capture theory. These cross-sections were used to estimate the high-pressure limit association rate constants. Comparisons with previous results were made, with the caveat that the present ones are not properly thermally averaged. With this caveat in mind the present results were below previous modeling ones by about a factor of 3.

Lifetime distributions of the H-bond complex and a limited analysis of the lifetimes of the HOONO and $HONO_2$ complexes were presented. As expected the lifetime of the H-bond complex is shorter than HOONO and $HONO_2$ lifetimes, and the more deeply bound $HONO_2$ was found to have a longer lifetime than HOONO. Very little HOONO/$HONO_2$ isomerization was found in the dynamics calculations; however, the isomerization observed occurs when a HOONO complex has begun to dissociate but reaches a turning point at large distance and return to the complex region of $HONO_2$. Facile O-atom scrambling was observed for $HONO_2$ but not for HOONO.

Chapter 6

Path Integral Monte Carlo Calculation of CH_5^+ and $CD_3H_2^+$

6.1 Introduction

6.1.1 CH_5^+ and $CD_3H_2^+$

The molecule CH_5^+ is of great interest for its highly fluxional property. In terms of dissociation property, the reaction

$$CH_3^+ + HD \rightarrow CH_2D^+ + H_2 \tag{6.1}$$

is a important interstellar reaction.

Recently a full-dimensional, ab initio-based potential energy surface(PES) for CH_5^+ has been reported. The PES excellently covers the global minimum, and asymptotic CH_3^++H_2 areas. The current ab-initio high-level calculation shows that the corresponding minimum is a Cs structure characterized as a CH_3 tripod with a "H_2"

attached to the carbon. Diffusion Monte Carlo calculations are performed based on the PES for the zero-point energy of CH_5^+ and isotopologs like $CD_3H_2^+$. Since we want to explore the scrambling behavior of hydrogen atom, Path Integral Monte Carlo Methods are used to calculate various bond distance distribution of CH_5^+ or $CD_3H_2^+$ at different temperature. In addition, the fitted zero-point energy will be presented.

6.1.2 Path Integral Monte Carlo Method

The path integral can be illustrated in a single line:

$$< x_f, t_f | x_i, t_i >= \int Dx(t) e^{iS[x(t)]/\hbar} \tag{6.2}$$

If you want to know the quantum mechanical amplitude for a particle at a initial position x_i at time t_i to reach a final position x_i at time t_i , you need to integrate all the possible paths connecting the two points with a weight given by the classical action :

$$S[x(t)] = \int_{t_i}^{t_f} dt L(x(t), \dot{x}(t)) \tag{6.3}$$

for each path. if you take the limit $\hbar \to 0$, the only contribution from classical path is expected. but when $\delta S \simeq \hbar$, the path is "fuzzy". Around the classical path, a quantum particle explores the vicinity, which also contributes to the path integral.

Then we define the quantity $K(x_f, t_f; x_i, t_i)$

$$K(x_f, t_f; x_i, t_i) =< x_f, t_f | x_i, t_i > \tag{6.4}$$

as a propagator . If we know this quantity, we know everything about what happens to the wavefunction, since

$$\begin{aligned}\psi(x_f,t_f) &= < x_f,t_f|\psi >= \int < x_f,t_f|x_i,x_t > dx_i < x_i,t_i|\psi > \\ &= \int K(x_f,t_f;x_i,t_i)\psi(x_i,t_i)dx_i \end{aligned} \tag{6.5}$$

In one case, suppose that the Hamiltonian does not depend on the time, The propagator can be expressed in terms of eigenvalue and eigenstates as:

$$\begin{aligned}K(x_f,t_f;x_i,t_i) &=< x_f|e^{-iH(t_f-t_i)/\hbar}|x_i > \\ &= \sum_n < x_f|n > e^{-iE_n(t_f-t_i)/\hbar} < n|x_i > \\ &= \sum_n e^{-iE_n(t_f-t_i)/\hbar}\psi_n^*(x_f)\psi_n(x_i) \end{aligned} \tag{6.6}$$

If we go back to the expression of partition fucntion

$$Z = \int dx\rho(x,x) = \int dx \sum_n e^{-E_n\beta/}\psi_n^*(x)\psi_n(x) \tag{6.7}$$

we can see the two equations are the same if $\beta = -i(t_f - t_i)/\hbar$

Because the kinetic energy term does not commute with the potential term in Hamiltonian, the slicing trick is used to obtain the partition function for a small infinite time interval as below:

$$\Phi(x_1,\cdots,x_p) = \frac{m}{2\hbar^2\Delta\beta\beta}\sum_{k=1}^{P}(x_k - x_{k+1})^2 - \Delta\beta\sum_{k=1}^{P}V(x_k) \tag{6.8}$$

$$Z \approx c\int dx_1\cdots dx_p exp\left(-\beta\Phi(x_1,\cdots,x_p)\right) \tag{6.9}$$

6.1.3 Path Integral Monte Carlo Algorithm

1) The basic algorithm for one main cycle

   1. choose a segment of the chains containing j links, e.g $x_1 \cdots x_{j+1}$
   2. generate $x_2 \cdots x_j$ using staging transformation
   3. accept the new configuration if r < min(1,w)

$$w = exp(-\Delta\beta \sum_{k=2}^{j} [V(x_k^{new}) - V(x_k)]) \tag{6.10}$$

   4. go to step 1 until P/j have been tried
   5. update

2) Sample Input file

```
**********************************************************************
6
C     0.000000000     0.000000000     0.000000000     12.0d0
H     0.080523472     1.107547444     0.000000000     1.007825d0
H     0.946274186    -0.735562791     0.000000000     1.007825d0
H     1.180245021     0.193484407     0.000000000     1.007825d0
H    -0.442927758    -0.326101602    -0.938878443     1.007825d0
H    -0.442927758    -0.326101602     0.938878443     1.007825d0
300              !temperature
7               ! power of slicing
25              ! segment
100000           ! number of main cycle
20000            ! number of initial cycle to update the value
**********************************************************************
```

3) Input variables

Basically, first set *segment value* $j = 0$, making acceptance ratio as high as 0.95, Then increase j to decrease the ratio between 0.2 and 0.5. In order to keep $\Delta\beta$ to be constant for different temperature, I just cut half of the temperature when the slicing doubles.

Table 6.1 Input parameters for PIMC calcualtin of CH_5^+

T(k)	P(power)	j	acc ratio
4.6875	13	25	0.297
9.375	12	25	0.297
18.75	11	25	0.298
37.5	10	25	0.297
75	9	25	0.298
150	8	20	0.204

6.2 Results and Discussion

At each temperature, we perform the calculation five times recording the bond length distribution and average kinetic estimator of energy. Then do the fit for the mean energies at different temperature to get the value at 0K, namely zero point energy of the molecule. Finally we compare the bond length distribution at different temperature.

6.2.1 CH_5^+

1) Zero Point Energy Calculation

The error bar calculations are presented in Figure 6.1, with fairly large one for high temperature. Then the mean values of corresponding energies are successfully fitted to the form of first order exponential decay. Zero point energy

from this calculation is 10911 cm^{-1}, shown in Figure 6.2, excellently close to the number 10917(3)cm^{-1} reported by Zhong Jin *et al* [58]

2) H-H bond length distribution

Our results in Figure 6.3 excellently reproduce the distribution from Diffusion Monte Carlo method by McCoy *et al* [59]. One feature is that when the temperature goes up, the distribution curve does not change too much.

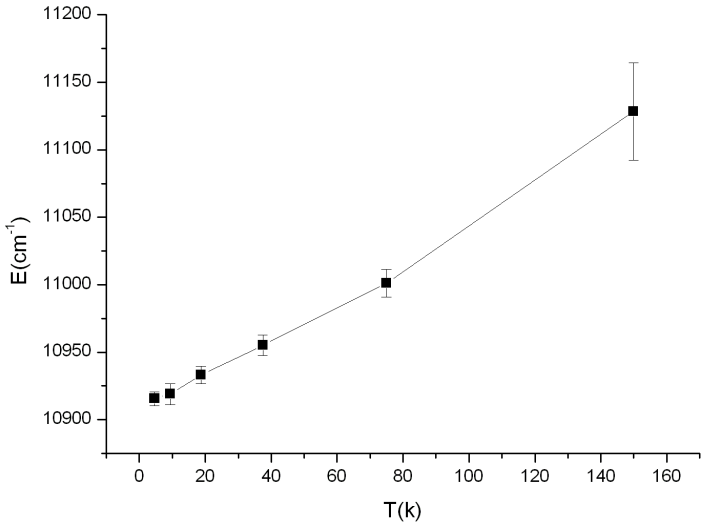

Figure 6.1 Average kinetic estimator of energy of CH_5^+ at different temperature

6.2.2 $CD_3H_2^+$

1) Zero Point Energy Calculation

The same procedure as that of CH_5^+ is applied, shown in Figure 6.5 and 6.6, to get the zero point energy as 9083 cm^{-1}, also excellently close to the number 9097(6)cm^{-1} reported by Zhong Jin *et al* [58]

2) Bond Distance Distribution at fairly low temperature 4K

In this deuterium case, we will randomly select which two hydrogen will be the hydrogen atoms of normal mass. Ten calculations have been performed at

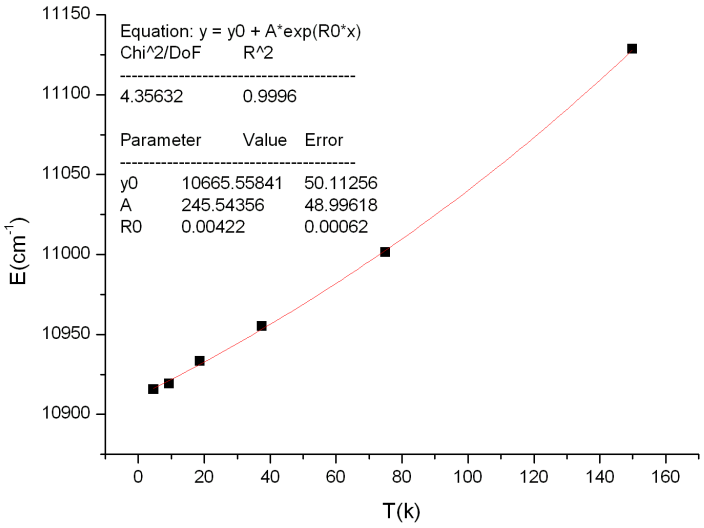

Figure 6.2 Fitting of average kinetic estimator of energy of CH_5^+ at different temperature

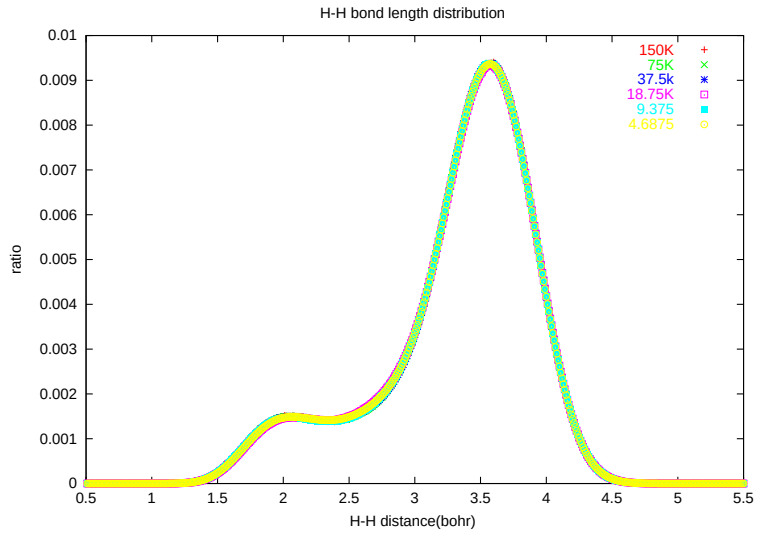

Figure 6.3 H-H Bond distribution of CH_5^+ at different temperature

4.6874K, which shows three possible distributions in Figure 6.6, 6.7 and 6.8. In these ten calculations, two of three starting from $(CDH_2)D_2^+$ finally turn to $(CD_3)H_2^+$, the other one gives the distribution as in Figure 6.8, which is a mixture of $(CD_3)H_2^+$, $(CDH_2)D_2^+$ and $(CD_2H)DH^+$. One of five starting from $(CD_2H)DH^+$ finally presents the distribution like that of $(CD_3)H_2^+$. Two of two starting from $(CD_3)H_2^+$ just keep the current distribution.

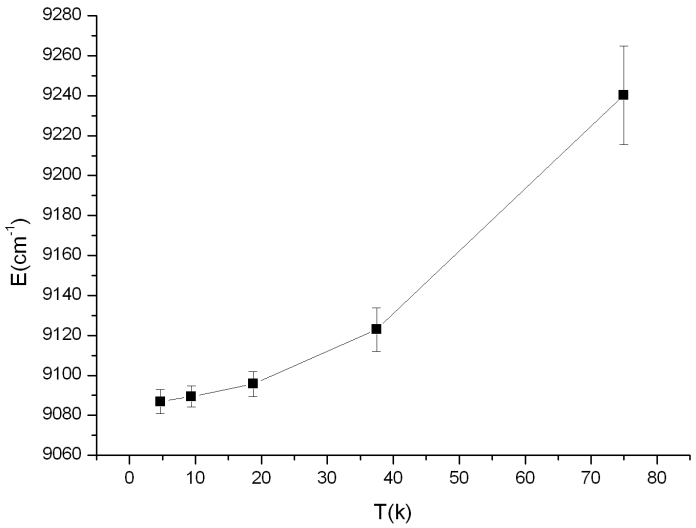

Figure 6.4 Average kinetic estimator of energy of $(CD_3)H_2^+$ at different temperature

3) Bond Distribution at relatively high temperature 75K

At this temperature, the hydrogen scrambling can be easily reached due to the thermal activation. In this case, 50 trajectories are done with different parameters, which designate when you will start to update the bond length distribution. It seems that if this parameter is similar to that for calculation at 4K, the distributions are like combination of three possible cases shown in Figure 6.8 due to easy accessibility to those configurations. Therefore, I increase the parameter to

start to update the distribution at fairly long propagation times, then the final distribution are similar to Figure 6.6, 6.7.

The number of distribution types at the begining of the calculation after random selection,denoted as *initial*, and at the end using the collections after the updating cycles, denoted as *final* are shown in Table 6.2. We can see that $(CD_3)H_2^+$ is the favorable configuration, while $(CDH_2)D_2^+$ seems not to appear again, which means the deuteurium hydrogen does not intend to be in the H_2 part. There are still a large amount of calculation staying at $(CD_2H)DH^+$ configuration. One possible assumption can be stated that if the progagation continues infinitely, the $(CHD_2)H_2^+$ should be the final configuration.

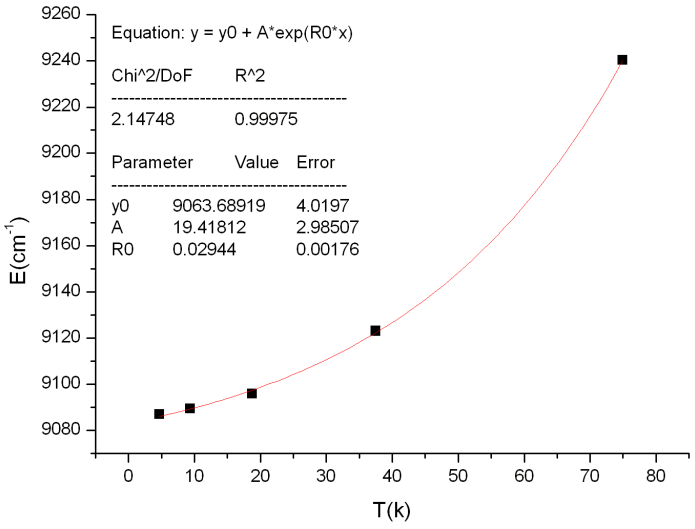

Figure 6.5 Fitting of average kinetic estimator of energy of $(CD_3)H_2^+$ at different temperature

Table 6.2 Number of distribution type at the begining and the end of the calculations

T(k)	$(CD_3)H_2^+$	$(CDH_2)D_2^+$	$(CD_2H)DH^+$	mixture
4k(initial)	2	3	5	0
4k(final)	5	0	4	1
75k(initial)	1	4	5	0
75k(final)	4	0	4	2

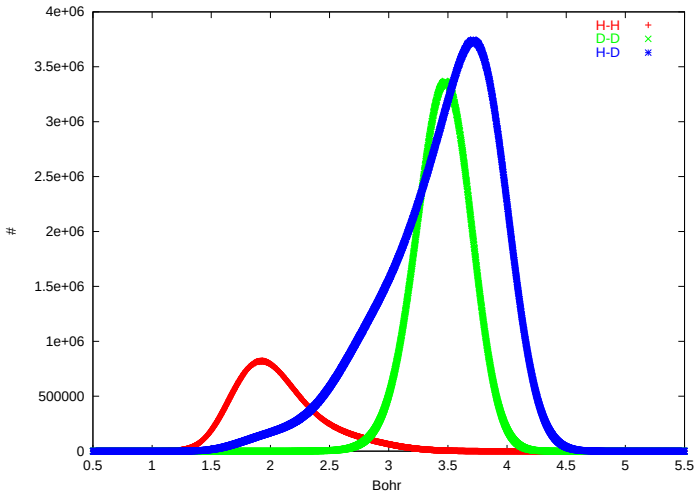

Figure 6.6 Bond Length Distribution of $(CD_3)H_2^+$

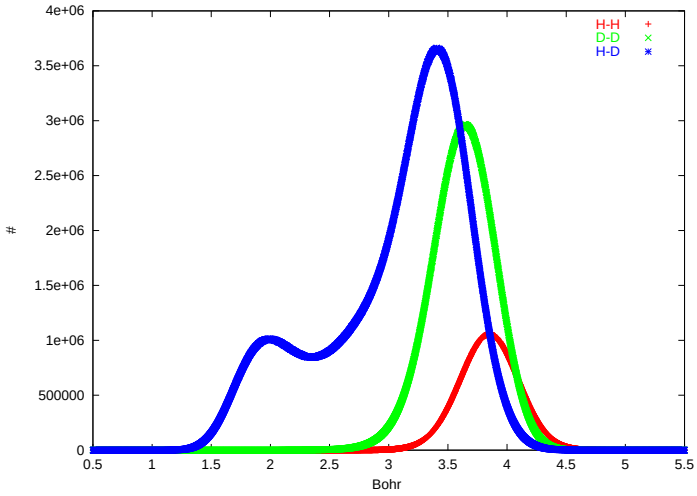

Figure 6.7 Bond Length Distribution of $(CD_2H)DH^+$

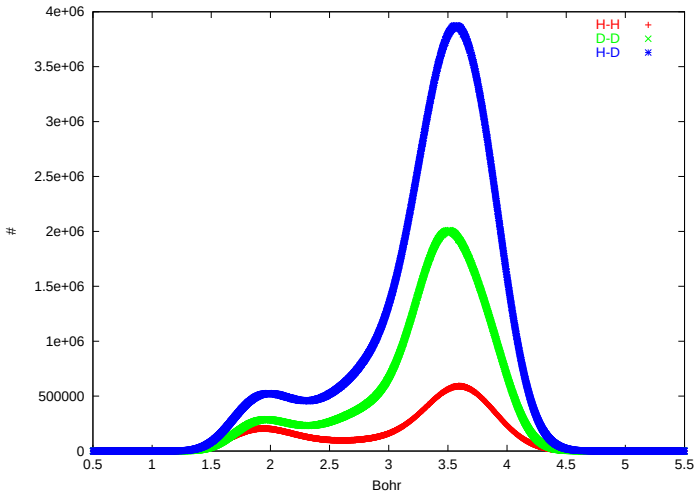

Figure 6.8 Bond Length Distribution of mixture of $(CD_3)H_2^+$, $(CDH_2)D_2^+$ and $(CD_2H)DH^+$

6.3 Conclusion

The path integral Monte Carlo method has been used to calculate the hydrogen scrambling in $(CD_3)H_2^+$, which shows that $(CDH_2)D_2^+$ is unfavorable , while the hydrogen prefers to stay in the H_2 part. Zero point energy can also be extracted from this calculation, which shows excellent accuracy as Diffusion Monte Carlo calculation.

Chapter 7

Dynamics Calculation of the HO_2+NO Association Reaction

7.1 Introduction

The reaction

$$HO_2 + NO \rightarrow OH + NO_2 \tag{7.1}$$

plays an important role in catalytic cycles to produce ozone in the upper and lower atmospheres [60]- [67]. Howard and Evenson [62] carried out the first direct measurement of the rate constant of reaction 7.1 using laser magnetic resonance to detect HO_2, OH and NO_2 species at 296K and a pressure of 140-220 Pa (1.1-1.7 Torr). Subsequently, Howard [63] extended the temperature range from 232 to 403 K and reported a small negative temperature dependence of the rate constant. Imamura *et al* [64] determined the rate constant at 299±2 K by time-resolved photoionization mass spectrometry. Seeley *et al* [65] measured the rate constant between 206 and

295 K using the turbulent flow technique and also found the reaction to be independent of the pressure between 70 and 190 Torr of N_2. Bohn *et al* [66] increased the pressure of N_2 up to 100 kpa covering the entire tropospheric pressure range at room temperature and also reported no pressure dependence of rate constant. Suggested by previous work, Bardwell *et al* [67] extended the temperature range over 183 and 300K and the pressure range from 75 to 220 Torr. The rate constants were fitted to a Arrhenius form as $3.98^{+0.29}_{-0.27}10^{-12} \times exp[(223 \pm 16.5)/T]cm^3molecule^{-1}s^{-1}$, getting good agreement with previous reports of the rate constant, and they also stated the rate constant is invariant with pressure. Thus most experiments reach the conclusions of absence of a pressure dependency and perhaps a slight negative temperature dependency, which indicates that the reaction 7.1 proceeds through a short-lived energized transient complex, which was suggested to be HOONO [63].

At high-pressure the reaction intermediates $HONO_2$ and in principle HOONO can be formed by a stabilizing collision with a third body,

$$HO_2 + NO + M \rightarrow HOONO + M \tag{7.2}$$

$$HO_2 + NO + M \rightarrow HONO_2 + M \tag{7.3}$$

The more stable product $HONO_2$ was detected in experiments reported by Butkovskava *et al* [68]- [69].

Extensive modeling of reactions 7.1-7.3 has been reported. Sumathi *et al.*[47] performed an *ab initio* study of the reaction, locating various stationary points including HOONO, and presented the possible pathway to OH+NO_2 and $HONO_2$ formation. Zhu *et al.*[46] characterized many minima and saddle points relevant to these reactions as well as the reverse reaction OH+NO_2 using sophisticated ab initio methodology.

They performed Variational Transition State Theory/RRKM calculations also considering the multi-well coupling to obtain rate constants for reactions 7.1, 7.2 and 7.3 and analogous ones for the reverse reaction. Zhang *et al.* [70] modeled the mechanism and kinetics of HO_2+NO using the multiple-well master equation using a model potential energy surface.

In previous chapter, We presented a realistic global potential energy (PES) for the OH+NO_2 reaction, and dynamics calculations were performed on that PES with a focus on the association products HOONO and $HONO_2$. Now we updated the PES with more stationary points shown below and better description of HO_2+NO channel. The new global PES that does describe the HO_2+NO channel realistically as well as all the intermediates and the OH+NO_2 channel. We perform quasi-classical trajectory calculations for the HO_2+NO reactions using this new PES.

In the section 7.2 we describe updates of the new PES and give some relevant properties of it. In Section 7.3 we present the details and results of QCT calculations using this PES. These include association cross-sections to form OH+NO_2, HOONO, and $HONO_2$, lifetime information of HOONO, and the rate constants of $HONO_2$ and HOONO complex in the high-pressure limit as well as rate constant of OH+NO_2 product in the low-pressure limit. A summary and conclusion are given in Section 7.4.

7.2 Update on the OH+NO_2 PES

Here we provide a updated new PES with an improved description of the HO_2+NO channel, which permits a study of that reaction. The only difference between this PES and the old PES for the study of OH+NO_2 reaction is with more data in asymptotic HO_2+NO and complex regions. For example, we added more data in the saddle

point regions from HOONO isomers to $HONO_2$.The PES is fitted to 66 919 energies calculated at the level of Density Functional Theory-B3LYP/6-311G(d,p). The RMS fitting error is 0.62 kcal/mol for energies up to 63 kcal/mol, relative to the global minimum.

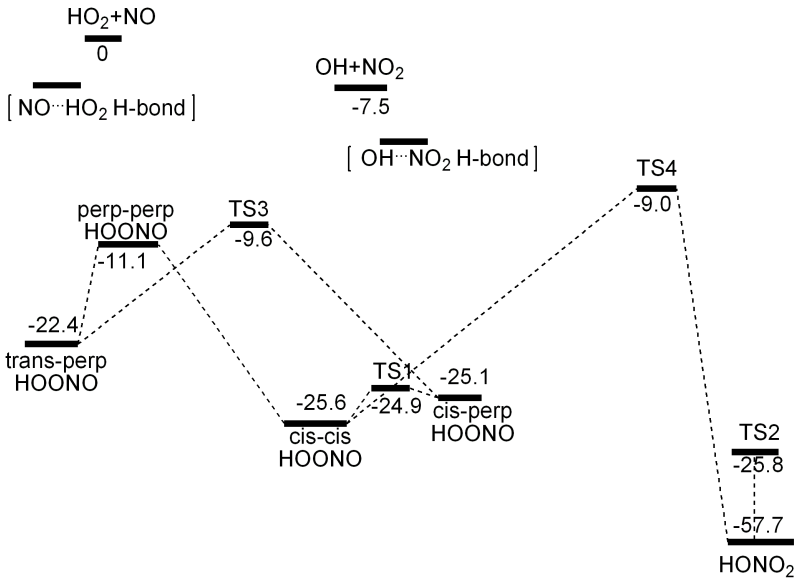

Figure 7.1 Energies (kcal/mol) of indicated minima and transition-state saddle points of the potential energy surface. The energies of the fragments are also given and the H-bond complexes associated with the fragments are indicated schematically.

The energies of the numerous stationary points are shown in Figure 7.1. For clarity only minima and saddle points of complexes are connected by dashed lines. From elementary considerations the expectation is that the HO_2+NO reactants form HOONO isomers via simple addition and that formation of nitric acid occurs from isomerization of HOONO. Hydrogen bonding in HO_2 + NO is certainly expected as such bonding has been reported for other reactions involving HO_2, such as HO_2 + H_2O [71]. Indeed two H-bonded complexes have been found on the PES and these are indicated schematically in the figure. H-bond complexes also exist for OH+NO_2 and these are also indicated in the figure. These complexes were reported previously [44], and also discussed in detail in section 5.3. In the OH+NO_2 reaction, those complexes were shown to be important in steering the reactants to either HOONO or $HONO_2$ and so

we made a major effort to verify the accuracy of the PES by doing separate CASPT2 calculations of them. For the present HO_2+NO reaction these H-bond complexes do not play such a steering role since as mentioned above and shown below HOONO is always the complex formed from these reactants and/or their associated H-bond complexes.

Table 7.1 Comparison of single point energies (kcal/mol) for the stationary points on the surface relative to the HO_2+NO minimum.

	PES	CCSD(T)/CBS[a]	B3lYP/6-311G(d,p)
HO_2+NO	0	0	0
OH+NO_2	-7.5	-7	-6.4
$HONO_2$	-57.6	-57.4	-56.6
cis-cis	-25.6	-30.6	-24.7
cis-perp	-25.2		-23.5
trans-perp	-22.3		-21.1
perp-perp	-11.1		-9.6
TS1	-24.9		-23.5
TS2	-25.8		-25.7
TS3	-9.6		-8.9
TS4	-9	-7.2	
H-bond I	-5.3		-2.6
H-bond II	-3.9		-6.5

[a] Ref. [43]

The accuracy of the PES energies is seen in Table 7.1, which contains a comparison of these energies with previous high-level calculations [43]. For reference the B3LYP/6-311G(d,p) energies are also given. Other characteristics of new PES such as the geometry and harmonic frequencies of the stationary points are quite similar to the previous PES, and detailed comparisons with previous high-level ab initio calculations showed good agreement. The current PES and the previous one smoothly and realistically interpolates between the open-shell fragments OH+NO_2 and HO_2+NO

and the complex region. This was verified by doing CASPT2 calculations along one-dimensional cuts starting from the PES optimized HOONO stationary points and separating to the fragments with all other degrees of freedom fixed. The comparisons for cuts leading to HO_2 + NO and OH + NO_2 are shown in Figure 7.2 and 7.3, respectively. As seen the PES faithfully reproduces the CASPT2 energies. It is interesting to note at the CASPT2/cc-pVTZ level of theory there is a small barrier (0.3 kcal/mol) in the cut depicting the break-up of cis-cis HOONO to HO_2+NO resulting from an avoided crossing with an excited electronic state.

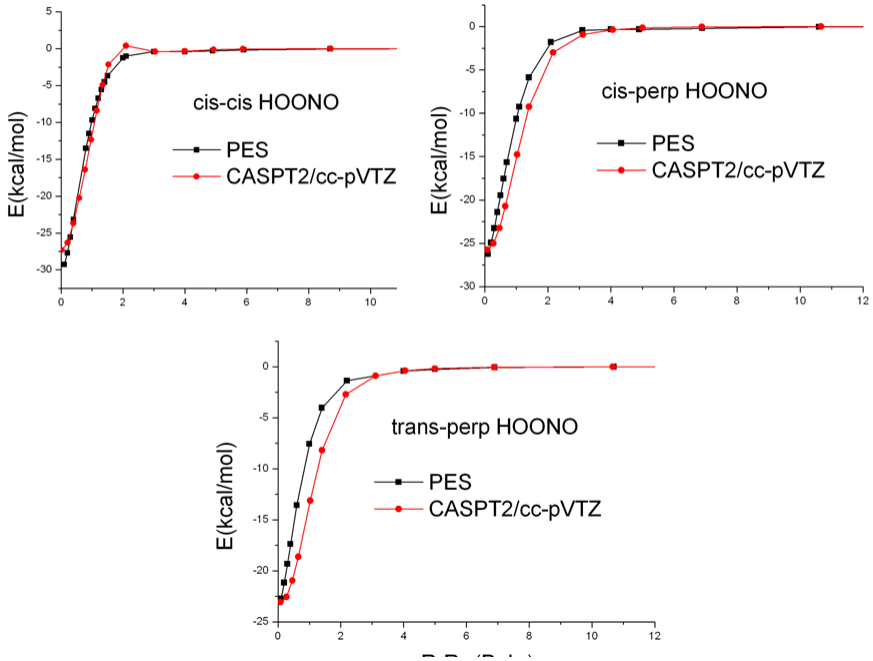

Figure 7.2 Comparison of cuts connecting indicated minima to HO_2+NO obtained directly from CASPT2/cc-pVTZ calculations and the potential energy surface.

7.3 Results and Disscussion

Standard QCT calculations using this PES were done from 0.12 to 2.4 kcal/mol initial relative collision energy to determine the cross-sections and details of the dynamics

to form HOONO, $HONO_2$ complexes and OH + NO_2 product from HO_2 + NO reactants in the ground vibrational states with rotational states sampled from a 300 K Boltzmann distribution. In brief, a normal mode analysis was done for the HO_2 and NO reactants and they were each given harmonic zero-point energy. Then random sampling was done from each normal mode in the usual fashion. Adjustments were then made to the momenta by adding thermally averaged rotation energy based as described elsewhere [2]. The trajectories were propagated with a time-step of 3 atomic units (roughly 0.07 fs) up to 14ps (200,000 time steps) and with the Verlet method. First trajectories were performed to determine the maximum impact parameter to within 0.1 Bohr. As described in detail below the formation of the HOONO intermediate is the key process for formation of both $HONO_2$ and products OH+NO_2. We found no trajectories in the collision energy considered that make these products without first forming HOONO and so the relevant b_{max} is the one for formation of

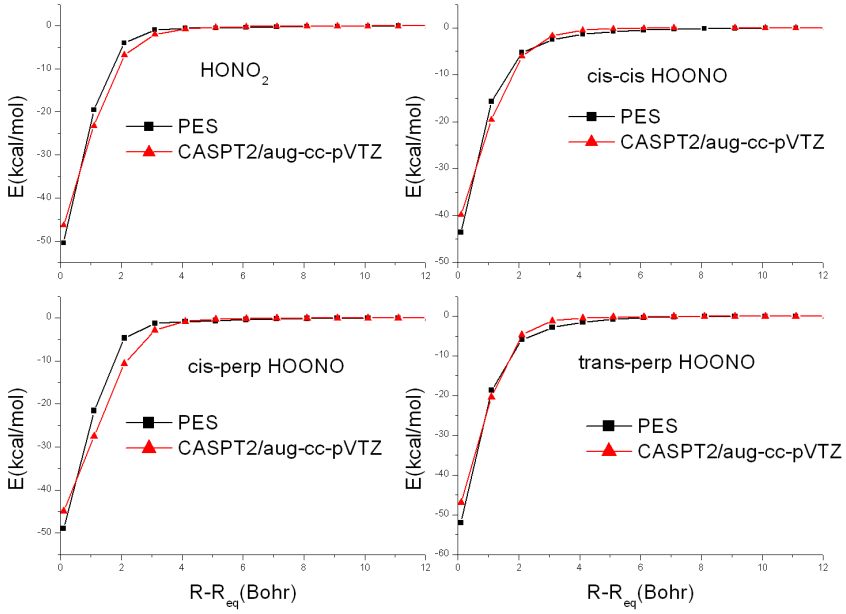

Figure 7.3 Comparison of cuts connecting indicated minima to OH+NO_2 obtained directly from CASPT2/aug-cc-pVTZ calculations and the potential energy surface.

HOONO. At each collision energy a total of 10 000 trajectories were run by the usual random sampling [2] of b from 0 to b_{max}.

For each trajectory the time dependence of the distance between the centers of mass of HO_2 and NO, denoted R(t), is used to monitor complex formation. At least one oscillation in R(t) must occur to characterize a trajectory as complex forming. Typically many such oscillations occur and then inspection of the geometry of the complex allows us to identify it. Of course more than one complex can form along a trajectory and so the characterization of complexes occurs throughout the course of a trajectory. This can in principle lead to a possibly complicated time history if there is rapid isomerization among complexes. This does occur but only for the isomers of HOONO.

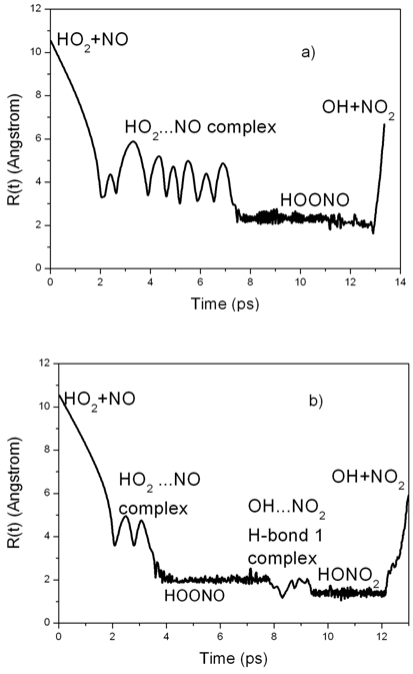

Figure 7.4 Time evolution of the distance between the OH and NO_2 centers of mass for a trajectory a) OH+NO_2 b) $HONO_2$ isomerization that illustrate typical pathway to decay to OH + NO_2 and $HONO_2$ formation.

Figure 7.4 shows R(t) for two trajectories. In both H-bond complexes initially form and go on to form HOONO which in the vast majority of cases goes on to directly form OH+NO_2, as indicated in Panel a). Panel b) shows a rare trajectory that forms $HONO_2$ via isomerization of HOONO and which subsequently leads to the products OH+NO_2. We did not find any trajectories that lead to OH + NO_2 without first forming HOONO. We also find no trajectories leading directly to $HONO_2$. We see facile isomerization among the HOONO isomers but very little isomerization between $HONO_2$ and HOONO. Animation of the trajectories shows that the HOONO/$HONO_2$ isomerization is accomplished by a mechanism where HOONO begins to dissociate to OH + NO_2 but undergoes a change in relative velocity while the incipient OH rotates bringing the incipient fragments return to the stable $HONO_2$ complex.

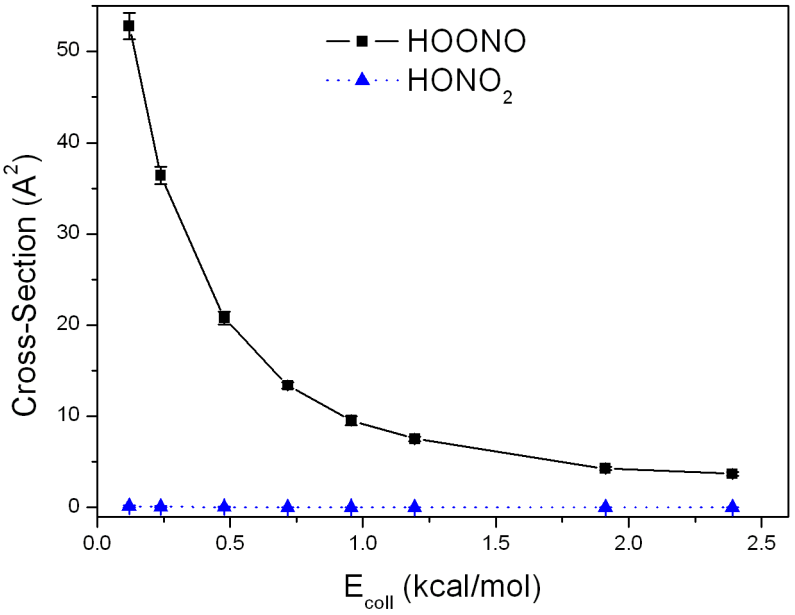

Figure 7.5 Association cross-section for HOONO (all isomers) and $HONO_2$ as a function of the initial relative collision energy for the HO+NO_2 reaction.

The energy dependence of the total cross-sections to form HOONO, $HONO_2$ complexes is plotted in Figure 7.5. As seen the cross-section to form $HONO_2$ is very small and within the uncertainties essentially independent collision energies. This small cross-section is just the result of the low probability of isomerization between HOONO and $HONO_2$, already noted. The HOONO cross-section exhibits a typical E_{coll}^{-q} (q > 0) energy dependence.

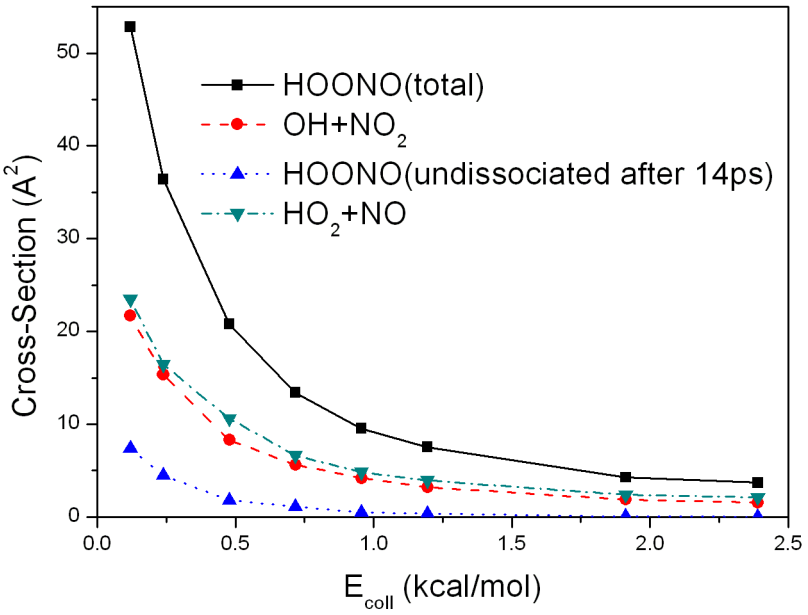

Figure 7.6 Collision energy dependence of the total cross-section to form HOONO (up to 14 ps) and its reactive (OH+NO_2) and non-reactive(HO_2+NO) component cross-sections as defined in the text.

As noted already all products of these reactions originate from the HOONO complexes. Thus the total cross-section to form HOONO complex, shown in Figure 7.5, can be decomposed into cross-section to form OH+NO_2, HO_2+NO and undissociated HOONO up to 14 ps. These are shown in Figure 7.6. As seen the cross-sections for the HOONO complex to decay into OH+NO_2 and HO_2+NO are comparable and except at the lowest collision energies the sum of those cross-sections is very close to

the HOONO cross-section. At lower energies the fraction of undissociated HOONO (after 14 ps) is relatively large, as expected and so the cross-section for undissociated HOONO is largest at the lowest collision energy and rapidly drops to zero at roughly E_{coll} of 1.0 kcal/mol.

The cross-sections shown in Figure 7.6 were used to obtain estimates of the high-pressure limit rate constants for complex HOONO, $HONO_2$, and the rate constant for product OH + NO_2, in principle in the low-pressure limit. The rate constants were obtained as usual from the expression 5.3. We compare our results with various experimental results shown in table 7.2. Note the results in that table include the factor $1/Q_{elec}(T)$, where $Q_{elec}(T)$ is the electronic partition function. This partition function is exactly analogous to the one discussed in detail previously for the HO_2 + OH reaction [72] and is given for the present reaction explicitly by 2[2+2exp(-171/T)] where the exponential factor comes from consideration of the difference in energy of the two spin-orbit stats of NO [73]. As seen there is very good agreement with experiment for the OH + NO_2 reaction. As noted in the Introduction very little, if any, pressure dependence has been observed for this reaction and while we have not directly addressed this here, the observation is certainly consistent with the present finding of a relatively short-lived HOONO complex, which as noted is the precursor to the OH + NO_2 products. Also our estimate of the high-pressure limit for formation of nitric acid agrees well with the one reported measurement, probably fortuitously so given the small number of trajectories that lead to $HONO_2$. The high-pressure limit rate constant for HOONO is, as expected, much larger than for nitric acid; however, the lifetime is much shorter and so it is not clear what pressure would actually correspond the high pressure without further modeling.

Table 7.2 For HO_2+NO reaction, high-pressure limit rate constants of complex HOONO and $HONO_2$, and low-pressure limit rate constants of product OH+NO_2 compared with previous results at 300 K.

	OH+NO_2	$HONO_2$	HOONO
calculated[a]	5.5	0.014	14.0
Ref. [63]	7.9±1.0		
Ref. [64]	6.5±2.0		
Ref. [65]	8.0±0.5		
Ref. [66]	9.6±1.5		
Ref. [68]		0.0160.005	

[a] Equation 5.3 multiplied by the factor $1/Q_{elec}(T)$ described in the text

7.4 Summary

We reported a DFT B3LYP/6-311G(d,p)-based global potential energy surface in full dimensionality for HO_2 + NO reaction, which describes $HONO_2$, HOONO, OH + NO_2 and HO_2 + NO regions. The PES is invariant with respect to permutation of like nuclei, which is essential for a realistic description of the dynamics of this system. Quasiclassical trajectory calculations were done to describe the reaction of HO_2 and NO in their ground vibrational states with rotations sampled from a 300 K distribution from 0.12 to 2.4 kcal/mol. The total cross-section for formation of HOONO (all isomers), $HONO_2$ and OH+NO_2 were presented. HOONO was shown to be the key intermediate to further decay to OH + NO_2, with nearly equal rate to decay back to HO_2+NO. After 14 ps, basically all HOONO dissociates at high collision energy. Very little isomerization to $HONO_2$ is observed resulting in a low yield of $HONO_2$, consistent with experimental observation. Association rate constants in the high-pressure limit for HOONO and $HONO_2$ complex formation, and rate constant for product HO_2+NO in the low-pressure limit were calculated based on the energy dependence of the cross-section, and both agree very well with experimental results.

Chapter 8

A New Potential Energy Surface for CH_3HCO

8.1 Motivation

In order to explore the photodissociation of CH_3HCO, we have constructed two potential energy surfaces, denoted as fifth order and sixth order PES. Those two PESs have been used to perform roaming dynamics calculations on CH_3HCO . We have shown that those two PES describes the open shell complex region like $CH_3 \cdots HCO$ quite realistic by interpolating through those problematic regions using fragmented energies. Comparison of PES against MRCI fixed one dimensional cuts illustrate similar curves. However, as shown in Figure 8.1, the MRCI curves quickly approach fragment region at around 6 or 7 Bohr, while PES curves are gradually up to 14 Bohr to enter CH_3+HCO fragment region, showing different complex region ranges. Furthermore, the roaming trajectories have configuration similar to $CH_3 \cdots HCO$ complex region. Therefore, a multireference method should be employed to treat those multirefrence configurations.

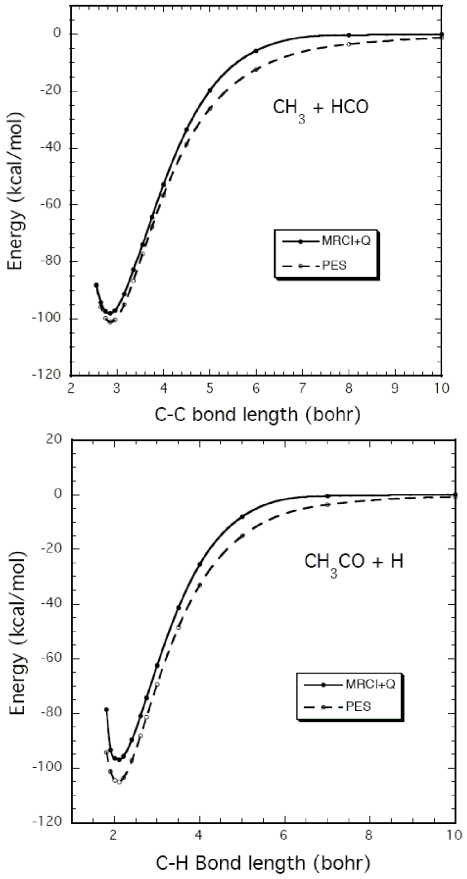

Figure 8.1 Comparison of 1D cut from PES and MRCI+Q calculations form a minimum to the separated fragments indicated on older PES.

8.2 Updates on the CH_3HCO PES

Like our previously reported two PESs, a roughly 170 000 ab initio energies are computed with CCSD(T)/AVTZ. The dataset consists of electronic energies for complex regions and fragments of all possible channels. The energy of fragment channel is obtained by separating the fragments by about 100 Bohr and assigning the energy as the sum of their fragment energies. The implementation of $CH_3 \cdots HCO$ complex region is obtained by adding MRCI energies of those multireference configrurations with possible energy shift to the whole CCSD(T)/AVTZ dataset for global fit. We choose MRCI/VTZ rather than the very time-consuming MRCI/AVTZ for single point cal-

culation. We will parallel CH_3+HCO fragment channel by shifting CH_3+HCO fragment MRCI energy. First we calculate the energy diffrence of MRCI/VTZ and CCSD(T)/AVTZ for all stationary points on acetaldehyde PES to make sure that shift on CH_3+CHO fragment will not take too much impact on other regions. The energy difference ranges from 4600-7000 cm^{-1} with mean value of 5570±178 cm^{-1}, in particular for CH_3+HCO, MRCI/VZT is higher than CCSD(T)/AVTZ by 4670 cm^{-1}. Second, In order to evaluate the possible shift value, many CH_3+HCO fragment configurations from previous trajectories are employed to calculate energy diffrence averaged at 4747 cm^{-1}. Therefore, MRCI energies of mutireference region are shifted to CCSD(T)/AVTZ by subtracting 4747 cm^{-1}, to be consistent with CH_3+HCO fragment region CCSD(T)/AVTZ energy value. Third, Basically there are two ways to obtain the $CH_3 \cdots HCO$ complex configurations. Many $CH_3 \cdots HCO$ complex configurations are selected from trajectories from previous PES with carbon-carbon bond distance from 4 to 9 Bohr. We choose some configraions of acetaldehyde from trajectories, and strectch out the carbon-carbon bond to get a series of configurations. For $CH_3CO \cdots H$ complex configuration, we employ the same procdeure described above. Totally , roughly 27 000 ab initio energy of MRCI/VTZ of selecting multi-refrence configurations are shifted and added to total dateset for global fit. The fit uses a basis

of polynomial in morse-like variables in all the inter-nuclear distance. The fit has the imporatent property of invariant with respect to all permutatoin of like nuclei. This is a fith order fit, and nearly 200 000 configurations of the curret fit gives RMS of 1000 cm^{-1}, which describes all stationary points of complex region and fragment channel, especially adding more reliable MRCI shifted energies for importment $CH_3 \cdots HCO$ and $CH_3CO \cdots H$ multireference complex regions. Table 8.1 shows the comparision of energies of PES with benchmark and previous PESs, showing better agreement with bench mark in terms of stationary points. Figure 8.2 shows one dimentional

Table 8.1 Comparison of the fitted potential energy surfaces and ab initio benchmark electronic energy calculations(without ZPE or higher-level corrections) for selected stationay points on the CH_3CHO surface relative to acetaldhyde global minimum (kcal/mol).

	CCSD(T)/CBS+CV	G3	Fifth order PES	Sixth order PES	Current PES
acetaldhyde	0.0	0.0	0.0	0.0	0
vinyl alcohol	9.1	9.6	13.5	15.0	12.4
hydroxyethylidene	50.8	51.2	54.0	53.4	57.0
TS1	70.8	70.7	72.4	72.5	72.3
TS2	83.0	82.9	87.2	85.6	82.9
TS3	75.5	76.3	87.6	81.6	77.7
TS4	87.5	87.2	84.8	96.1	87.7
TS5	110.9	111.8	102.6	108.0	98.9
TS6	86.0	86.9	91.8	95.1	85.0
CH_4+CO	-2.0	-2.7	-2.5	-1.6	-2.0
CH_2CO+H_2	35.2	33.9	43.5	37.1	39.2
CH_3+HCO	90.8	89.4	91.0	94.0	90.8
CH_3CO+H	95.6	94.0	100.9	100.5	95.6
CH_2CHO+H	102.5	101.1	103.7	103.9	113.2
CH_3+CO+H	110.5	107.8	104.7	106.0	110.6

cuts from global miniumum of CH_3HCO and some randomly generated CH_3HCO, showing better agreement with MRCI cuts than cuts of previous PESs.

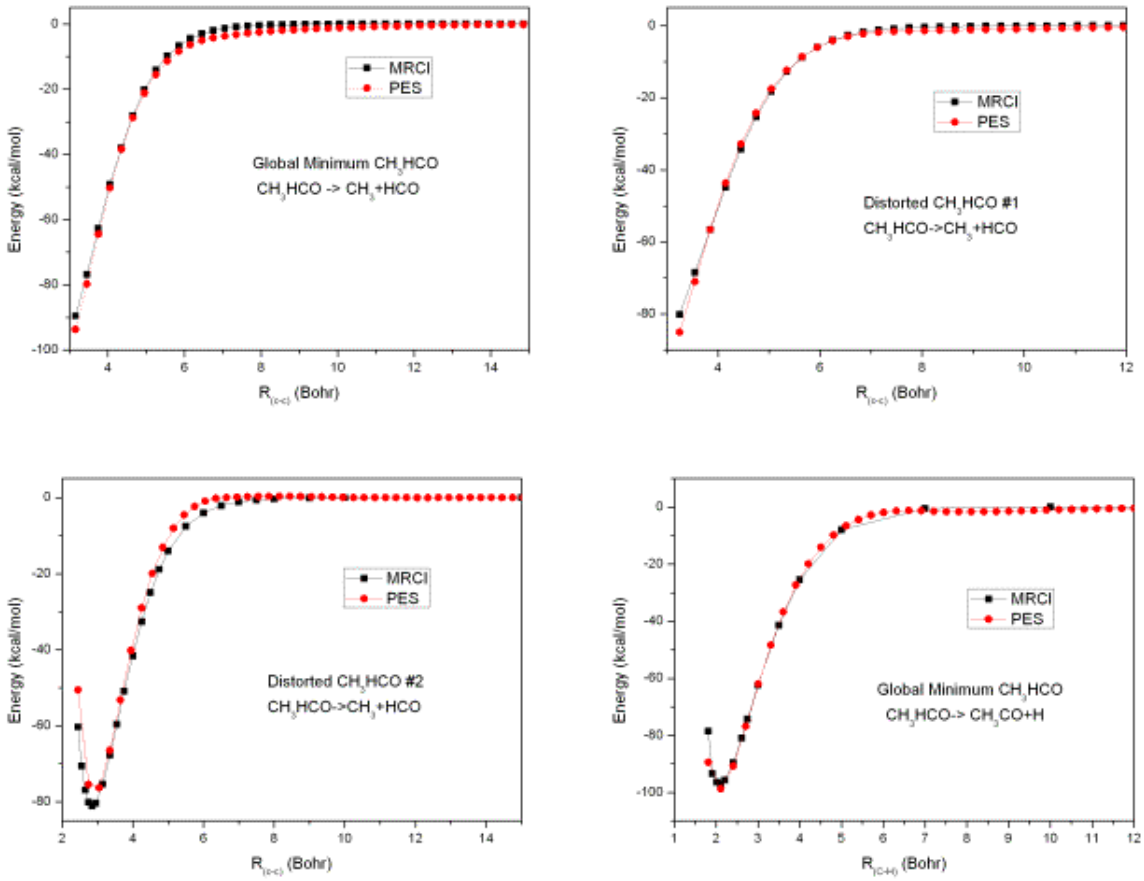

Figure 8.2 Comparison of cuts connecting indicated configurations obtained directly from MRCI/VTZ calculations and the potential energy surface.

Chapter 9

Dynamics Study of Dissociation of Allyl Radicals

9.1 Introduction

The allyl radical (C_3H_5) is very important in the combustion mechanisms of hydrocarbons, in planetary atmospheres, and in atmospheric chemistry [74]- [79]. Chen and his co-workers advanced the field by developing a pyrolysis source that could dissociate allyl iodide to produce a molecular beam of allyl radicals. Building on early spectroscopic work by Sappey and Weisshaar [80], the Chen group identified the B[1^1A_1], C[2^2B_1] and D[1^2B_2] states of allyl and some of its deuterated isotopomers using two photon ionization [81]- [83]. Subsequent work using similar techniques has characterized several Rydberg states of allyl [84], [85].

One interesting but unresolved aspect is the competition of various dissociation channels for allyl radicals excited with a specific internal energy. The reaction can

have those possible products

$$\begin{aligned} CH_2CHCH_2 &\rightarrow H + C_3H_4(Allene) \\ CH_2CHCH_2 &\rightarrow H + C_3H_4(Propyne) \\ CH_2CHCH_2 &\rightarrow H + C_3H_4(Cyclopropene) \\ CH_2CHCH_2 &\rightarrow CH_3 + C_2H_2 \end{aligned} \tag{9.1}$$

The first photodissociation study of the allyl radical was performed by Stranges *et al.* [86], who used photofragment translational spectroscopy to examine the products following excitation of allyl to the C[2^2B_1] and A[1^2A_1] states at 248 and 351 nm, respectively. At 248 nm, the primary dissociation channel was H-atom loss (84%), but CH_3 elimination (16%) was also observed. Based on the energy release, the authors proposed that the CH_3 was eliminated directly from a four-member cyclic transition state. Subsequent work [87] with similar techniques but using CH_2CDCH_2 suggested that there are actually two mechanisms for production of methyl products, each associated with a distinguishable velocity distribution. The theoretical analysis by Davis *et al.* [88] when compared to the isotopic composition of the measured products [87] suggested an identification of the two methyl elimination channels. In one, a 1,3 hydrogen shift takes place to give the CH_3CDCH intermediate, which then dissociates to yield CH_3 + DCCH, whereas in the second, two 1,2 hydrogen shifts take place, the first to form CH_2D-C-CH_2 , and the second to form CH_2D-CH-CH, which subsequently dissociates to CH_2D + HCCH. These reactions can be summarized as

$$\begin{aligned} CH_2CDCH_2 &\rightarrow CH_3CDCH \rightarrow CH_3 + CDCH \\ CH_2CDCH_2 &\rightarrow CH_2DCCH_2 \rightarrow CH_2DCHCH \rightarrow CH_2D + CHCH \end{aligned} \tag{9.2}$$

Stranges *et al.* [87] found that the kinetic energy distributions for the DCCH and HCCH were different, with the former peaking at about 15 kcal/mol and the latter peaking at about 6 kcal/mol. This result is surprising because both pathways go through an intermediate of the form (for the non-deuterated species) CH_3-CH-CH. A key assumption of the RRKM theory is that energy will be randomized in the potential energy well corresponding to this intermediate before dissociation, so that one would expect the two isotopically different products to have nearly the same kinetic energy distributions.

Other photodissociation studies have focused on the hydrogen elimination channel. The Fischer and Chen groups have excited allyl and some deuterated isotopomers near 240 nm and probed the H or D product using ps time-resolved laser fluorescence [89]-[94]. Appearance rates for the H or D products were in the 5 x 10^7 s^{-1} to $\geq$ x 10^8 s^{-1} range. The measurements suggest that H or D is produced on two time scales, but the resolution was not sufficient for measurement of the fastest appearance rate. Since the electronically excited states decay nonradiatively within 9-20 ps [92], [93], it is likely that dissociation occurs on the ground electronic state.

Finally, two groups [95]- [98] have studied the dissociation of allyl by preparing radicals whose internal energy spans the energy barriers to various dissociation channels. In one case the excited allyl was prepared by dissociation of allyl iodide at 193 nm, while in the other it was prepared by dissociation of 2-bromopropene at 193 nm. By measuring the translaional energy distribution of the iodine or bromine product, the researchers were able to determine the internal energy distribution of the allyl product. Then, by comparing this distribution with that measured for the surviving allyl products, they were able to determine the energy distribution of those allyl radicals that dissociated on the timescale between the preparation and detection. Surprisingly, some allyl radicals with energies up to 15 kcal/mol greater than

the barrier to H elimination remained stable [95], [96]. This stability was attributed to a centrifugal barrier caused by the large amount of rotational energy imparted to the allyl radical from the dissociation of the allyl iodide. Szpunar *et al.* [95] also measured the H velocity distribution using Rydberg time-of-flight methods.

Theoretical work on the allyl radical has also advanced. As previously mentioned, Davis *et al.* [88] calculated a dozen stationary points on the allyl surface at the B3-PW91/6-311G(d,p) level and provided energies and RRKM parameters. Electronic structure calculations were also reported by Deyerl *et al.* [90] to obtain vibrational parameters in order to allow accurate RRKM calculations. Most of the geometries were optimized using fourth-order perturbation theory (MP4) including single, double, and quadruple excitations and employing a 6-31G* basis set. Other locations on the surface were calculated by Stranges *et al.* [87] at the QCISD(T) level and by Calstiglione, Bach and Chen [94] at the CCSD(T) level.

In this work we reexamine the dissociation of the allyl radical using trajectory calculations on an *ab initio* potential energy surface for the ground electronic state of allyl. We provide results for dynamics study of both CH_2CHCH_2 and 2-d1-allyl CH_2CDCH_2. Our results provide branching ratios for the various hydrogen elimination products (C_3H_4 isomers +H from CH_2CHCH_2) as well as methyl elimination products (CH_3+C_2H_2 from CH_2CHCH_2). The time scale for the dissociation is found to be about 16 ps (1/e), and the results provide translational, internal energy distributions for the products. Most importantly, the trajectories suggest that the cause of the lower kinetic energy distribution for the CH_2D + HCCH products observed in the experiments of Stranges *et al.* [87] is that there is a third channel that contributes to these products, the production of methyl plus vinylidine, CH_2D + CCH_2.

9.2 C_3H_5 Potential Energy Surface Construction

The construction of the PES employs procedures described in section 2.1. The PES is made explicitly invariant under all permutations of like nuclei, and this property is expressed into the polynomial basis used for the fitting. The polynomials of Morse-type variables y_{ij} given by $y_{ij} = exp(-r_{ij}/\lambda)$, where r_{ij} is the internuclear distance between nuclei i and j, go to maximum degree of five. The associated 3308 coefficients were obtained by standard linear-least squares fitting to all the data. In terms of the data set, 97418 ab initio energies are computed at the CCSD(T)/AVTZ level. The configurations include the complex C_3H_5 regions, the separated CH_3 +C_2H_2, and the product channels for each of the C_3H_4 isomers and hydrogen. The energies of about 20,000 fragment channel data are obtained by separating the fragments by about 8 Bohr and assigning the energy as the sum of their fragment energies. The data are weighted by a simple function 0.1/(0.1+E), where E is in hartree, measured relative to the C_3H_5 global minimum. The RMS fitting error is 2.4 kcal/mol for energies up to 63 kcal/mol.

Previous *ab initio* calculations of various stationary points of the potential have been reported [87], [94], [99]. These calculations and additional ones we performed were used to check our fitted PES. Figure 9.1 shows the schematic representation of the total C_3H_5 PES. It contains a global minimum (GM), 3 local minima (LM), 9 saddle points (TS) and 4 fragment channels (CH_3 +C_2H_2, and H elimination to produce the C_3H_4 isomers allene, propyne, and cyclopropene). The hydrogen loss channels are not barrierless, but rather have saddle points connecting local minima and fragment configurations. In CH_3 +C_2H_2 channel, there exist two possible pathways to reach fragment region, denoted as 1,2 hydrogen shift and 1,3 hydrogen shift channel in Stranges *et al.* [87]. In CH_3 +C_2H_2 case, regardless of specific pathway, finally both

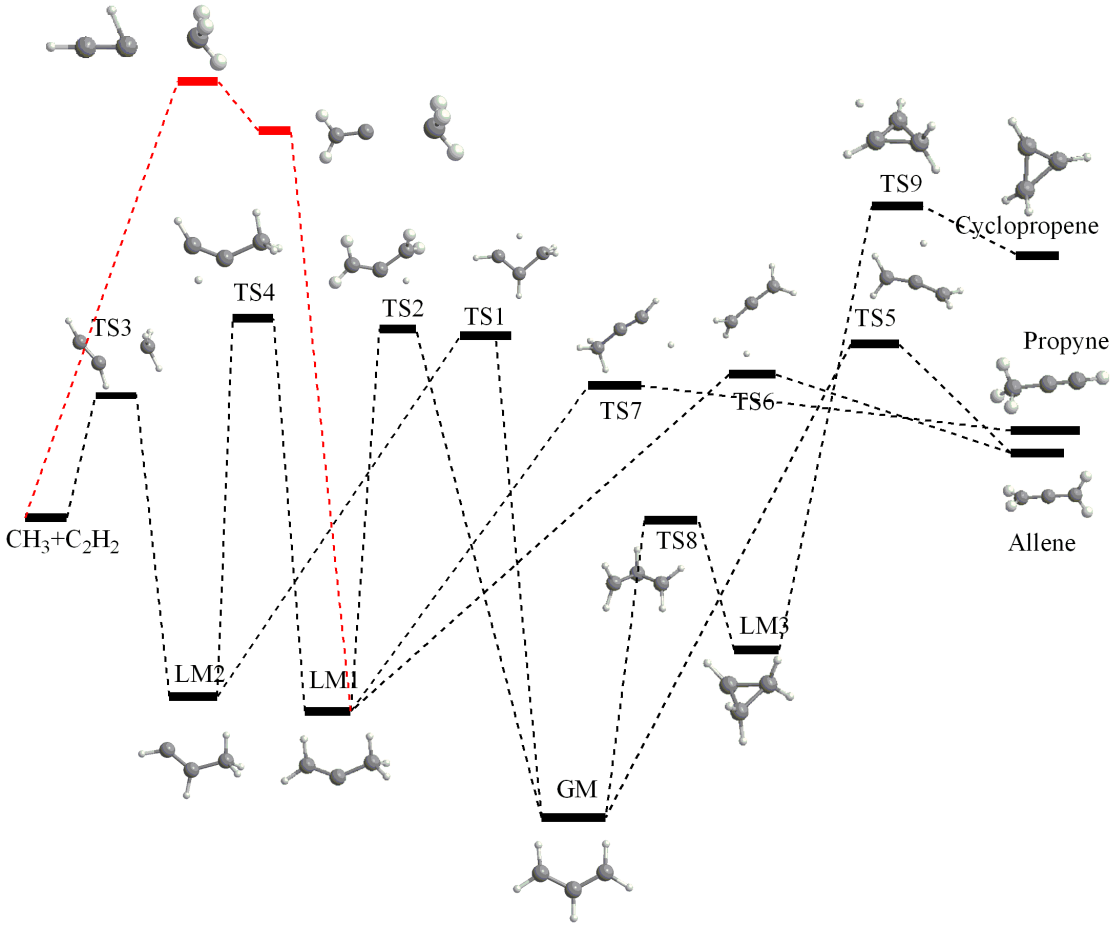

Figure 9.1 Schematic representation of the allyl potential energy surface.

mechanisms will reach the same minima LM2 (CH_3CHCH) before dissociation to CH_3 $+C_2H_2$, indicating that they are indistinguishable.

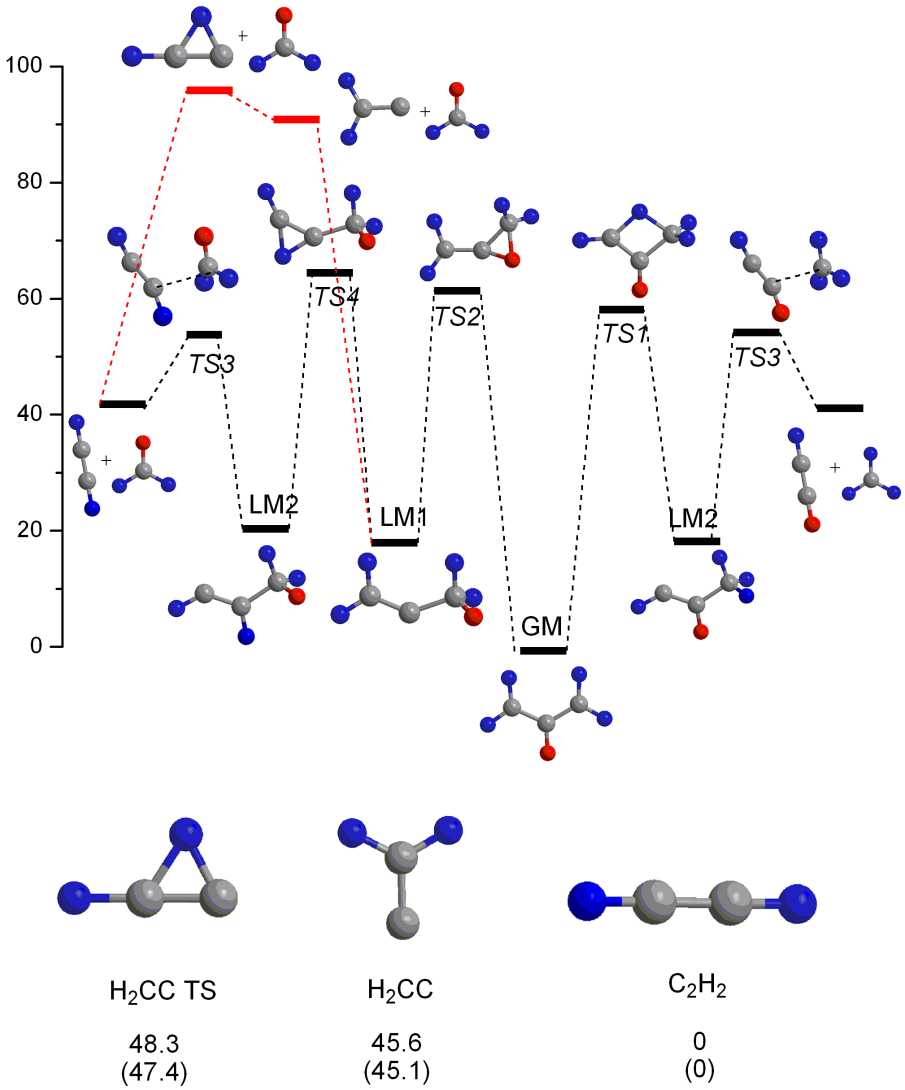

Figure 9.2 Schematic of the configurations of stationary points of the allyl potential energy relevant to the CH_3+HCCH channel. Also shown are the geometries and energies of the acetylene/vinylidene isomerization from the PES and from direct ab initio calculations in parentheses.

However, these two pathways were distinguished by different products when starting with the 2-d1-allyl CH_2CDCH_2 [87]. Of particular relevance to the CH_3 $+C_2H_2$ channel are the stationary points and product channels shown schematically in Figure 9.2, where the migrating H (D) atom is colored blue (red). The local minima and

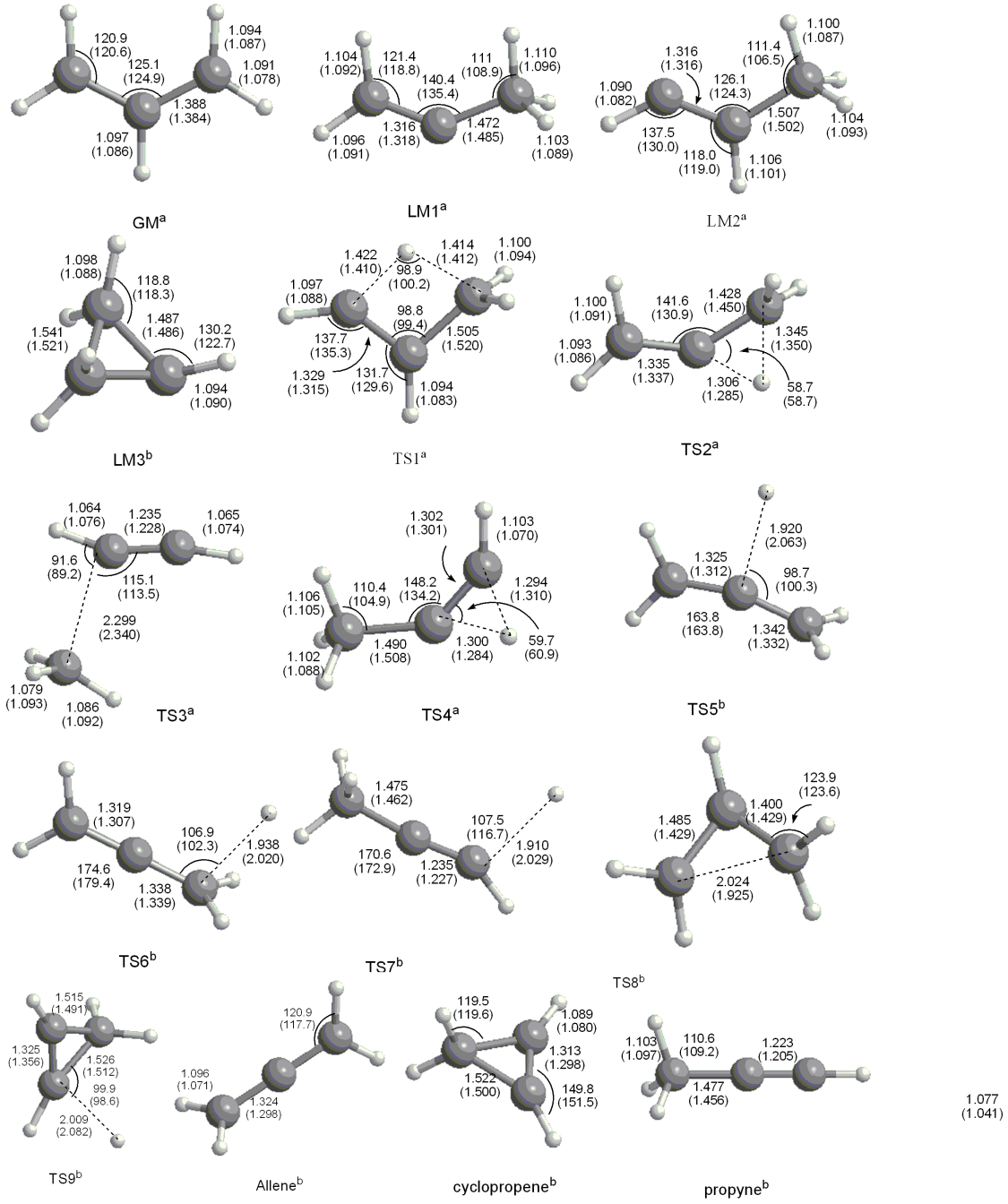

Figure 9.3 Structures of stationary points in the PES. The top values are from various benchmark calculation [a] Ref. [87]. [b] Ref. [94]. [b] Ref. [99] , and the geometrical parameters in parentheses are from PES.

transition states are indicated below as LMn and TSm where n and m are used in the figure (and as explained in the caption). We can use this notation to fully expeand the two pathways in equation 9.2 as

$$\begin{aligned} & 1,2 \quad shift \\ CH_2CDCH_2(GM) \quad & \rightarrow \quad TS2 \rightarrow LM1 \rightarrow TS4 \rightarrow LM2 \rightarrow TS3 \rightarrow CDH_2 + HCCH \\ & 1,3 \quad shift \\ CH_2CDCH_2(GM) \quad & \rightarrow \quad TS1 \rightarrow LM2 \rightarrow TS3 \rightarrow CH_3 + DCCH \end{aligned} \tag{9.3}$$

Now we can see the difference between the two pathways is whether or not the dissociation samples the potential energy well around LM1. Those that do were counted as contributing to the double 1,2 hydrogen-shift channel in Sranges *et al.* [87], whereas those that bypass this potential energy well were counted as contributing to the 1,3 hydrogen-shift channel. In 1,2 hydrogen-shift channel, the duterium hydrogen appears in methyl part; while in 1,3 hydrogen-shift channel, it appears in acetylene product.

In addition to these two channels, from the molecular dynamics on our PES we find an unusual mechanism starting from LM1 in which the CH_3CCH_2 dissociates directly to $CH_3 + CCH_2$; the highly excited vinylidene then easily isomerizes to produce internally hot acetylene via a small barrier. Interestingly, in 2-d1-allyl (CH_2CDCH_2) case, LM1 (CH_2DCCH_2) dissociates directly to $CH_2D + CCH_2$. Therefore, this unusual channel hides beneath the 1,2 hydrogen-shift channel, and it will produce the same products as 1,2 hydrogen-shift channel. We also check that the PES behaves well in the part where vinylidene isomerizes to acetylene via a known saddle point [99],

Table 9.1 Comparison of the fitted potential energy surfaces and *ab initio* benchmark electronic energy calculations for stationary points I) on the C_3H_5 surface relative to allyl global minimum (kcal/mol).

I	QCISD(T)[a]	CCSD(T)[b]	PES
Gm	0		0
Lm1	19.9		20.4
Lm2	23.3		25.0
Lm3		32.1	29.5
Ts1	67.4		69.6
Ts2	67.5	67.2	70.5
Ts3	60.8		62.5
Ts4	72.0		70.9
Ts5		66.9	69.4
Ts6		65.1	66.4
Ts7		64.3	63.5
Ts8		53.2	51.9
Ts9		86.1	86.7
C_2H_2+CH_3	52.6		52.4
Allene+H		62.4	62.9
Propyne+H		61.1	58.4
Cyclopropene+H		84.5	83.5

[a] Ref. [87]. [b] Ref. [94]

shown also in Figure 9.2 with energies and geometries. Table 9.1 gives the potential energy comparison between our PES and the ab initio results [87], [94], [99]. Table 9.2 shows the harmonic frequencies comparison and Figure 9.3 presents the geometry comparison. Overall, the stationary points in our fitted PES agree quite well with *ab initio* results in terms of geometry, potential energy and harmonic frequencies. In addition, principal moments of inertia for those stationary points on this allyl PES are presented in Table 9.3, which may be used for RRKM calculation. The PES seems quite suitable for the quasi-classical trajectory calculations described below.

Table 9.2 Comparison of harmonic frequencies (cm^{-1}) for the stationary points on the surface between the PES and direct *ab initio* calculations.

GM	GM	LM1	LM1	LM2	LM2	LM3	LM3	TS1	TS1	TS2	TS2	TS3	TS3
a	PES	a	PES	a	PES	b	PES	a	PES	a	PES	a	PES
426.1	393	186.7	93.4	202.6	40.4	524.2	562.2	-2153.2	-2155.1	-1929.4	-1733.4	-451.3	-560.3
532.3	468.9	310.5	389	404.4	481.4	754.9	792.2	445.7	298.5	298.1	267.8	50.2	101.4
550.6	562.4	473.2	455.6	606.4	533.7	766.6	833.9	621.5	587.4	405.4	401	230.8	254
779.8	813.1	867.1	900.1	793.1	626.6	849.5	946.1	681.5	626.5	687.7	515.5	437.5	510.9
802.4	853.5	892.1	950.9	798.4	723.1	927.8	1024.9	881.1	773.1	815.6	703.3	474.6	638.2
927.9	885.5	933.7	1009.3	932.6	947	1000.4	1041.6	905.4	833.2	826	810.9	522.3	656.6
1012.8	1079.3	1036.8	1087.3	1048.1	1066.4	1037.3	1081.6	936.2	840.5	965	935.4	619.7	661.1
1036.2	1094.6	1088.3	1181.2	1106.6	1221.1	1068.6	1159.5	1035.5	961.4	1011.6	1025.7	734.1	821.8
1213.8	1190.5	1367.3	1397.1	1253.5	1286.2	1073.5	1165.2	1040.6	1048.8	1090.9	1150.9	761.4	823.4
1264.5	1326.7	1393.2	1501.9	1385.7	1392.5	1140.4	1211.9	1114.2	1203.8	1125.7	1213.8	812.7	933.7
1404	1447.3	1424.2	1555.6	1452.8	1559.1	1254.6	1276.4	1218.1	1335.3	1398.8	1412.9	1379.5	1395.3
1500.2	1573.5	1440.5	1654	1453.2	1573.5	1432.1	1548.2	1399.3	1405.9	1428.6	1517.4	1387.1	1420.6
1505	1584.6	1759.9	1782.4	1695.2	1709	1457.8	1582.1	1646.1	1516.2	1677.5	1624.4	1928.8	1753.3
3135.3	3110.6	2967.1	2975.7	3014.8	2864.7	3065.9	2960.1	1836.4	1919.6	2168.2	2337.9	3087	3076.1
3137.9	3159.2	3033.6	3025.4	3024.4	2974.3	3067	2967.3	3058.4	3041.7	3046.9	2987.2	3259.1	3256
3145	3183.4	3058.5	3111.4	3078.2	3105.8	3134.1	3267.7	3129.6	3145.9	3072.6	3042.1	3270.8	3256.6
3245.6	3275.7	3085.7	3169.9	3127.3	3110	3145.4	3328.6	3157.5	3174.3	3191.9	3106.3	3390.8	3337.9
3248.1	3301.2	3160.2	3182.7	3239	3308.4	3205.8	3398.7	3186.9	3223.9	3196.3	3275	3477.5	3502.3
TS4	TS4	TS5	TS5	TS6	TS6	TS7	TS7	TS8	TS8	TS9	TS9	Allene	
a	PES	b	PES	b	PES	b	PES	b	PES	b	PES	b	PES
-2112.5	-1795	-679.8	-592.1	-440.6	-571.4	-472.4	-775	-931.8	-734.6	-533.6	-784.9	357.5	262.6
144.7	109.7	124.2	76.1	196.9	120.9	27.2	110.6	564	343.2	149.4	328.1	357.5	263.6
217.3	404.8	371.5	224.4	268.8	184.2	201.3	151.8	617.1	587.1	236.8	448.9	838.9	453.1
355.4	421.8	414.6	410.6	363.9	248.1	334.1	197.8	638.4	683	601.9	658.2	838.9	737.6
585.1	770.3	452.4	529.1	366.3	653	352.9	434.6	747.3	725.1	784.5	838.3	866.9	737.6
820.8	837.4	826.8	758.8	842.7	840.7	601.4	531.8	895.9	891.2	813.4	944.8	992.3	1166.7
902.4	905	833.3	821.8	849.5	1001.4	671.2	948.5	907.5	900.6	902.9	952	992.3	1167.7
1019.1	1076	853.1	843.8	867.4	1012	935.8	1118.9	1030.9	1055.4	1002.1	1000.7	1093.6	1331.8
1022.1	1177.9	989.1	1090.1	984.4	1057.3	1018.8	1139.5	1098.5	1090.3	1012.1	1019.9	1398.2	1596.2
1367.6	1363.3	996.9	1170.4	996.4	1212.4	1028.7	1210	1256.3	1302	1057.9	1112.1	1452.1	1628.8
1433.9	1576.1	1076.8	1241.6	1082.1	1279	1378.3	1396.2	1326.5	1308.8	1094.9	1152.7	2005.4	2063.4
1441.1	1578.3	1400.1	1568.2	1395.9	1591	1450.4	1656.2	1421.7	1494.8	1148.9	1227.5	3106.4	3291.6
1866.1	1752.1	1448	1654	1446.8	1644.6	1450.7	1681.3	1493.6	1532.8	1499.9	1600.7	3110.8	3427.6
2355	2618.8	1946.9	1895.7	1980.6	1902.8	2140.6	2026.6	3032.7	2949.7	1664.1	1692.6	3185.8	3427.7
2994.1	2815.1	3109.6	3047.5	3100.9	3112.5	3007.2	3120.7	3103.8	2984.5	3025.7	2877.6	3185.8	3430.9
3027.1	2993.2	3114.2	3217.1	3115.7	3174.9	3077	3170.7	3152.5	3172.8	3095.4	3092.8		
3082.2	3089.8	3189.7	3313.1	3176.4	3239.1	3081.1	3174.3	3176.1	3268.9	3225	3142.4		
3103.8	3193.5	3200.8	3344.6	3191.4	3258.2	3433.6	3599.8	3206	3393.7	3267.5	3402.9		
c-propene		Propyne	Propyne	C_2H_2	C_2H_2	CH_3	CH_3	H_2CC	H_2CC	H_2CC TS			
b	PES	b	PES	a	PES	a	PES	c	PES	c	PES		
582.8	556.6	327.1	267.2	699.2	699.2	463.4	687.3	327	226	936i	947i		
787.5	586	327.1	267.2	699.2	699.2	1370.7	1395.5	769	807	575	676		
823.5	896	607.3	590.2	800.3	800.3	1370.7	1395.5	1234	1294	905	969		
906.3	964.8	607.3	590.2	800.3	800.3	3100.6	3112.7	1682	1738	1821	1780		
1006.7	1015.8	935.8	977.9	2082.1	2082.1	3293.7	3112.8	3159	3220	2559	3197		
1008.6	1023.5	1026.4	1147.4	3626.4	3626.4	3293.7	3197.2	3228	3252	3377	3711		
1058.5	1042.7	1026.4	1147.4	3659.3	3659.3								
1102.2	1074.4	1379.3	1324.2										
1150	1137.5	1451.2	1704.9										
1505.9	1527.7	1451.2	1705.1										
1704.5	1797.9	2178.2	2275.2										
3023.8	3133.6	3008.2	3068.7										
3093.1	3159	3081.5	3223										
3221	3390.7	3081.5	3223.1										
3265.4	3423.8	3438.8	3790.1										

[a] Ref. [87]. [b] Ref. [94]. [c] Ref. [99]

Table 9.3 Principal moments of inertia (atomic units) for indicated stationary points on the allyl PES.

	$\mathbf{I}(10^5)$		
GM	0.603	3.169	3.771
Lm1	0.468	3.737	4.003
Lm2	0.579	3.405	3.792
Lm3	1.405	1.574	2.449
Ts1	0.844	2.638	3.255
Ts2	0.512	3.465	3.802
Ts3	0.864	4.785	5.423
Ts4	0.531	3.559	3.882
Ts5	0.5614	3.692	4.011
Ts6	0.464	3.989	4.219
Ts7	0.447	4.160	4.398
Ts8	1.090	2.188	2.931
Ts9	1.490	1.766	2.561
Allene	0.236	3.600	3.600
Propyne	0.211	3.814	3.814
Cyclopropene	1.100	1.472	2.359
CH_3	0.117	0.117	0.233
C_2H_2	0	0.930	0.930
H_2CC	0.125	0.826	0.951
H_2CC TS	0.083	0.807	0.891

9.3 Trajecotry Setup and Analysis Method

The quasi-classical trjaectory calculations were performed using methods similar to those used previously [100]. Calculations were done in a space-fixed frame using microcanonical sampling of initial momenta subject to the zero total angular momentum constraint. The integration was done using time steps of 0.1205 fs and were run for typically 200,000 steps or 24.1 ps (in some cases 100,000 steps or about 12 ps).

Trajectories were analyzed by first assigning a structure to the products. A program automatically classified the final configuration into several categories, such as H + allene, H + propyne, H + other C_3H_4 products, and CH_3 + C_2H_2. Since the trajectory keeps track of the identities of the different carbons and hydrogens, it is possible to further categorize the results. Thus, for the CH_3 + C_2H_2 category, the products were examined to see whether they were consistent with a 1,3 hydrogen shift mechanism or a double 1,2 hydrogen shift mechanism shown in equation 9.3. There are multiple variants for each reaction depending on which hydrogens are transferred. Once the final structure has been determined, it is a simple matter to determine the relative velocity of the two fragments in the center-of-mass frame. This velocity is used to determine the kinetic energy distribution.

9.4 Dissociation of Allyl (CH_2CHCH_2)

A general overview of the results is taken from a summary of 18627 trajectories for C_3H_5 starting from the global minimum. The trajectories were stopped when a dissociation occurred or when they had run for 24 ps. Of these trajectories, about 18% did not react, whereas 72% dissociated to give identifiable products; the other 10% gave unreasonable products or products not easily identified by our computer algorithm. Of the trajectories that did dissociate to identifiable products, 80% gave allene, 12% gave propyne, 5% gave methyl + acetylene via an apparent 1,3 hydrogen shift mechanism, 1% gave methyl + acetylene via an apparent double 1,2 hydrogen shift mechanism, and another 1% produced a C_3-containing product that was not readily identified as allene or propyne. In some cases for this last group, the structure was that of cyclopropene, whereas in others, it was simply a stretched version of allene or propyne. A exponential fit of the number of trajectories undissociated as a function of time gave a 1/e decay time for the dissociation of 16 ps for CH_2CHCH_2 .

The presence of some trajectories producing a ring structure for C_3H_4 should not be taken as evidence that substantial time during the trajectory was spent in the cyclo-C_3H_5 potential energy well. Although the entrance barriers to this potential energy well are substantially below the excitation energy of 115 kcal/mol, there is little evidence that the potential energy well is significant in the dissociations. For example, none of the 18627 CH_2CHCH_2 and only 3 of the CH_2CDCH_2 trajectories eventually eliminated the central carbon as part of a methyl product. If a substantial number of trajectories entered the cyclo-C_3H_5 potential energy well, we would expect scrambling of the carbons in the final products; some methyl would have the central carbon atom. The non-importance of the cyclo-C_3H_5 potential energy well is also consistent with the experimental results on dissociation of CH_2CDCH_2 [87]. If a substantial number of trajectories spent time in this potential energy well, the deuterium would be scrambled, and there would be no way to account for the observed difference in the velocity distributions of HCCH and HCCD.

The trajectory results are in reasonably good agreement with experimental data, although there are some significant differences. The quantum yields (and branching ratios) for hydrogen and methyl elimination have previously been reported as 95% and 5% (BR=19.0) for CH_2CHCH_2 [87], whereas the trajectories gave 94% and 6% (BR=15.7) for C_2CHCH_2. The trajectory results indicate that about 88% of allene formed from CH_2CHCH_2 dissociation is produced via loss of the central hydrogen. For the methyl elimination channel, the ratio of reaction 1,3 shift to 1,2 shift meachnism was found experimentally to be about 1:1, whereas the trajectory results give 5.6:1 for CH_2CHCH_2. If acetylene produced via the vinylidine channel were more easily ionized than acetylene because of greater internal excitation, the experiment would underestimate this ratio.

The one experimental area where it is not easy to reconcile the trajectory results with experiment concerns the dissociation timescale. The trajectories give a 1/e time of 16 ps and a dissociation rate of 6.3 x $10^{10}s^{-1}$ for CH_2CHCH_2 and 23 ps and 4.4 x $10^{10}s^{-1}$ for CH_2CDCH_2 . In contrast Deyerl *et al.* [89], [89] measure and calculate a rate on the order of 4.8 x $10^{8}s^{-1}$ and see changes in the H vs. D ratio for dissociation of 2-deuteroallyl at times as long as 100 ns.

9.4.1 Hydrogen Elimination Channel

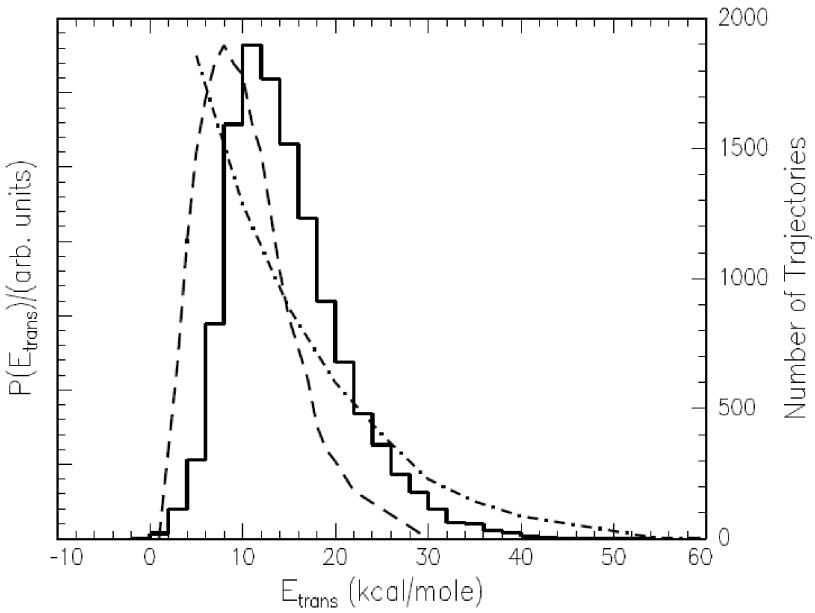

Figure 9.4 Kinetic energy distribution for hydrogen elimination from CH_2CHCH_2. Solid curve: trajectory results; dashed curve: experimental results from reference [95]; dot-dash curve: experimental results from reference [86].

Hydrogen loss is the main exit channel for allyl dissociation. Figure 9.4 shows the kinetic energy distribution for the hydrogen elimination channels derived from the trajectory results for CH_2CHCH_2 along with distributions obtained from previous experiments. Since the trajectories start with zero angular momentum, the comparison between experiment and theory should be made with caution. Szpunar *et*

al [95], [96] have argued that the rotational angular momentum of the allyl radical generated in the dissociation of allyl iodide is responsible for the observation that hydrogen elimination occurs only significantly above the energetic barrier. The rotational temperature in the experiments by Stranges *et al.* [86] is also likely to be about 50K due to the use of a heated pyrolysis source. It seems plausible that the rotational distribution of the allyl precursor could affect the experimentally measured translational energy distributions. Nonetheless, it is clear that, except perhaps at the lowest energies, the trajectory results are in reasonable agreement with the experimental observations.

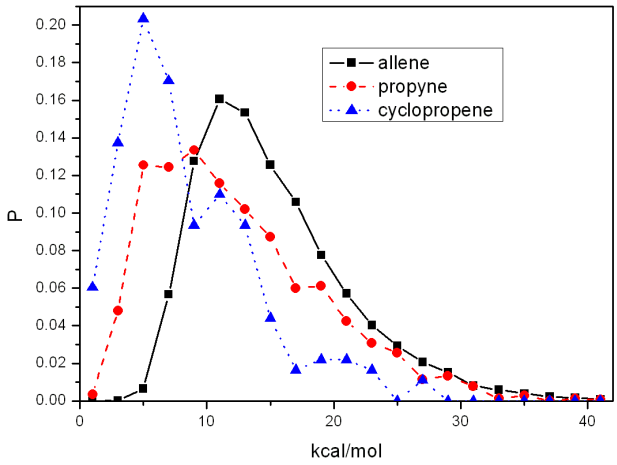

Figure 9.5 Kinetic energy distribution for Allene, Propyne and Cyclopropene+H from CH_2CHCH_2.

The kinetic energy distributions for the various hydrogen elimination channels from the C_2CHCH_2 trajectories are shown in Figure 9.5. We can say that the distributions of those hydrogen elimination channels are similar , with the H + propyne and H + other C_3H_4 channels peaking at somewhat lower energy (6-9 kcal/mol) than the distribution for H + allene. Keep in mind that most of the C_3H_4 isomers are in allene

form, while other isomers do not contribute too much to the total distribution in Figure 9.4.

9.4.2 Methyl Elimination Channel

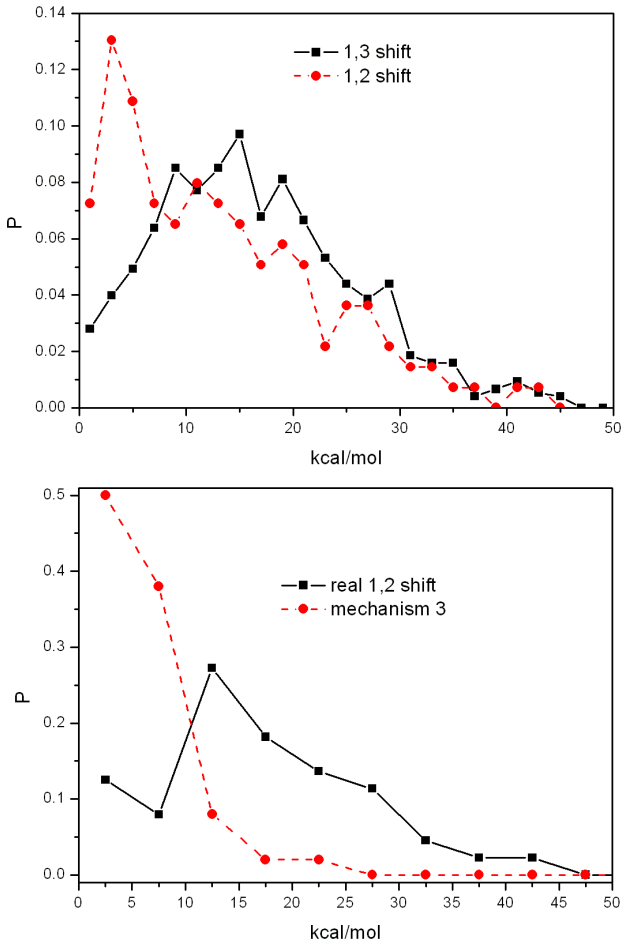

Figure 9.6 Top panel: kinetic energy distribution for original 1,2 and 1,3 shift from CH_2CHCH_2. Bottom panel: kinetic energy distribution for real 1,2 shift and mechanism 3 part of orignal 1,2 distribution.

Methyl elimination channels were identified by examining the final products to see whether they were consistent with a 1,3 hydrogen shift mechanism or a double 1,2 hydrogen shift mechanism. The top panel of Figure 9.6 shows that the distribution for

the dissociation of C_3H_5 via 1,3 hydrogen shift mechanism peaks at a higher kinetic energy (about 14 kcal/mol) than does the distribution for dissociation via 1,2 hydrogen shift mechanism. The distributions illustrate that 1,2 and 1,3 hydrogen show totally different translatioanl energy distribution. As noted before, this is particularly surprising, since the presumed pathways for 1,3 and 1,2 hydrogen shift mechanisms both traverse LM2 before dissociation. The RRKM theory would predict that energy would be randomized in the LM2 potential energy well before dissociation, so that the kinetic energy distributions for the products from these two mechanisms should be nearly identical. The reason for the difference will become clear below.

In order to investigate the methyl elimination channels in more detail, we ran trajectories for CH_2CHCH_2 starting either from LM1 or LM2. For all the trajectories that produced methyl, we determined the kinetic energy distribution in each case. The distributions obtained starting in these local minima are similar to those found for the two mechanisms from trajectories starting at the global minimum.

The surprising result, which explains the paradox of why the two kinetic energy distributions are not identical, came from close examination of the trajectories starting from LM1. Those producing methyl were of two kinds, the ones that did the second 1,2 hydrogen shift and those that dissociated directly to vinylidine as below, denoted as mechanism 3:

$$CH_3CCH_2 \rightarrow CH_3 + CCH_2 \quad mechanism \quad 3 \tag{9.4}$$

In more than one half of the trajectories starting from LM1 (CH_3CCH_2), the C-C bond broke well before a hydrogen from the CH group migrated to the center carbon. Although the trajectories typically stopped soon after the C-C bond was broken, the CCH_2 clearly had sufficient energy to rearrange to HCCH. On the other hand, the acetylene produced from vinylidine was created with a very large degree

of vibrational energy, leaving much less energy available as kinetic energy of recoil. The kinetic energy distribution for the products of a configuration consistent with 1,2 shift mechanism is therefore peaked at lower energy than that for products of a configuration consistent with 1,3 shift mechanism. Thus, the trajectory results strongly suggest that the distribution attributed to 1,2 shift actually consists of a mixture of trajectories consistent with 1,2 shift and those consistent with machanism 3. We actully divide the 1,2 shift mentioned above into real 1,2 shift and mechanism 3, and the translational energy distributions of these two channel are shown in bottom panel Figure 9.6. As seen, the real 1,2 shift distribution looks very similar to 1,3 shift mechansim curve in top panel of Figure 9.6, both peaked around 14 kcal/mol. It thus appears that the RRKM assumption is correct; trajectories passing through the LM2 potential energy well do produce nearly identical kinetic energy distributions, regardless of how they get to this potential energy well. While the mechanism 3 curve shows peak is around 5 kcal/mol, dropping very quickly close to 0 arond 15 kcal/mol, showing totally different behavihor compared with real 1,2 and 1,3 shift mechanisms. As seen in Figure 9.2, rather than isomerizing into LM2, LM1 (CH_3CCH_2) needs much more energy (extra 40 kcal/mol) to dissociate to vinylidine or highly excited acetylene after rearrangment. As a result, much less energy is left in the translational part for products.

Morever, the highly excited acetylene may be another evidence for this unusual mechanism 3. Therefore we repeat our analysis above for internal energy distribution of C_2H_2 shown in figure 9.7. The top panel of figure 9.7 presents those distribution of our original 1,2 and 1,3 channel. The two curves have large overlapping area, but 1,2 shift seems have more internally hot acetylene. Subsequently the bottom panel show the components of this mixed 1,2 shift. Surprisingly, the real 1,2 shift curve and mechanism 3 curve dose not have too much overlap. Most of C_2H_2 with interal energy above 70 kcal/mol are from mechanim 3 ; while real 1,2 shift curve looks close

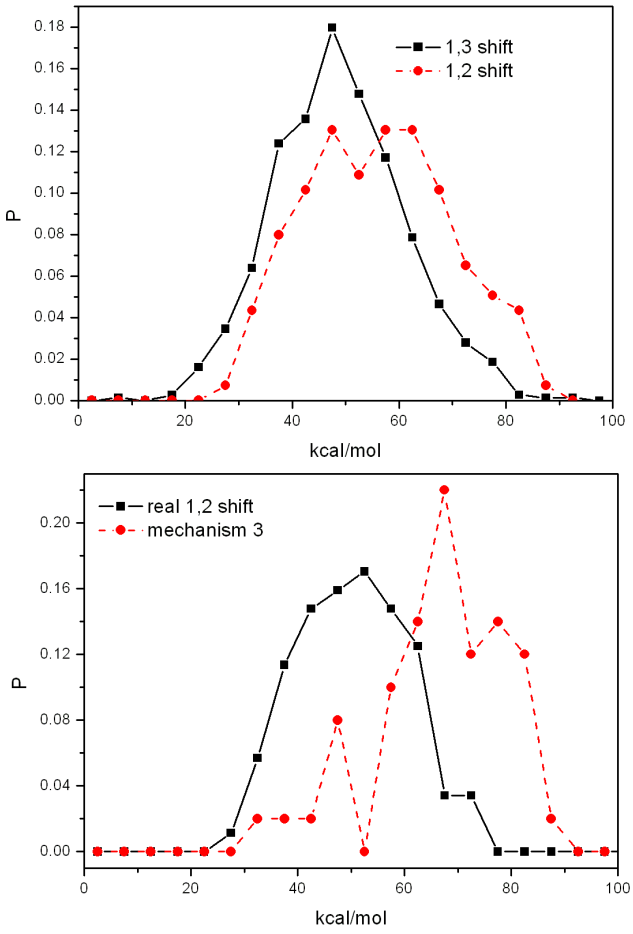

Figure 9.7 Top panel: internal energy distribution of C_2H_2 for original 1,2 and 1,3 shift from CH_2CHCH_2. Bottom panel: internal energy distribution of C_2H_2 for real 1,2 shift and mechanism 3 part of orignal 1,2 distribution.

to 1,3 shift curve in top panel of figure 9.7. All of those results are consistent with translational energy distribution results.

9.5 Dissociation of 2-d1-allyl CH_2CDCH_2

In the 2-d1-allyl CH_2CDCH_2 case, products could be very complicated. We got approximately 22000 finished trajectories dissociated to give identifiable products. Figure 9.8 illustrates various ratio of possible products. In terms of quantum yields (and branching ratios) for hydrogen and methyl elimination,the trajecotries gave 91.9% and 8.9% (BR=10.1) for CH_2CDCH_2 case, smaller than CH_2CHCH_2 case (94% and 6% (BR=15.7)). Minsek *et al.* [83] measured the ratio of allene to propyne formation by dissociating the allene isotopomer CH_2CDCH_2 and measuring the ratio of D to H. Under the assumption that most of the allene is formed by loss of the D, they estimated the allene to propyne ratio to be between 2:1 and 3:1. The trajectory results for D elimination vs H elimination for CH_2CDCH_2 gave a ratio of 2.7:1. For the methyl elimination channel, the ratio of 1,3 shift to 1,2 shift was found experimentally to be about 1.6:1, whereas the trajectory results give 6:1 for CH_2CDCH_2, similar to the CH_2CHCH_2 case. A exponential fit of the number of trajectories undissociated as a function of time gave a 1/e decay time for the dissociation of 23 ps for CH_2CDCH_2 .

9.5.1 H/D Elimination Channel

Of the trajectories that did undergoes H/D elimination, 73.5% gave D+C_3H_4, and 26.5% gave H+C_3H_3D. Figure 9.9 shows the kinetic energy distribution for D+C_3H_4 and H+C_3H_3D derived from the trajectory results. Both peak around 12 kcal/mol, but H+C_3H_3D seems to have more distribution around low kinetic energy area. This

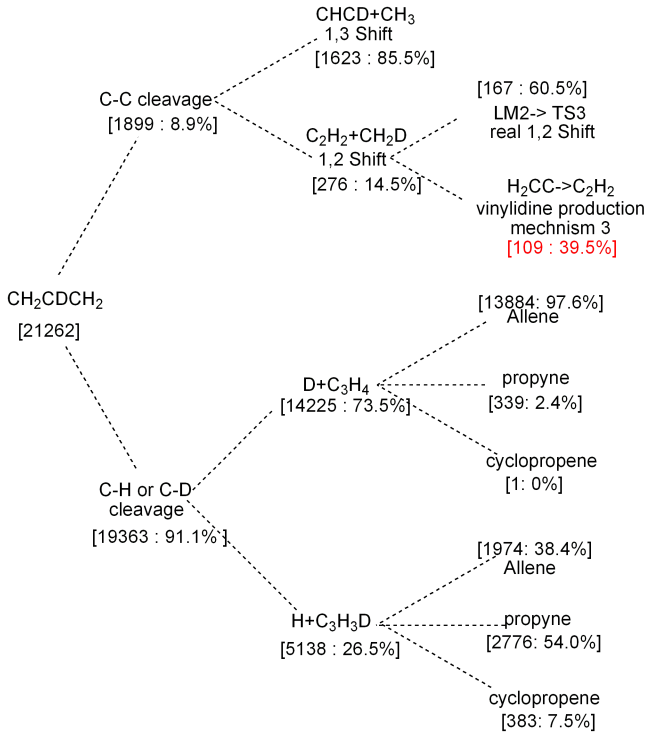

Figure 9.8 Illustration of ratio of various channels from dissociation of CH_2CDCH_2

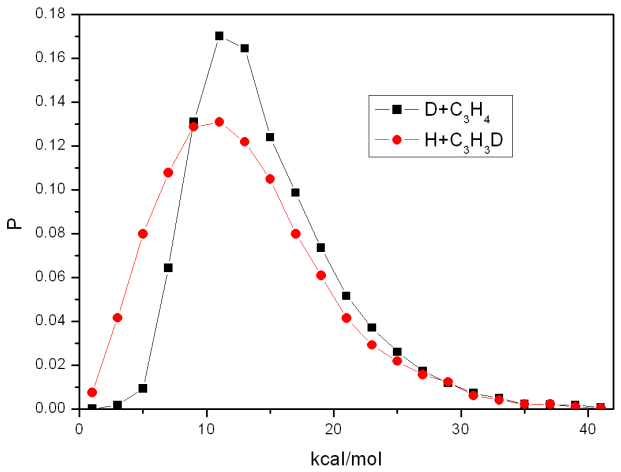

Figure 9.9 kinetic energy distribution of $D+C_3H_4$ and $H+C_3H_3D$ from dissociation of CH_2CDCH_2

feature could be explained below after looking through the form of C_3H_4/C_3H_3D in each case. For all D+C_3H_4 products, nearly all (97.6%) are in allene form; propyne and cyclopropene are rare. From Figure 9.1, we can infer that this dissociation is more or less "direct". Global minimum CH_2CDCH_2 directly overcomes TS6 barrier to lose center D to form allene+H. While in H+C_3H_3D case, the dissociation looks like to be "indirect" with more transition states and local minima involved in. Global minimum CH_2CDCH_2 should undergo some kind of isomerization to local minima to exchange center D with side end H. Therefore, in complex region, reactants can get trapped in any minimum well before dissociation, expecting no dominant products. Indeed, unlike the dominance of allene in D+C_3H_4 case, we get a fair amount of populations for each C_3H_3D isomers, nearly half (54%) in propyne form, 38.4% in allene form and 7.5% in cyclopropene form. If we look at the energy scale in Figure 9.1, the isomerization of global mininum seems to need more energy than direct overcoming TS6, so H+C_3H_3D may relatively have more chance to produce lower kinetic energy than D+C_3H_4. But the explanatoin may be wrong since hydrogen tunneling effect may play an crucial role in both channels, and we do not take it into account here. Figure 9.10 presents kinetic energy distribution for specific isomers both in D+C_3H_4 and H+C_3H_3D case. They are consistent with each other, where the distribution of C_3H_4 or C_3H_3D in propyne form peaking at lower energy (about 6 kcal/mol) than those in allene form. This result is also consistent with trajectory results in CH_2CHCH_2 case.

9.5.2 CH_3 or CH_2D Elimination Channel

In CH_2CDCH_2 case, methyl elimination channels counld be easily identified. As seen from figure 9.2, the 1,3 hydrogen shift mechanism will produce CH_3+CHCD, while the double 1,2 hydrogen shift mechanism will yield different product,CH_2D+CHCH. The kinetic energy distributions for these two channel can then be determined separately

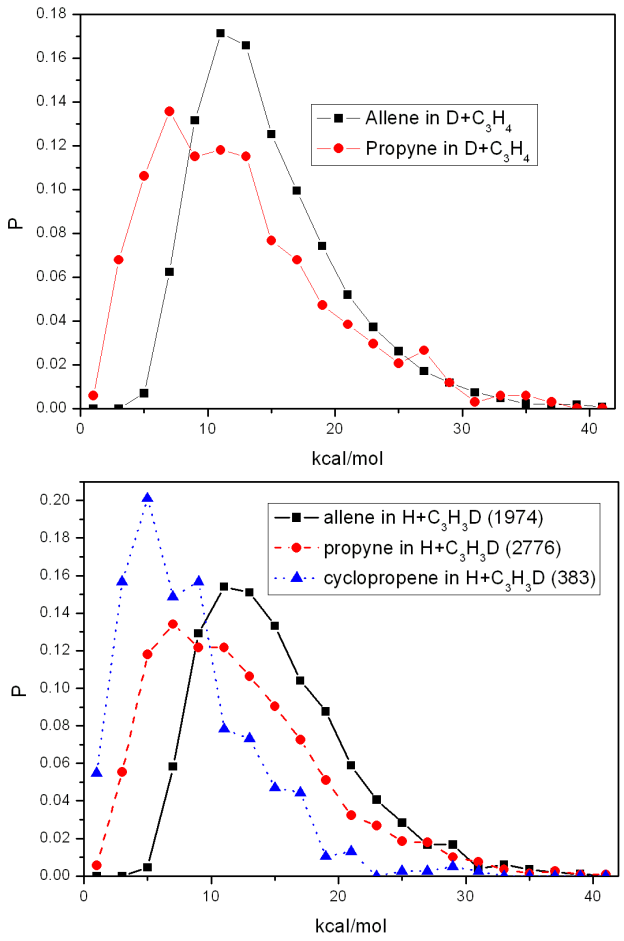

Figure 9.10 Top panel: kinetic energy distribution of D+allene and D+propyne for D+C_3H_4 channel from dissociation of CH_2CDCH_2. Bottom panel: kinetic energy distribution of H+allene, H+propyne and H+cyclopropene for H+C_3H_3D channel from dissociation of CH_2CDCH_2.

and compared to the data of Stranges et al. [87]. The figure 9.11 shows that, indeed, the distribution for the dissociation of CH_2CDCH_2 via 1,3 shift (CH_3+CHCD) peaks at a higher kinetic energy (about 14 kcal/mol) than does the distribution for dissociation via 1,2 shift (CH_2D+CHCH). The distributions from the trajectory results are in reasonable agreement with the experimental data. Similar to CH_2CHCH_2 case, the mechanism 3 pathway is beneath 1,2 shift mechanim for CH_2D+CHCH channel. Ortherwise, the RRKM theory would expect idendical kinetic energy distribution for both CH_3+CHCD and CH_2D+CHCH channels. Here the direct dissociation to vinylidine mechanism 3 channel can be expressed as

$$CH_2CDCH_2 \rightarrow CH_2D + CCH_2 \tag{9.5}$$

The same explanation as CH_2CHCH_2 case is that, the acetylene, produced from vinylidine, was created with a very large degree of vibrational energy, leaving much less energy available as kinetic energy. The kinetic energy distribution for the products of a configuration consistent with meachasnim 3 is therefore peaked at lower energy than that for products of a configuration consistent with 1,2 or 1,3 shift. And the distribution attributed to 1,2 shift from trajectoriesactually consists of a mixture of trajectories consistent with 1,2 shift and those consistent with mechanism 3. Note that for both reactions 1,2 shift and mechanism 3 starting with CH_2CDCH_2 , the deuterium winds up in the methyl fragment and the acetylene has two hydrogens. Thus, detection of the kinetic energy distributions by mass spectrometry [87] would associate the detection of C_2H_2 to both 1,2 shift and mechanism 3 while associating the detection of CHCD to 1,3 shift. Like in CH_2CHCH_2 case, we further divides the original 1,2 shift into mechanism 3 and real 1,2 shift part, and their respective kinetic energy distributions are shown in Figure 9.12. As seen, the real 1,2 shift of HCCH peaks at a position around 14 kcal/mol similar to 1,3 shift of DCCH, while the

mechanism 3 curve peaks at very low energy and goes to nearly zero at 15 kcal/mol, indicating totally different mechanisms. This comparison is also consistent with that of figure 9.6 in CH_2CHCH_2 case.

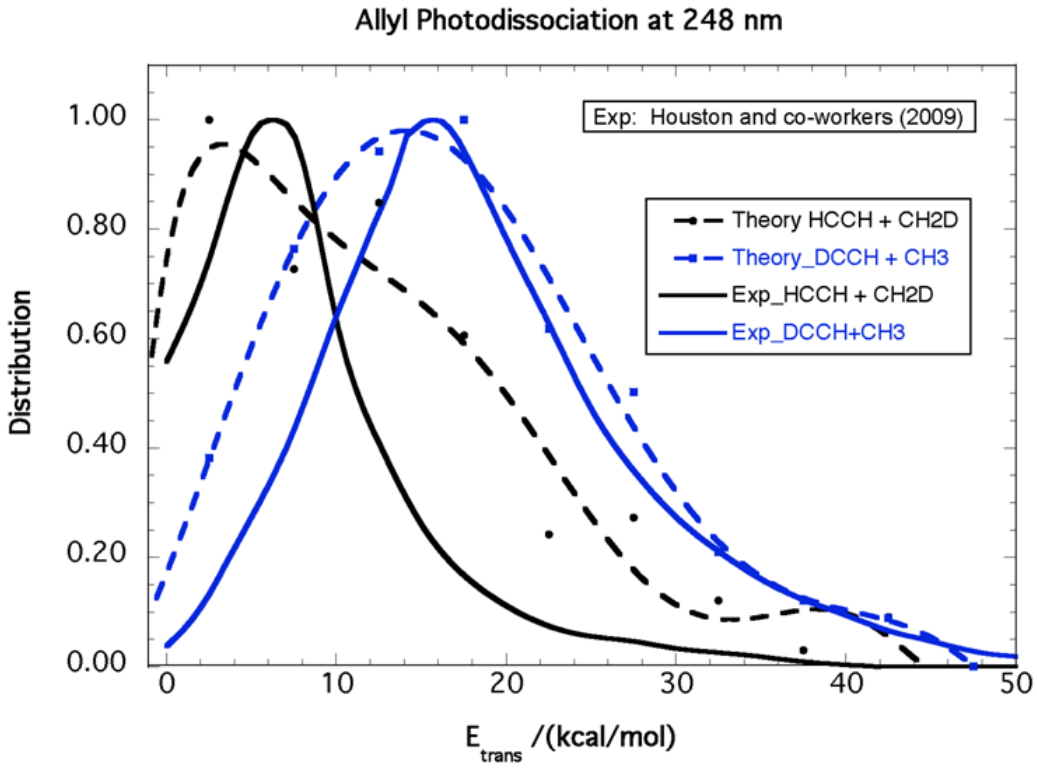

Figure 9.11 The smooth curves give the experimental kinetic energy distributions for HCCH (blue) and DCCH (red) from ref. [87]. The dashed curves give the corresponding distributions for trajectories starting at the allyl global minimum (the HCCH curve has been multiplied by 3).

The corresponding internal energy of HCCH/DCCH also provides evidences for the existence of mechanism 3. The top panel of Figure 9.13 illustrates the internal energy distribution of DCCH and HCCH for the dissociation of CH_2CDCH_2. HCCH of 1,2 shift has a little bit more population for internal energy above 60 kcal/mol than

DCCH of 1,3 shift. Further dicomposition of HCCH into real 1,2 shift and mechanism 3 is shown in the bottom panel of Figure 9.13. You can see that real 1,2 shift peaks at around 50kcal/mol, similar to the DCCH curve in top panel, while mechanism 3 distribution have a peak at around 70 kcal/mol, and does not have too much populuation below 50 kcal/mol. The real 1,2 shift curve and mechanism 3 even do not have too much overlap, indicating two distinct mechanisms.

Up to now, we confirm that mechanism 3 plays an important role in this methyl elimination channel from allyl dissociation. It is interesting to investigate why the vinylidine channel is so important even though its barrier is 26.7 kcal/mol higher than the transition state TS4. An obvious reason is that TS4 requires a very tight configuration where the hydrogen to be transferred is shared between two carbon atoms. In contrast, the methyl + vinylidine exit channel appears to be much looser. In order to compare these two channels, trajectories were calculated as a function of total energy starting at the LM1 configuration, and both the total rate of reaction from this potential energy well and the quantum yields for dissociation to methyl via

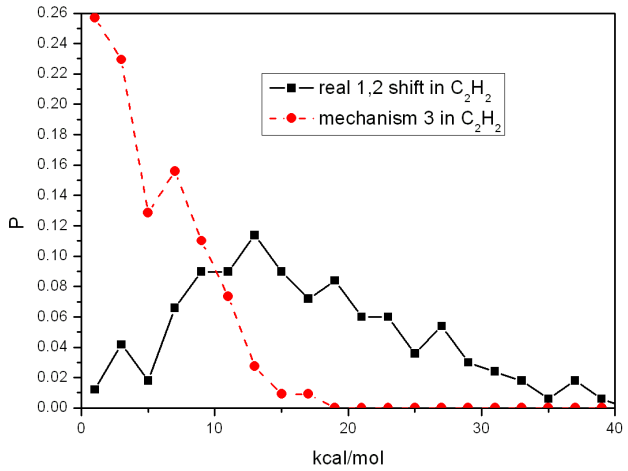

Figure 9.12 kinetic energy distribution of real 1,2 shift and mechanism 3 for $CH_2D+C_2H_2$ channel from dissociation of CH_2CDCH_2

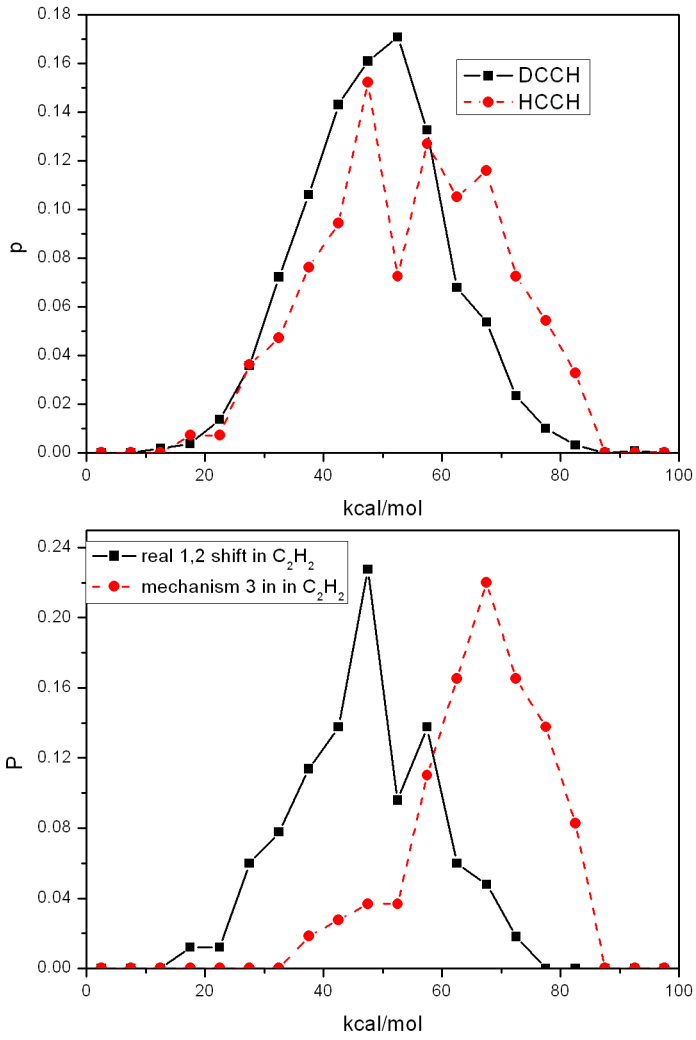

Figure 9.13 Top panel: internal energy distribution of HCCH for HCCH+CH_2D and DCCH for DCCH+CH_3 from dissociation of CH_2CDCH_2. Bottom panel: internal energy distribution of real 1,2 shift and mechanism 3 component of HCCH for HCCH+CH_2D channel from dissociation of CH_2CDCH_2.

the vinylidine channel and the channel requiring a second 1,2 hydrogen shift were tabulated. The rate for a specific channel is given by the product of the overall rate and the quantum yield for that channel. The rates of reaction as a function of energy are shown in Figure 9.14 . It is clear that, while the 1,2 shift channel dominates at very low energies, at higher energies the vinylidine channel is much more important, likely due to the smaller change in entropy between LM1 and CH_3 + CCH_2 than between LM1 and TS4.

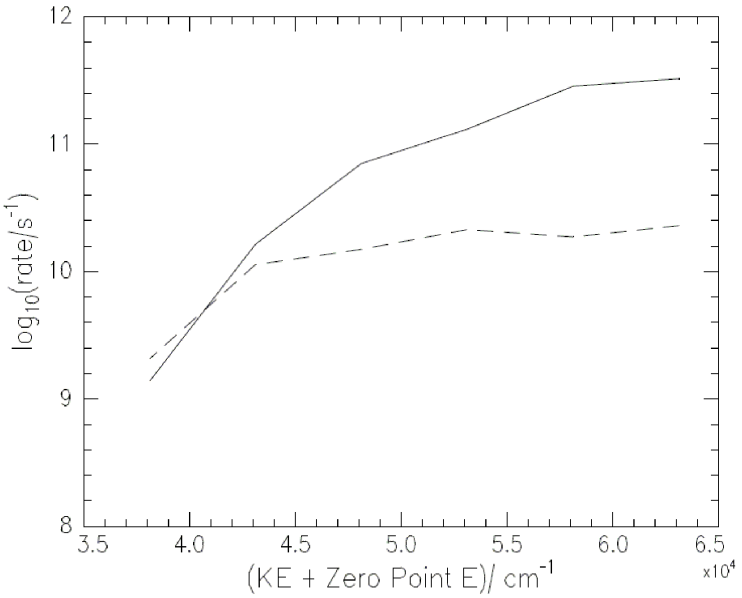

Figure 9.14 Rates of dissociation as a function of energy above the configuration of LM1 for trajectories of C_3H_5 starting at this configuration. The solid line gives the rates for production of vinylidine, whereas the dashed line gives the rate of production of methyl and acetylene via the second 1,2 hydrogen shift via TS4. While dissociation via TS4 dominates at low energy, dissociation via methyl + vinylidine becomes increasingly important at higher energy.

From a broader perspective, the allyl dissociation has similarities to a number of dissociations recently characterized by roaming mechanisms. For example, in both formaldehyde [101]- [109] and acetaldehyde [100], [110]- [115]. it has been found that, in addition to direct dissociation over the lowest energy barrier to form H_2 + CO or CH_4 + CO, a second channel opens up at somewhat higher energy in which the a

nearly dissociating fragment, H or CH_3 , respectively, returns to abstract a hydrogen from HCO. The same products are formed, but by different detailed reaction paths and with different internal energy distributions. In a similar way, the allyl radical here dissociates by two conventional channels at low energy (1,2 shift and 1,3 shift), but a third channel (mechanism 3) opens at higher energy, producing the same CH_3 + HCCH products but with a very different internal energy distribution. What the third channel for allyl dissociation has in common with the roaming channels in formaldehyde and acetaldehyde is a very loose transition state. As soon as the energy is sufficient to reach this barrier, most of the trajectories dissociate via the path over that barrier, even though it is of higher energy.

9.6 Conclusion

The dissociation of allyl radicals has been investigated by constructing a potential energy surface and performing quasiclassical trajectory calculations. Results from the calculations are in reasonable agreement with most available experimental data, although some differences remain. The most important finding is that there are actually three pathways to the methyl plus acetylene products, the two 1,2 and 1,3 hydrogen shift proposed by earlier research and a third,mechanism 3, in which dissociation from LM1 directly to vinylidine takes place. It is this third channel that is responsible for the observed difference in the kinetic energy distribution between different isotopomers of methyl and acetylene [87]. Because this channel has a loose transition state, it can dominate the dissociation at high energies. In this way, it is similar to the roaming channels observed previously for dissociation of formaldehyde and acetaldehyde. The trajectory results provide predictions for many properties that have not yet been measured experimentally, specifically angular momentum distributions, the anisotropy of dissociation, and the v-J correlation.

Bibliography

[1] H. Derksen and G. Kemper, *Computational Invariant Theory* (Springer, Berlin, 2002), Chap. 3.

[2] W. L. Hase, Classical Trajectory Simulations, in *Encyclopedia of Mass Spectrometry*, Vol 5, Chemsity and Physics of Gas-Phase Ions, ed. M. Cross and R. Capriolli, Elsevier Science, New York.

[3] J. C. Tully, R. K. Preston, J. Chem. Phys. 55, 562 (1971).

[4] M. S. Child, *Molecular Collision Theroy*, Academic Press, 1974. p. 161.

[5] G. E. Zahr, R. K. Preston, W.H. Miller, J. Chem. Phys. 62, 1127 (1974).

[6] D. C. Clary, E. Buonomo, I. R. Sims, I. W. M. Smith, W. D. Geppert, C. Naulin, M. Costes, L. Cartechini, and P. Casavecchia, J. Phys. Chem. A 106, 5541 (2002).

[7] I. W. M. Smith, Chem. Soc. Rev. 31, 137 (2003).

[8] R I. Kaiser, T. N. Le, T. L. Nguyen, A. M. Mebel, N. Balucani, Y. T. Lee, F. Stahl, P v. R. Schleyer, H. F. Schaefer III. Faraday Discuss. 119, 51 (2001).

[9] D. C. Clary, N. Haider, D. Husain, and M. Kabir, Astrophys. J. 422, 416 (1994).

[10] B. E. Turner, E. Herbst, and R. Terzieva, Astrophys. J. Suppl. Ser. 126, 427 (2000).

[11] J. Keene, K. Young, T. G. Phillips, and T. H. Bttegenbach, Astropys. J. 415, L131 (1993).

[12] R. I. Kaiser, C. Ochsenfeld, M. Head-Gordon, Y. T. Lee, and A. G. Suits, J. Chem. Phys. 106, 1729 (1997).

[13] N. Haider, and D. Husain, J. Chem. Soc., Faraday Trans. 89, 7 (1993).

[14] D. Chastaing, P. L. James, I. R. Sims, I. W. M. Smith, Phys. Chem. Chem. Phys. 1, 2247 (1999).

[15] D. Chastaing, S. D. Le Picard, I. R. Sims, I. W. M. Smith, Astron. Astrophys. 365, 241 (2001).

[16] R. I. Kaiser, D. Stranges, Y. T. Lee, A. G. Suits, Astrophys. J. 477, 982 (1997).

[17] R. I. Kaiser, A. M. Mebel, and Y. T. Lee, J. Chem. Phys. 114, 231 (2001).

[18] L. Cartechini, A. Bergeat, G. Capozza, P. Casavecchia, G. G. Volpi, W. D. Geppert, C. Naulin, and M. Costes, J. Chem. Phys. 116, 5603 (2002).

[19] M. Costes, N. Daugey, C. Naulin, A. Bergeat, F. Leonori, E. Segoloni, R. Petrucci, N. Balucani, P. Casavecchia, Faraday Discussion Chem. Soc. 133, 157 (2006).

[20] C. Ochsenfeld, R. I. Kaiser, Y. T. Lee, A. G. Suits, and M. Head-Gordon, J. Chem. Phys. 106, 4141 (1997).

[21] J. Takahashi, and K. Yashimata, J. Chem. Phys. 104, 6613 (1996).

[22] R. Guadagnini, G. C. Schatz, and S. P. Walch, J. Phys. Chem. A 102, 5857 (1998).

[23] A. M. Mebel, W. M. Jackson, A. H. H. Chang, and S. H. Lin, J. Am. Chem. Soc. 120, 5751 (1998).

[24] E. Buonomo, and D. C. Clary, J. Phys. Chem. A 105, 2694 (2001).

[25] T. Takayanagi, Chem. Phys. 312, 61 (2005).

[26] T. Takayanagi, J. Phys. Chem A 110, 361 (2006).

[27] A. M. Mebel, V. V. Kislov, M. Hayashi, J. Chem. Phys. 126 204310 (2007).

[28] N. Koga, K. Morokuma, Chem. Phys. Lett. 119, 371 (1985).

[29] F. Leonori, R. Petrucci, E Segoloni, A. Bergeat, K. M. Hickson, N. Balucani, P. Casavecchia, J. Phys. Chem. A. 112, 1363 (2008).

[30] B. J. Finlayson-Pitts, J. N. Pitts, *Chemistry of the Upper and Lower Atmosphere: Theory, Experiments, and Applications* (Academic Press, San Diego, 2000).

[31] N. M. Donahue, R. Mohrschladt, T. J. Dransfiled, J. G. Anderson, and M. K. Dubey, J. Phys. Chem. A 105, 1515 (2001).

[32] S. A. Nizkorodov and P. O. Wennberg, J. Phys. Chem. A 106, 855 (2002).

[33] H. Hippler, S. Nasterlack, and F. Striebel, Phys. Chem. Chem. Phys. 4, 2959 (2002).

[34] H. Hippler, N. Krasteva, S. Nasterlack, and F. Striebel, J. Phys. Chem. A 110, 6781 (2006).

[35] I. B. Pollack, I. M. Konen, E. X. J. Li, and M. I. Lester J. Chem. Phys. 119, 9981 (2003).

[36] I. M. Konen, I. B. Pollack, E. X. J. Li, and M. I. Lester, J. Chem. Phys. 122, 094320 (2005).

[37] I. M. Konen, E. X. J. Li, T. A. Stephenson, and M. I. Lester, J. Chem. Phys. 123, 204318 (2005).

[38] B. D. Bean, A. K. Mollner, S. A. Nizkorodov, G. Nari, M. Okumura, S. P. Sander, K. A. Peterson, and J. S. Francisco, J. Phys. Chem. A 107, 6974 (2003).

[39] J. L. Fry, S. A. Nizkorodov, M. Okumura, C. M. Roehl, J. S. Francisco, and P. O. Wennberg, J. Chem. Phys. 121, 1432 (2004).

[40] J.Matthews, A. Sinha, and J. S. Francisco, J. Chem. Phys. 120, 10543 (2004)

[41] J.Matthews and A. Sinha, J. Chem. Phys. 122, 104313 (2005).

[42] X. Zhang, M. R. Nimlos, G. B. Ellison, M. E. Varner, and J. F. Stanton, J. Chem. Phys. 124, 084305 (2006).

[43] D. A. Dixon, D. Feller, C. Zhan, and J. S. Francisco, J. Phys. Chem. A 106, 3191 (2002).

[44] K. N. Houk, K. R. Condroski, and W. A. Pryor, J. Amer. Chem. Soc. 118, 13002 (1996).

[45] D. M. Golden, J. R. Barker, and L. L. Lohr, J. Phys. Chem. A 107, 11057 (2003).

[46] R. S. Zhu and M. C. Lin, J. Chem. Phys. 119, 10667 (2003).

[47] R. Sumathi and S. D. Peyerimhoff, J. Chem. Phys. 107, 1872 (1997).

[48] Y. Li and J. S. Francisco, J. Chem. Phys. 113, 7976 (2000).

[49] K. J. Feierabend, D. K. Havey, M. E. Varner, J. F. Stanton and V. Vaida, J. Chem. Phys. 124, 124323 (2006).

[50] N. A. Burton, Y. Yamaguchi, I. L. Alberts, H. F. Schaefer. J. Chem. Phys. 95, 7466 (1991).

[51] A. B. McCoy, J. L. Fry, J. S. Francisco, A. K. Mollner, and M. Okumura, J. Chem. Phys. 122, 104311 (2005).

[52] D. P. Schofield, H. G. Kjaergaard, J. Matthews, and A. Sinha, J. Chem. Phys. 123, 134318 (2005).

[53] Y. Liu, L. L. Lohr, and J. R. Barker, J. Phys. Chem. A 110, 1267 (2006).

[54] C. F. Williams, S. K. Pogrebnya and D. C. Clary, J. Chem. Phys. 126, 154321 (2007).

[55] Y. Miller, G. M. Chaban, B. J. Finlayson-Pitts, and R. B. Gerber, J. Phys. Chem. A 110, 5342 (2006).

[56] D. M. Medvedev, S. K. Gray, E. M. Goldfield, M. Larkin, D. Troya, and G.C. Schatz, J. Chem. Phys. 120, 1231 (2004).

[57] C. M. Rosado-Reyes and J. S. Francisco, J. Phys. Chem. A 110, 4419 (2006).

[58] Z. Jin, B. J. Braams, J. M. Bowman, J. Phys. Chem. A. 110, 1569 (2006).

[59] A. B. Mccoy, B. J. Braams, A. Brown, X. Huang, Z. Jin, J. M. Bowman, J. Phys. Chem. A, 108, 499 (2004)

[60] P. J. Crutzen, *Physics and Chemistry of the Upper Atmosphere*, ed. B. McCormac, (D. Reidel, Dordrecht, Netherlands, 1973), p. 110.

[61] W. Chameides and J. C. G. Walker, J. Geophys. Res. 78, 8751 (1973).

[62] C. J. Howard and K. M. Evenson, Geophys. Res. Lett. 4, 437 (1977).

[63] C. J. Howard, J. Chem. Phys. 71, 2352 (1979).

[64] T. Imamura and N. Washida, Laser Chem. 16, 43 (1994).

[65] J. V. Seeley, R. F. Meads, M. J. Elrod and M. J.Molina, J. Phys. Chem. 100, 4026 (1996).

[66] B. Bohn and C. Zetzsch, J. Phys. Chem. A. 101, 1488 (1997).

[67] M. W. Bardwell, A. Bacak, M. T. Raventos, C. J. Percival, G. Sanchez-Reyna and D. E. Shallcross, Phys. Chem. Chem. Phys. 5, 2381 (2003).

[68] N. I. Butkovskaya, A. Kukui, N. Pouvesle and G. Le Bras, J. Phys. Chem. A. 109, 6509 (2005).

[69] N. I. Butkovskaya, A. Kukui and G. Le Bras, J. Phys. Chem. A. 111, 9047 (2007).

[70] J. Zhang and N. M. Donahue, J. Phys. Chem. A. 110, 6898 (2006).

[71] S. Aloisio and J. S. Francisco, J. Phys. Chem. A. 102, 1899 (1998).

[72] C. Gonzalez, J. Theisen, L. Zhu, H. B. Schlegel, W. L. Hase and E. W. Kaiser, J. Phys. Chem. 95, 6784 (1991).

[73] NIST Standard Reference Database Number 69, June 2005 Release, http://webbook.nist.gov/chemistry/

[74] D. J. Huchnall, Chemistry of Hydrocarbon Combustion (Chapman and Hall, London, 1985).

[75] Lara, L. M.; Rodrigo, R.; Coustenis, A.; Lopez-Moreno, J. J.; Chassefiere, E., From European Space Agency, [Special Publication], SP (1992), ESA SP-338(Proc. - Symp. Titan, 1991), 137-46.

[76] J. M. Tulloch, M. T. Macpherson, C. A. Morgan, and M. J. Pilling, J. Phys. Chem. 86, 3812 (1982).

[77] R. X. Fernandes, B. R. Giri, H. Hippler, C. Kachiani, and F. Striebel, J. Phys. Chem. A 109, 1063 (2005).

[78] T. Bentz, B. R. Giri, H. Hippler, M. Olzmann, F. Striebel, and M. Szri, J. Phys. Chem. A 111, 3812 (2007).

[79] M. E. Jenkin, T. P. Murrells, S. J. Shalliker, and G. D. Hayman, J. Chem. Soc., Faraday Trans. 89, 433 (1993).

[80] A. D. Sappey and J. C. Weisshaar, J. Phys. Chem. 91, 3731 (1987).

[81] D. W. Minsek, J. A. Blush, and P. Chen, J. Phys. Chem. 96, 2025 (1992).

[82] J. A. Blush, D. W. Minsek, and P. Chen, J. Physl Chem. 96, 10150 (1992).

[83] D. W. Minsek and P. Chen, J. Phys. Chem. 97, 13375 (1993).

[84] J.-C. Wu, R. Li, and J.-L. Chang, J. Chem. Phys. 113, 7286 (2000).

[85] C.-W. Liang, C.-C. Chen, C.-Y. Wei, and Y.-T. Chen, J. Chem. Phys. 116, 4162 (2002).

[86] D. Stranges, M. Stemmler, X. Yang, J. D. Chesko, A. G. Suits, and Y. T. Lee, J. Chem. Phys. 109, 5372 (1998).

[87] D. Stranges, P. OKeeffe, G. Scotti, R. Di Santo, and P. L. Houston, J. Chem. Phys. 128, 151101 (2008).

[88] S. G. Davis, C. K. Law, and H. Wang, J. Phys. Chem. A 103, 5889 (1999).

[89] H.-J. Deyerl, T. Gilbert, I. Fischer, and P. Chen, J. Chem. Phys. 107, 3329 (1997).

[90] H.-J. Deyerl, I. Fischer, and P. Chen, J. Chem. Phys. 110, 1450 (1999).

[91] I. Fischer and P. Chen, J. Phys. Chem. A 106, 4291 (2002).

[92] T. Schultz and I. Fischer, J. Chem. Phys. 107, 8197 (1997).

[93] T. Schultz and I. Fischer, J. Chem. Phys. 109, 5812 (1998).

[94] L. Castiglioni, A. Bach, P. Chen, Phys. Chem. Chem. Phys. 8, 2591(2006).

[95] D. E. Szpunar, M. L. Morton, and L. J. Butler, J. Phys. Chem. B 106, 8086 (2002).

[96] D. E. Szpunar, Y. Liu, M. J. McCullagh, and L. J. Butler, J. Chem. Phys. 119, 5078 (2003).

[97] H. Fan and S. T. Pratt, J. Chem. Phys. 125, 144302 (2006).

[98] H. Fan and S. T. Pratt, J. Chem. Phys. 127, 144301 (2007).

[99] N. Y. Chang, M. Y. Shen, C. H. Yu, J. Chem. Phys. 106, 3237 (1997).

[100] B. C. Shepler, B. J. Braams, and J. M.. Bowman, J. Phys. Chem. A 112, 9344 (2008).

[101] D. Townsend, S. A. Lahankar, S. K. Lee, D. Chambreau, A. G. Suits, X. Zhang, J. Rheinecker, L. B. Harding, J. M. Bowman, Science 306, 1158 (2004).

[102] X. Zhang, J. L. Rheinecker, J. M. Bowman, J. Chem. Phys. 122, 114313 (2005).

[103] J. M. Bowman, X. Zhang, Phys. Chem. Chem. Phys. 8, 321 (2006).

[104] S. A. Lahankar, S. D. Chambreau, D. Townsend, F. Suits, J. Farnum, X. Zhang, J. M. Bowman, A. G. Suits, J. Chem. Phys. 125, 044303 (2006).

[105] S. A. Lahankar, S. D. Chambreau, X. Zhang, J. M. Bowman, A. G. Suits, J. Chem. Phys. 126, 044314 (2007).

[106] A. G. Suits, S. D. Chambreau, and S. A. Lahankar, Int. Rev. Phys. Chem. 26, 585 (2007).

[107] J. Farnum, X. Zhang, J. M. Bowman, J. Chem. Phys. 126, 134305 (22006007).

[108] V. Goncharov, S. A. Lahankar, J. D. Farnum, J. M. Bowman, and A. G. Suits, J. Phys Chem. A 113, 15315 (2009).

[109] H. M. Yin, S. H. Kable, X. Zhang, J. M. Bowman, Science 311, 1443 (2006).

[110] L. B. Harding, Y. Georgievskii, and S. J. Klippenstein, J. Phys. Chem. A 114, 765 (2010).

[111] B. R. Heazlewood, M. J. T. Jordan, S. H. Kable, T. M. Selby, D. L. Osborn, B. C. Shepler, B. J. Braams, and J. M. Bowman, Proc. Nat. Acad. Sci. 105, 12719 (2008).

[112] L. Rubio-Lago, G. A. Amaral, A. Arregui, J. G. Izquierdo, F. Wang, D. Zaouris, T. N. Kitsopoulos, and L. Banares, Phys. Chem. Chem. Phys. 9, 6123 (2007).

[113] B. C. Shepler, B. J. Braams, and J. M. Bowman, J. Phys. Chem. A 111, 8282 (2007).

[114] P. L. Houston, and S. H. Kable, Proc. Nat. Acad. Sci. 103, 16079 (2006).

[115] J. M. Bowman, Proc. Nat. Acad. Sci. 103, 16061 (2006).